Dipl.-Ing. Patrick Wurm, BSc

Various efficiency improvements of concurrent and hierarchical atomistic-to-continuum multiscale methods

DOCTORAL THESIS

to achieve the university degree of

Doktor der technischen Wissenschaften (Dr. techn.)

submitted to

Graz University of Technology

Supervisor and Referee:

Assoc.Prof. Dipl.-Ing. Dr.techn. Manfred Hannes Ulz
Graz University of Technology

Referee:

Prof. Panayiotis Papadopoulos
University of California, Berkeley

Institute of Strength of Materials
Graz University of Technology

Graz, November 2020

VERSION 1.0 (November 2020)

"Various efficiency improvements of concurrent and hierarchical atomistic-to-continuum multiscale methods" by Patrick Wurm is licensed under CC BY-NC 4.0 (`https://creativecommons.org/licenses/by-nc/4.0/`).

The journal articles included in this thesis are owned by different copyright holders, thus other licenses may apply.

This document was written with texmaker, is set in Palatino, compiled with pdfLaTeX2e and `Biber`.

The LaTeX template from Karl Voit is based on KOMA script and can be found online: https://github.com/novoid/LaTeX-KOMA-template

Affidavit

I declare that I have authored this thesis independently, that I have not used other than the declared sources/resources, and that I have explicitly indicated all material which has been quoted either literally or by content from the sources used. The text document uploaded to TUGRAZonline is identical to the present dissertation.

Date	Signature

Acknowledgements

Working on this thesis was certainly the hardest challenge I ever faced in my life. As a born pessimist, I was always uncertain about the outcome, but after countless failures and setbacks, it eventually all turned out right. I am very grateful to the many people that supported and encouraged me along this exciting journey.

I want to express my deepest appreciation to my supervisor Prof. Manfred H. Ulz. You're truly one of the very few teachers I had in my life, that really stand out. You were the reason I first joined the institute as a student assistant back when I was an undergraduate, and the first to get me interested in the topic of atomistic and multiscale modeling. I was able to learn so much from you and I sincerely cannot express how thankful I am for all the support and trust you gave me in the past years.

I also wish to thank Prof. Thomas Hochrainer for many helpful discussions and for giving me a lot of freedom in my work. Many thanks to my colleague Benedikt Weger for practical suggestions on the finite element method. I will miss our coffee breaks which really loosened things up.

I would also like to extend my deepest gratitude to my girlfriend and partner, Ines. I am sure that my episodes of self-doubt and impatience were not always easy to handle. You were by my side and supported me during the most challenging times of my professional and personal life. When we met, it felt like I knew you all my life and I am so excited for our future and the many things that lay ahead.

My success would not have been possible without the support and nurturing of my family, my parents Melitta and Franz, my brother Sebastian, my grandmother Emma, my late grandmother Maria and my late grandfather Franz. Thank you for your relentless support throughout all my life.

I also want to thank Ines' parents, Silvia and Peter. You welcomed me into your family at the first day with laughter and kindness, in a way that I deeply value and I have never experienced before.

Many thanks to Prof. William Curtin for allowing me to join your group in Lausanne for a research stay und all the helpful discussions during this time. Thanks also to Prof. Panayiotis Papadopoulos, Till Junge, Max Hodapp, Guillaume Anciaux and Prof. Eric Vanden-Eijnden for your helpful comments and advice.

Vires in numeris

Abstract

Multiscale materials modeling is an effective approach for the accurate numerical study of material phenomena which occur across multiple length and time scales. Atomistic-to-continuum multiscale methods are able to drastically reduce a system's degrees of freedom in comparison to single-scale atomistic methods. However, these methods are computationally still very demanding, which presents a major hindrance to their industrial adoption. This thesis introduces three novel approaches to improve the efficiency of these methods and shows their effectiveness in various numerical examples.

The first approach is concerned with hierarchical atomistic-to-continuum multiscale methods. In these methods, the fine-scale data is often noise-corrupted due to limited computational resources. This noise impairs the convergence behavior of the multiscale method and creates a setting that shows remarkable resemblance to iteration schemes known from the field of stochastic approximation. This resemblance justifies the use of two well-known stochastic approximation averaging strategies in the multiscale method. It is found that the averaging strategies reduce the impact of the noise and improve the convergence behavior of the multiscale method.

The second and third approaches are concerned with concurrent atomistic-to-continuum methods. The scales are commonly coupled at fixed intervals of time in these methods, which is often inefficient. In the second approach, a demand-based coupling is proposed instead, in order to save redundant coarse-scale computations. This coupling is achieved via a novel algorithm which continuously judges, based on the local deformation at the coupling interface, whether the coarse-scale computations are necessary or not.

The continuum models in concurrent atomistic-to-continuum methods are either dynamic or quasi-static, both of which are shown to have advantages but also significant drawbacks. In the third approach, an alternative model, suitable for linear elastic continua, is presented. This hybrid model uses a complementary superposition of a dynamic and a quasi-static subproblem and aims at combining the advantages of the dynamic and quasi-static models, while avoiding the drawbacks.

Kurzfassung

Die Mehrskalenmodellierung von Materialien ist ein effektiver Ansatz für die präzise numerische Untersuchung von Materialphänomenen, in die mehrere Längen- und Zeitskalen involviert sind. Obwohl es Atomistik-zu-Kontinuum Mehrskalenmethoden verglichen mit atomistischen Methoden erlauben, die Freiheitsgrade eines Systems drastisch zu reduzieren, sind sie dennoch mit enormem Rechenaufwand verbunden. Dies stellt ein großes Hindernis für den industriellen Einsatz dieser Methoden dar. Diese Dissertation stellt drei neue Verfahren zur Effizienzsteigerung der Atomistik-zu-Kontinuum Mehrskalenmethoden vor und zeigt deren Effektivität anhand von zahlreichen numerischen Beispielen.

Das erste Verfahren beschäftigt sich mit hierarchischen Atomistik-zu-Kontinuum Mehrskalenmethoden. In diesen Methoden sind die ermittelten Größen auf der feinen Skala durch unzureichende Rechenleistung oft fehlerbehaftet. Diese Fehler beinträchtigen das Konvergenzverhalten der Mehrskalenmethode und erzeugen eine Situation, die große Ähnlichkeit mit Iterationsverfahren aus dem Gebiet der stochastischen Approximation aufweist. Diese Ähnlichkeit rechtfertigt die Anwendung zweier, aus der stochastischen Approximation bekannter, Mittelungsverfahren im Mehrskalenmodell. Es wird gezeigt, dass die Mittelungsverfahren den negativen Einfluss der fehlerbehafteten Größen reduzieren und so das Konvergenzverhalten der Mehrskalenmethode verbessern können.

Das zweite und dritte Verfahren beschäftigt sich mit Atomistik-zu-Kontinuum Mehrskalenmethoden auf geteilten Gebieten. In diesen Methoden werden die Skalen üblicherweise in festen zeitlichen Intervallen miteinander gekoppelt; ein Ansatz, der oft ineffizient ist. Um überflüssige Rechenzeit auf der groben Skala zu vermeiden wird stattdessen eine bedarfsabhängige Kopplung vorgeschlagen. Diese Kopplung wird durch einen neuartigen Algorithmus erreicht, der ständig, basierend auf der lokalen Deformation an der Grenzfläche der beiden Skalen, entscheidet ob Berechnungen auf der groben Skala gerade notwendig sind oder nicht.

Die Kontinuumsmodelle in Atomistik-zu-Kontinuum Mehrskalenmethoden auf geteilten Gebieten sind entweder dynamisch oder quasi-statisch. Es wird gezeigt, dass beide Ansätze Vorteile, aber auch erhebliche Nachteile aufweisen. Als drittes Verfahren wird deshalb ein alternatives Kontinuumsmodell vorgeschlagen, das für linear-elastische

Kontinua geeignet ist. Das Verfahren beruht auf der komplementären Superposition eines dynamischen und eines quasi-statischen Subproblems. Das dadurch entstehende hybride Kontinuumsmodell zielt darauf ab, die Vorteile eines dynamischen und eines quasi-statischen Kontinuumsmodells zu vereinen und die Nachteile zu vermeiden.

Contents

List of Symbols

This thesis combines topics from various broad fields such as continuum and statistical mechanics, the finite element method, molecular dynamics, stochastic approximation and others, each having their own common notation. In the thesis, the common notation of every field is used wherever possible, which unavoidably leads to the multiple use of symbols in some cases. However, in these cases, the same symbols denote very different quantities which do not appear in the same parts of the text. It is therefore hoped that the correct meaning of the symbol is immediately clear from context and does not cause any confusion. In the notation convention used, spatial dimensions are denoted by italic subscripts with roman letters, using uppercase letters for the referential configuration (*e.g.*, $\bullet_I$) and lowercase letters for the current configuration (*e.g.*, $\bullet_i$). Descriptive notation is denoted as nonitalic superscripts with roman letters (*e.g.*, $\bullet^{\max}$), discrete time indices as italic superscripts with roman letters (*e.g.*, $\bullet^n$), iterations as italic superscripts with roman letters in parentheses (*e.g.*, $\bullet^{(n)}$), descriptive indices such as particle/atom numbers as italic superscript with greek letters (*e.g.*, $\bullet^\alpha$) and node numbers as italic superscript with capital roman letters (*e.g.*, $\bullet^I$).

Greek symbols

α	pulse parameter
$\boldsymbol{\alpha}$	known target vector used in the root finding of the function $\boldsymbol{\alpha} - \mathbf{g}(\boldsymbol{\theta}) = \mathbf{0}$
β	thermodynamic beta, *i.e.*, $\beta = 1/(k^{\mathrm{B}}T)$
Γ	phase space
γ	Langevin damping coefficient
ε	Lennard-Jones energy parameter
ε	engineering strain
ε	stochastic approximation gain sequence
η	entropy per volume
$\boldsymbol{\Theta}$	sample average of the series of estimated parameters $\boldsymbol{\theta}$ in the stochastic approximation process
$\boldsymbol{\theta}$	vector of parameters being estimated in the stochastic approximation process
$\boldsymbol{\theta}^*$	root of the function $\boldsymbol{\alpha} - \mathbf{g}(\boldsymbol{\theta}) = \mathbf{0}$
κ	constant used in the definition of the stochastic approximation gain sequence

Λ	radial pulse parameter
λ	constant used in the definition of the stochastic approximation gain sequence
$\boldsymbol{\xi}^p$	vector with value one at its p-th component and zero in all others
$\boldsymbol{\Pi}, \Pi_{ij}$	generalized momentum of the molecular dynamics cell
ρ	mass density in the current configuration
ρ^0	mass density in the reference configuration
ρ^{EAM}	electron charge density function of the EAM potential
σ	Lennard-Jones distance parameter
$\boldsymbol{\sigma}, \sigma_{ij}$	Cauchy stress tensor
χ	deformation mapping
Ψ	Helmholtz free energy
Ω	volume of the atomistic region
Ω^0	volume of the referential molecular dynamics cell
Ω^σ	volume of the atomistic region used for stress evaluation
ω	angular frequency

Roman symbols

A	amplitude
$A(\mathbf{r}, \mathbf{p})$	microscopic phase space function
$\mathcal{A}$	macroscopic observable
$\mathbf{A^1}, \mathbf{A^2}, \mathbf{A^3}$	edge vectors of the undeformed molecular dynamics cell
$\mathbf{a}, a_i$	continuum acceleration field
a	equilibrium atomic spacing
$\mathbf{a^1}, \mathbf{a^2}, \mathbf{a^3}$	edge vectors of the deformed molecular dynamics cell
B	continuum body
$\mathbf{B}, B_{ij}$	left Cauchy-Green deformation tensor
b	magnitude of the Burgers vector
$\mathbf{b}, b_i$	body force per unit mass
$\mathbf{C}, C_{IJ}$	right Cauchy-Green deformation tensor
$\mathbb{C}, C_{IJKL}$	Lagrangian elasticity tensor
$\mathbb{C}^{\mathrm{inst}}, C^{\mathrm{inst}}_{IJKL}$	instantaneous microscopic elasticity tensor
$\mathbb{C}^{\mathrm{inst,kin}}, C^{\mathrm{inst,kin}}_{IJKL}$	kinetic part of the instantaneous microscopic elasticity tensor
$\mathbb{C}^{\mathrm{inst,pot}}, C^{\mathrm{inst,pot}}_{IJKL}$	potential part of the instantaneous microscopic elasticity tensor
c	stochastic approximation gain sequence
D	integer factor used in the signal downsampling operation

$\mathbf{D}$	damping matrix
d	distance between the spatial coupling interface and a band of atoms
E	total energy
$\mathbf{E}, E_{IJ}$	Green-Lagrange strain tensor
$\mathbf{e}$	vector-valued noise term
$\mathbf{e^1}, \mathbf{e^2}, \mathbf{e^3}$	unit vectors
$\mathbf{e}, e_{ij}$	Euler-Almansi strain tensor
F	embedding energy function of the EAM potential
$\mathbf{F}, F_{iJ}$	deformation gradient tensor
$\delta\mathbf{F}, \delta F_{iJ}$	first variation of the deformation gradient tensor
$f(\mathbf{r}, \mathbf{p})$	phase space distribution function
$f^{A,\min}$	smallest frequency of the atomic motion
f^{c}	cut-off frequency
$f^{\mathrm{c}*}$	normalized cut-off frequency
f^{FE}	maximum admissible continuum frequency
$f^{\max}$	maximum frequency of the atomic vibration
f^{Ny}	Nyquist sampling rate
f^{s}	rate of the filter input signal
$\mathbf{f}^{\alpha}, f_i^{\alpha}$	force on atom α
$\mathbf{f}^{\mathrm{r}}, f_i^{r}$	random force
$\mathbf{f}^{\mathrm{ext}}$	column matrix of external nodal forces
$\mathbf{f}^{\mathrm{int}}$	column matrix of internal nodal forces
g	number of independent momentum degrees of freedom in a discrete system
$\mathbf{g}$	vector-valued function for which the root of $\boldsymbol{\alpha} - \mathbf{g}(\boldsymbol{\theta}) = \mathbf{0}$ with known $\boldsymbol{\alpha}$ is to be found via stochastic approximation
$\widehat{\mathbf{g}}$	finite difference estimate of a function $\mathbf{g}(\boldsymbol{\theta}) = \partial L/\partial\boldsymbol{\theta} = \mathbf{0}$.
$\mathcal{H}$	Hamiltonian
$\mathcal{H}^{\mathrm{N}}$	Nosé Hamiltonian
$\mathcal{H}^{\mathrm{R}}$	Ray-Rahman Hamiltonian
$h^{\max}$	length of the largest finite element (1D)
$\mathbf{h}, h_i$	Cauchy entropy flux per area
$\mathbf{I}$	unit tensor
J	determinant of the deformation gradient tensor
$\mathbf{J}, J_{IJ}$	referential inertia tensor
K^{f}	filter kernel normalization constant

$\mathcal{K}^{\text{atoms}}$	kinetic energy of the atoms
$\mathcal{K}^{\text{cell}}$	kinetic energy of the molecular dynamics cell
$\mathcal{K}^{\text{heatbath}}$	kinetic energy of the heatbath
$\mathbf{K}$	stiffness matrix
k	spring stiffness
k	wave number
k^{B}	Boltzmann constant
$\mathbf{k}, k^j$	filter kernel
L	loss function
$\mathcal{L}$	Lagrangian
M	length of the filter kernel
MAE	mean absolute error
$\mathcal{M}$	number of fine-scale time steps
$\mathbf{M}$	mass matrix
m	mass
N	number of discrete particles
N^{b}	number of band atoms
N^{d}	number of spatial dimensions
N^{nodes}	number of finite element nodes
N^{off}	size of the averaging window in the stochastic approximation iterate (offline) averaging
N^{on}	size of the averaging window in the stochastic approximation iterate and observation (online) averaging
N^{q}	number of Gauss points
$\mathbf{N}, N_I$	outwards unit normal vector (in the reference configuration)
$\mathbf{n}, n_i$	outwards unit normal vector (in the current configuration)
P	continuum particle
$\mathbf{P}, P_{iJ}$	first Piola-Kirchhoff stress tensor
p^s	conjugate momentum of the degree of freedom of the thermal reservoir
$\mathbf{p}, p_i$	momenta of discrete particles
Q	thermal "mass" of the thermal reservoir
$\mathbf{q}, q_i$	heat flux per unit surface area
r	heat source per unit time and volume
R	reflection coefficient
RMSD	root-mean-square deviation

r^{cut}	cut-off radius
$r^{\alpha\beta}$	distance between two discrete particles α and β
$\tilde{r}$	entropy source per time and per volume
$\mathbf{r}, r_i$	positions of discrete particles
$\dot{\mathbf{r}}, \dot{r}_i$	velocities of discrete particles
$\mathbf{r}$	residual
S	finite element shape functions
$\mathbf{S}, S_{IJ}$	second Piola-Kirchhoff stress tensor
$\mathbf{S}^{\text{ext}}, S_{IJ}^{\text{ext}}$	externally applied second Piola-Kirchhoff stress tensor
$\mathbf{S}^{\text{inst}}, S_{IJ}^{\text{inst}}$	instantaneous microscopic stress tensor
s	degree of freedom of the thermal reservoir
$\mathbf{s}, s_i$	positions of discrete particles in the undeformed molecular dynamics cell
$\mathbf{s}^0, s_i^0$	initial positions of discrete particles in the undeformed molecular dynamics cell
T	temperature
T^∞	temperature of the heatbath
$\mathbf{T}, T_i$	first Piola-Kirchhoff traction vector
$\hat{\mathbf{T}}, \hat{T}_i$	prescribed first Piola-Kirchhoff traction vector
t, τ	time
Δt	coarse scale time step
Δt^{c}	minimum period of time for which the continuum is activated
Δt^{delay}	time delay in the filter output
$\Delta\tau$	fine-scale time step
$\mathbf{t}, t_i$	Cauchy traction vector
$\hat{\mathbf{t}}, \hat{t}_i$	prescribed Cauchy traction vector
$\mathbf{U}$	estimate of the Jacobian matrix of the vector-valued function $\mathbf{g}$
$\mathcal{U}$	potential energy
$\mathcal{U}^3$	potential energy due to three-body interactions of discrete particles
$\mathcal{U}^{\text{atoms}}$	potential energy of the atoms
$\mathcal{U}^{\text{cell}}$	potential energy of the molecular dynamics cell
$\mathcal{U}^{\text{ext}}$	potential energy due to an externally applied potential field
$\mathcal{U}^{\text{heatbath}}$	potential energy of the heatbath
$\mathcal{U}^{\text{pair}}$	potential energy due to pair interactions of discrete particles
$\mathcal{U}^\alpha$	potential energy of atom α
u	internal energy per unit volume

$\mathbf{u}, u_i$	continuum displacement field
$\mathbf{u}^{A,\alpha}, u_i^{A,\alpha}$	displacement of atom α
$\dot{\mathbf{u}}^{A,\alpha}, \dot{u}_i^{A,\alpha}$	velocity of atom α
$\ddot{\mathbf{u}}^{A,\alpha}, \ddot{u}_i^{A,\alpha}$	acceleration of atom α
$\mathbf{u}$	column matrix of nodal displacements
$\dot{\mathbf{u}}$	column matrix of nodal velocities
$\ddot{\mathbf{u}}$	column matrix of nodal accelerations
$\Delta\mathbf{u}$	column matrix of nodal displacement increments
V	volume occupied by the continuum body in the current configuration
V^0	volume occupied by the continuum body in the reference configuration
$V^{0,e}$	volume occupied by a finite element in the reference configuration
∂V^{u}	displacement boundary in the current configuration
∂V^{σ}	traction boundary in the current configuration
$\partial V^{0,\sigma}$	traction boundary in the reference configuration
$\mathbf{v}, v_i$	continuum velocity field
W	strain-energy function
w^{q}	Gauss quadrature weights
$\mathbf{X}, X_I$	position vector of a continuum particle (reference configuration)
x^{q}	coordinates of the Gauss points
$\mathbf{x}, x^n$	filter input
$\mathbf{x}, x_i$	position vector of a continuum particle (current configuration)
$\delta\mathbf{u}, \delta u_i$	first variation of the displacement field
$\mathbf{Y}$	noisy measurement of the vector-valued function $\boldsymbol{\theta}$
y	noisy measurement of the loss function L
$\mathbf{y}, y^n$	filter output
$\mathbf{y}^{\max}$	maximum filter output in equilibrium
$\mathbf{y}^{\min}$	minimum filter output in equilibrium
$\Delta\mathbf{y}$	fluctuations in the filter output signal

Mathematical notation

$\langle\bullet\rangle$	ensemble average
$\lceil\bullet\rceil$	ceil function
$\overline{\bullet}$	time average, set closure
$\widehat{\bullet}$	prescribed quantity at a boundary
$\mathcal{O}(n)$	terms proportional to order n

1. Introduction

1.1. Motivation

The exponential technical progress in the last two centuries is closely linked to the development of new materials and applications. Until the dawn of computers, material development heavily relied on experiments and application development was largely based on prototyping, experience, and trial and error. Computers allowed to create and manipulate virtual matter, to perform virtual experiments and develop virtual prototypes. Modern simulation methods allow to replace costly experiments and tests by virtual clones. These methods allow engineers to study phenomena which are difficult or impossible to study in experiments.

There are many well established theories which describe the mechanical behavior of virtual matter at certain length and time scales (see Fig. 1.1).

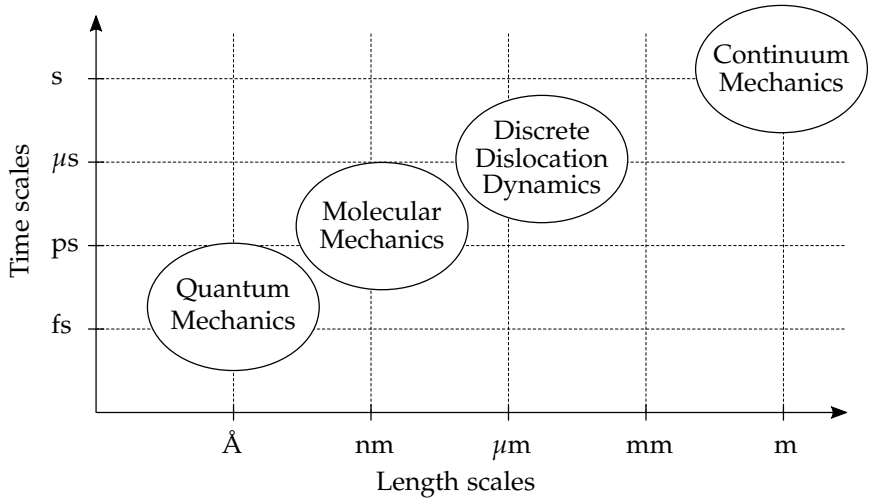

Fig. 1.1.: Length and time scales in the mechanical modeling of materials.

The fine end of the scales is the so-called microscale, where the theories of quantum and molecular mechanics exist. Quantum mechanics and its numerical realizations (*e.g.*, density functional theory and the tight-binding method) aim at solving Schrödinger's

wave equation in order to obtain a highly accurate representation of the electronic structure and the interactions in atomic systems. When the Born-Oppenheimer approximation and the assumption of classical particles hold, the classical molecular mechanics theory is valid. In this theory, the potential energy of a system of atoms may be represented by an effective potential which is a function of the nuclear coordinates only (see, *e.g.*, Tadmor and Miller, 2011). This effective potential, called the interatomic potential, therefore contains no explicit contribution of the electrons. A numerical realization of molecular mechanics is the molecular dynamics simulation technique (MD), which is briefly presented in Section 2.2.4. The coarse end of the scales is the so-called macroscale, where the continuum theory exists. This theory omits the discrete structure of the material and assumes a medium (the continuum) with a continuous distribution of matter in space. A numerical realization of continuum theory is the finite element method (FEM), briefly presented in Section 2.1.4. Between the micro- and macroscale, various so-called mesoscale theories exist. An example of a numerical realization of a meso-scale theory is, *e.g.*, discrete dislocation dynamics.

In the development of new materials with characteristic features in the nanometer range (*e.g.*, nano-structured materials) and new applications (*e.g.*, micro- and nano-electro-mechanical devices), it became clear that simulation techniques operating on a single scale (micro-/meso-/macroscale) are insufficient. In micro- and nano-electro-mechanical devices, the accurate modeling of the features requires simulation techniques with microscopic resolution, *e.g.*, MD, however, the overall size of the devices is too large to be treated solely by MD, due to computational limitations and requires *e.g.*, the FEM (Rudd, 2001; Karakasidis and Charitidis, 2007). Similarly, in nano-structured materials, the features require atomic resolution, but again, the representative volume elements are too large to be handled by MD and thus require methods from larger scales (Chen *et al.*, 2014; Aluko, Gowtham, and Odegard, 2017).

The so-called atomistic-to-continuum multiscale methods have been developed to bridge this gap between the scales. These methods can be divided into two categories.[1] On one hand, there are concurrent methods, in which the body of interest is spatially decomposed into atomistic and continuum regions, thus introducing a direct spatial coupling between the two scales. On the other hand, there are hierarchical methods, in which there is no spatial coupling. Instead, both scales exist everywhere in the body and the atomistic scale is used to compute missing data for the continuum scale. In comparison to single-scale atomistic methods, the atomistic-to-continuum multiscale methods allow to study much larger spatial systems over longer periods

[1] Unfortunately, there exist different terminology conventions for the subcategories of atomistic-to-continuum multiscale methods, which may lead to confusion. For example, some authors use the term concurrent method as an overarching category over the two presented categories, which is then divided into partitioned-domain and hierarchical, while other authors use the term semiconcurrent instead of hierarchical.

of time at the same computational cost. From a different point of view, they aim at producing the same results as if the problem was modeled purely atomistic, but at a fraction of the computational cost. Despite the major decrease in computational cost, the computational demands of the multiscale methods are still relatively high and thus, they heavily rely on the use of high performance computing. Due to the computational demands these methods are still only of academic interest and have not yet received industrial adoption. To start this process, novel approaches to increase their efficiency are needed (Van der Giessen *et al.*, 2020).

1.2. Objectives and challenges

The main objective of this thesis is to develop approaches to increase the efficiency of atomistic-to-continuum multiscale methods. The increase in efficiency can be understood in three ways. Such approaches may allow one to i) achieve results of the same quality at reduced computational cost, or ii) achieve results of higher quality at the same computational cost, or iii) study larger systems over longer periods of time at the same computational cost and accuracy.

Such approaches will be presented for hierarchical (see Chapter 4) as well as for concurrent methods (see Chaps. 5 and 6). In the development, the focus is laid on keeping the approaches as general as possible, so that they can be applied to a variety of methods. To test and validate the approaches, existing multiscale methods are naturally needed as test vehicles. While many openly accessible tools exist for single-scale methods (*e.g.*, Quantum Espresso (Giannozzi *et al.*, 2009), LAMMPS (Plimpton, 1995), ParaDis (Cai *et al.*, 2004), OOF2 (Reid *et al.*, 2009), deal.II (Arndt *et al.*, 2019)), the vast majority of all multiscale methods are still limited to not openly-accessible, in-house research codes. In the development of approaches to increase the efficiency of the multiscale methods, one faces a high barrier to entry as the test vehicle, a numerical implementation of the multiscale method of interest, needs to be established first. Thus, a significant amount of programming work was spent to establish one of the two methods used in this thesis more or less from scratch, based on the available description of the method in the literature.[2]

[2]The code is openly accessible at `https://github.com/patrickwurm/CADD`.

1.3. Author contributions

In this section, the three efficiency improvement approaches presented in this thesis, their contribution to the objective of this thesis and the author's individual contribution to each of the three approaches, are briefly summarized.

"A stochastic approximation approach to improve the convergence behavior of hierarchical atomistic-to-continuum multiscale methods" (Chapter 4)
A general approach to increase the efficiency of hierarchical atomistic-to-continuum multiscale methods is proposed. In the approach, well-known averaging techniques methods from the field of stochastic approximation are applied on the macroscopic observables obtained from the fine-scale computations.

Individual contribution:

- Contribution to the original idea
- Literature research and selection of the stochastic approximation (SA) averaging strategies
- Implementation of the SA averaging strategies into an existing code of a hierarchical multiscale method
- Design, implementation and evaluation of three numerical examples
- Writing of the publication (80%)

"Demand-based coupling of the scales in concurrent atomistic-to-continuum methods at finite temperature" (Chapter 5)
To increase the efficiency in various concurrent atomistic-to-continuum methods, an algorithm which detects deformation at the spatial coupling interface, and avoids redundant continuum computations, is developed.

Individual contributions:

- Contribution to the original idea
- Programming of a one- and two-dimensional code of the Coupled Atomistic and Discrete Discloation (CADD) method from scratch with various features such as
  - Multiple interatomic potentials (Lennard-Jones potential, Embedded atom method)
  - Suitable for studying NVE and NVT (Langevin thermostat, Nose-Hoover thermostat) ensembles in the atomistic region
  - Ability to detect dislocations and pass those from the atomistic to the continuum region (in the two-dimensional version)
- Literature research and development of the deformation detection algorithm

- Application of the proposed approach to the CADD code
- Design, implementation and evaluation of three numerical examples
- Writing of the publication (90%)

"A hybrid continuum model for dynamic concurrent atomistic-to-continuum methods" (Chapter 6)
To increase efficiency, a hybrid (quasi-static and dynamic) continuum model, applicable to various concurrent atomistic-to-continuum methods, is proposed.

Individual contributions:

- Contribution to the original idea
- Literature research
- Implementation of the quasi-static and hybrid continuum models into the previously developed CADD code
- Design, implementation and evaluation of three numerical examples
- Writing of a manuscript (90%), which is in preparation of submission as of the writing of this thesis

1.4. Organization

This thesis is organized as follows: in Chapter 2, the fundamentals of continuum mechanics and statistical mechanics are presented in a brief extent which covers the basics needed to provide a foundation for the following chapters. The presentation is not extensive by any means and references to supplementing literature are provided in the text. Chapter 3 gives an overview of the state of the art in atomistic-to-continuum multiscale modeling. The three efficiency improvement approaches which present the novel contribution to the field of atomistic-to-continuum multiscale modeling are given in Chaps. 4-6. The thesis closes with a conclusion in Chapter 7.

2. Fundamentals of continuum mechanics and statistical mechanics

2.1. Continuum mechanics

This section gives a brief introduction into the mechanics of continuous media and the finite element method. For further information, see, *e.g.*, Malvern (1969); Truesdell and Noll (1992); Marsden and Hughes (1994); Bonet and Wood (1997); Holzapfel (2000); Belytschko, Liu, and Moran (2000); Zienkiewicz and Taylor (2000); Tadmor, Miller, and Elliott (2011).

Continuum mechanics is concerned with the study of the mechanical behavior of materials modeled as a continuum. In a continuum, the discrete atomic structure of the material is omitted, and instead, the material is viewed as a continuous medium, possessing a continuous distribution of matter in space. By doing so, the large number of atoms is replaced by a few meaningful quantities. This kind of approach is known as macroscopic modeling. A continuum body B in a three-dimensional Euclidean space is the collection of continuum particles $P \in B$. At every instant of time t, the continuum body occupies a volume V. Each continuum particle P is located at a point x in space, the position of which is described by the position vector $\mathbf{x}$ with respect to a Cartesian reference coordinate system. The configuration of B at time t is known as the current (or deformed) configuration. Additionally, a reference (or undeformed) configuration is defined, in which the continuum body occupies a volume V^0 and the location of each continuum particle is described by a position vector $\mathbf{X}$ (see Fig. 2.2).

The motion of particles from their reference position $\mathbf{X}$ to their current position $\mathbf{x}$ is described by a uniquely invertible and sufficiently differentiable mapping χ, such that $\mathbf{x} = \chi(\mathbf{X}, t)$. The displacement field (in Lagrangian description) is defined as $\mathbf{u}(\mathbf{X}, t) = \chi(\mathbf{X}, t) - \mathbf{X}$. The velocity and acceleration of a material point can thus be defined as

$$\mathbf{v}(\mathbf{X}, t) = \frac{\partial \chi(\mathbf{X}, t)}{\partial t} = \frac{\partial \mathbf{u}(\mathbf{X}, t)}{\partial t} = \dot{\mathbf{u}} \tag{2.1}$$

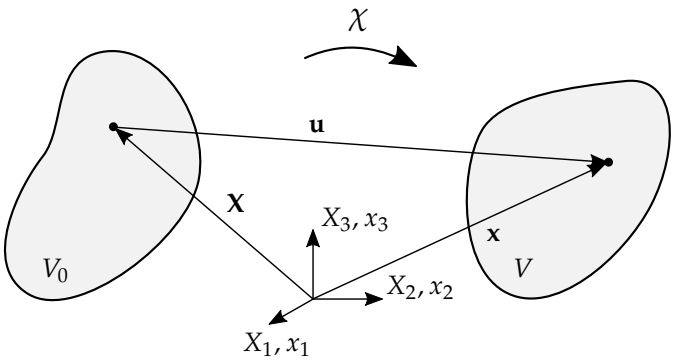

Fig. 2.1.: Undeformed and deformed configurations.

and

$$\mathbf{a}(\mathbf{X}, t) = \frac{\partial^2 \boldsymbol{\chi}(\mathbf{X}, t)}{\partial t^2} = \frac{\partial^2 \mathbf{u}(\mathbf{X}, t)}{\partial t^2} = \ddot{\mathbf{u}}, \tag{2.2}$$

respectively.

2.1.1. Strain

The fundamental quantity in the description of the local deformation at a material point is the deformation gradient tensor

$$\mathbf{F} = \frac{\partial \boldsymbol{\chi}(\mathbf{X}, t)}{\partial \mathbf{X}}, \tag{2.3}$$

which transforms elemental vectors $d\mathbf{X}$ in the reference configuration into elemental vectors $d\mathbf{x}$ in the current configuration via $d\mathbf{x} = \mathbf{F}d\mathbf{X}$.

With aid of the deformation gradient tensor, suitable strain measures can be defined, such as the Green-Lagrange strain tensor

$$\mathbf{E} = \frac{1}{2}(\mathbf{C} - \mathbf{I}), \tag{2.4}$$

which operates on vectors in the reference configuration, where $\mathbf{C} = \mathbf{F}^T\mathbf{F}$ is the right Cauchy-Green deformation tensor and $\mathbf{I}$ is the unit tensor, or the Euler-Almansi strain tensor

$$\mathbf{e} = \frac{1}{2}(\mathbf{I} - \mathbf{B}^{-1}), \tag{2.5}$$

which operates on vectors in the current configuration, where $\mathbf{B}^{-1}$ is the inverse of the left Cauchy-Green deformation tensor $\mathbf{B} = \mathbf{F}\mathbf{F}^T$.

2.1.2. Stress

To describe the interaction between the continuum particles, the fundamental concept of stress is introduced. A cut through the body in the current configuration along an arbitrary plane (with outwards unit normal vector **n**) reveals in every material point **x** the Cauchy traction vector **t**, which measures the force per unit surface in the current configuration. The corresponding cut along the plane in the reference configuration (with outwards unit normal vector **N**) reveals the first Piola-Kirchhoff traction vector **T**.

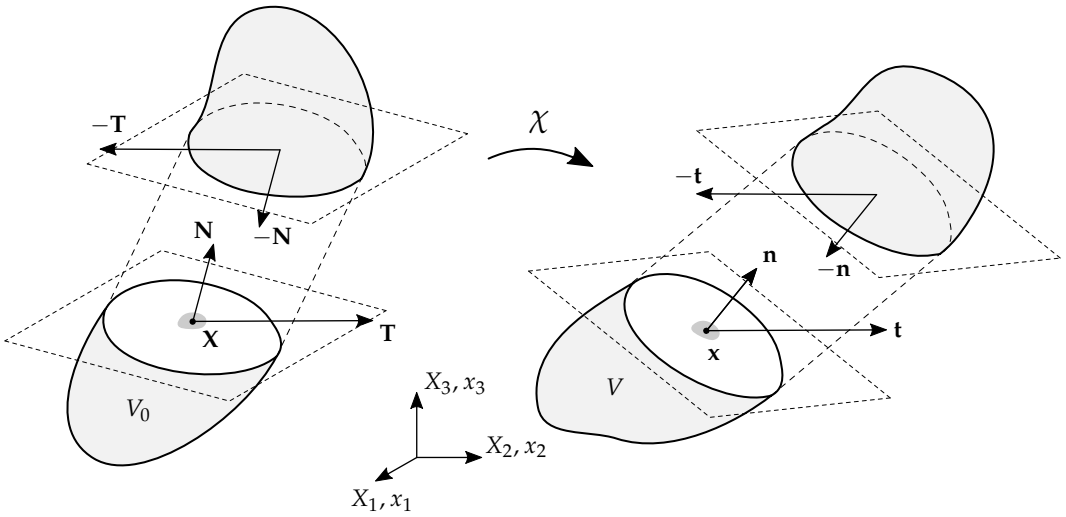

Fig. 2.2.: Traction vectors **T** and **t** in the undeformed and deformed configuration.

Cauchy's stress theorem states that there exist second order tensors σ and **P**, such that (Holzapfel, 2000)

$$\mathbf{t}(\mathbf{x}, t, \mathbf{n}) = \sigma(\mathbf{x}, t)\mathbf{n}, \tag{2.6}$$

$$\mathbf{T}(\mathbf{X}, t, \mathbf{N}) = \mathbf{P}(\mathbf{X}, t)\mathbf{N}, \tag{2.7}$$

where σ is the Cauchy stress tensor and **P** is the first Piola-Kirchhoff stress tensor. There exist various other stress tensors such as the Kirchhoff, Biot and second Piola-Kirchhoff stress tensors. An overview is, *e.g.*, given in Bonet and Wood (1997). As an example, the second Piola-Kirchhoff stress tensor shall be given here, which is related to the Cauchy and the first Piola-Kirchhoff stress tensors via the relations

$$\mathbf{S} = J\mathbf{F}^{-1}\sigma\mathbf{F}^{-T} = \mathbf{F}^{-1}\mathbf{P}, \tag{2.8}$$

where $J = \det \mathbf{F}$ is the determinant of the deformation gradient tensor. This stress

tensor is particularly useful as it is symmetric and defined purely on the reference configuration.

2.1.3. Balance equations

The classical balance equations in continuum mechanics are the conservation of mass, the balance of linear and angular momentum and the balance of energy. Additionally, the entropy inequality principle is introduced, which gives the direction of energy transfer.

It is assumed that the continuum body B is a closed system, *i.e.*, a system that does not allow mass transfer across its boundaries. The mass m of such a system must be conserved throughout its motion. This is expressed by the conservation of mass

$$m = \int_{V^0} \rho^0(\mathbf{X})\, dV = \int_V \rho(\mathbf{x}, t)\, dv = \text{const}, \tag{2.9}$$

where ρ^0 is the reference mass density and ρ is the current mass density.

The balance of linear momentum (written in terms of the current configuration) is

$$\frac{D}{Dt} \int_V \rho \mathbf{v}\, dv = \int_{\partial V} \mathbf{t}\, ds + \int_V \rho \mathbf{b}\, dv, \tag{2.10}$$

where $D(\bullet)/Dt$ is the material time derivative, $\mathbf{t}$ is the Cauchy traction vector and $\rho\mathbf{b}$ is the body force per unit current volume. Together with Cauchy's law $\mathbf{t} = \boldsymbol{\sigma}\mathbf{n}$, the conservation of mass and the divergence theorem, the balance of linear momentum leads to Cauchy's famous first equation of motion

$$\int_V \left(\mathrm{div}\boldsymbol{\sigma} + \rho\mathbf{b} - \rho \frac{\mathrm{D}\mathbf{v}}{\mathrm{D}t} \right) dv = \mathbf{0}. \tag{2.11}$$

In terms of the reference configuration, the equivalent equation is found as

$$\int_{V^0} \left(\mathrm{Div}\mathbf{P} + \rho^0\mathbf{b} - \rho^0 \frac{\partial \mathbf{v}(\mathbf{X}, t)}{\partial t} \right) dV = \mathbf{0}. \tag{2.12}$$

The balance of angular momentum (written in terms of the current configuration) is

$$\frac{D}{Dt} \int_V (\mathbf{x} - \mathbf{x}^0) \times \rho\mathbf{v}\, dv = \int_{\partial V} (\mathbf{x} - \mathbf{x}^0) \times \mathbf{t}\, ds + \int_V (\mathbf{x} - \mathbf{x}^0) \times \rho\mathbf{b}\, dv, \tag{2.13}$$

where $\mathbf{x}^0$ is an arbitrary fixed point. An important consequence of the balance of angular momentum is the symmetry of the Cauchy stress tensor $\boldsymbol{\sigma} = \boldsymbol{\sigma}^T$.

When considering mechanical and thermal energy contributions, the balance of energy (*i.e.*, the first law of thermodynamics, written in terms of the current configuration) is[1]

$$\frac{D}{Dt}\int_V \left(\frac{1}{2}\rho\mathbf{v}^2 + u\right) dv = \int_{\partial V} (\mathbf{t}\cdot\mathbf{v} - \mathbf{q}\cdot\mathbf{n})\, ds + \int_V (\mathbf{b}\cdot\mathbf{v} + \rho r)\, dv, \tag{2.14}$$

where u is the internal energy per unit current volume, $\mathbf{q}$ is the heat flux per unit current surface area and ρr is the heat source per unit current volume. As the balance of energy does not include any information about the physical direction of energy transfer, an additional principle is needed, which is the entropy inequality principle (the second law of thermodynamics). It reads as

$$\frac{D}{Dt}\int_V \eta(\mathbf{x},t)\, dv + \int_{\partial V} \mathbf{h}\cdot\mathbf{n}\, ds - \int_V \tilde{r}\, dv \geq 0, \tag{2.15}$$

where η is the entropy per unit current volume, $\mathbf{h}$ is the Cauchy entropy flux per unit current surface area and $\tilde{r}$ is the entropy source per unit time and per unit current volume. Another form of the second law of thermodynamics is the Clausius-Duhem inequality

$$\frac{D}{Dt}\int_V \eta(\mathbf{x},t)\, dv + \int_{\partial V} \frac{\mathbf{q}}{T}\cdot\mathbf{n}\, ds - \int_V \rho\frac{r}{T}\, dv \geq 0, \tag{2.16}$$

which uses the well known relation linear relations of the entropy flux and entropy source with the heat flux and heat source through the proportional factor $\frac{1}{T}$, where T is the total temperature.

2.1.4. Principle of virtual work and finite element approximation

The principle of virtual work (*i.e.*, the weak form of the balance of linear momentum) written in terms of the reference configuration (Eq. 2.12) is (see, *e.g.*, Belytschko, Liu, and Moran, 2000)

$$\int_{V^0} \left(\mathbf{P} : \delta\mathbf{F} - \rho^0\delta\mathbf{u}\cdot\mathbf{b} + \rho\delta\mathbf{u}\cdot\ddot{\mathbf{u}}\right) dV - \sum_{i=1}^{N^{\mathrm{d}}} \int_{\partial V^{0,\sigma,i}} (\delta\mathbf{u}\cdot\mathbf{e}^i)(\mathbf{e}^i\cdot\hat{\mathbf{T}})\, dS = 0, \tag{2.17}$$

where $\delta\mathbf{u}$ and $\delta\mathbf{F}$ are the first variations of the displacement field and the deformation gradient tensor, and $\hat{\mathbf{T}}$ is the prescribed first Piola-Kirchhoff traction vector specified

[1] In this thesis, only isentropic and isothermal processes are considered in the continuum. In the study of these processes, the balance of energy does not need to be considered but is still given here for completeness.

on a portion of the boundary $\partial V^{0,\sigma} \in \partial V^0$, often called the traction boundary. N^{d} is the number of spatial dimension and $\mathbf{e}^i$ is the unit vector of the Cartesian coordinate system in i-direction.

An approximate solution to this non-linear equation is obtained by the finite element approximation, in which the domain V^0 is subdivided into a finite number of elements, *i.e.*, $V^0 = \bigcup_e V^{0,e}$ connected at the finite element nodes. In the finite element approximation, the motion is interpolated from the position at the finite element nodes $\mathbf{x}^I$ using known shape functions S

$$\mathbf{x}(\mathbf{X}, t) = \sum_{I=1}^{N^{\mathrm{nodes}}} S^I(\mathbf{X})\mathbf{x}^I(t), \tag{2.18}$$

where N^{nodes} is the total number of finite element nodes in the domain. Likewise, the displacement field and its first variation as well as the velocity and acceleration fields are interpolated using their corresponding nodal values, *i.e.*,

$$\mathbf{u}(\mathbf{X}, t) = \sum_{I=1}^{N^{\mathrm{nodes}}} S^I(\mathbf{X})\mathbf{u}^I(t), \qquad \delta\mathbf{u}(\mathbf{X}, t) = \sum_{I=1}^{N^{\mathrm{nodes}}} S^I(\mathbf{X})\mathbf{u}^I(t), \tag{2.19}$$

$$\dot{\mathbf{u}}(\mathbf{X}, t) = \sum_{I=1}^{N^{\mathrm{nodes}}} S^I(\mathbf{X})\dot{\mathbf{u}}^I(t), \qquad \ddot{\mathbf{u}}(\mathbf{X}, t) = \sum_{I=1}^{N^{\mathrm{nodes}}} S^I(\mathbf{X})\ddot{\mathbf{u}}^I(t). \tag{2.20}$$

Using the finite element approximation, the principle of virtual work can be rewritten to yield the well-known equation of motion

$$\mathbf{M}^{IJ}\ddot{\mathbf{u}}^J + \mathbf{f}^{\mathrm{int},I} = \mathbf{f}^{\mathrm{ext},I} \quad \text{or} \quad \mathbf{M}\ddot{\mathbf{u}} + \mathbf{f}^{\mathrm{int}} = \mathbf{f}^{\mathrm{ext}}, \tag{2.21}$$

where $\mathbf{M}^{IJ}$ is the mass matrix

$$\mathbf{M}^{IJ} = \mathbf{I}\int_{V^0} \rho^0 S^I S^J \, dV \tag{2.22}$$

and $\mathbf{f}^{\mathrm{int},I}$ and $\mathbf{f}^{\mathrm{ext},I}$ are the internal and external nodal forces

$$\mathbf{f}^{\mathrm{int},I} = \int_{V^0} \frac{\partial S^I}{\partial \mathbf{X}}\mathbf{P}\, dV = \int_{V^0} \frac{\partial S^I}{\partial \mathbf{X}}\mathbf{F}\mathbf{S}\, dV, \tag{2.23}$$

$$\mathbf{f}^{\mathrm{ext},I} = \int_{V^0} S^I \rho^0 \mathbf{b}\, dV + \int_{\partial V^{0,\sigma,i}} S^I \mathbf{e}^i \hat{\mathbf{T}}\, dS\,. \tag{2.24}$$

The quantities $\mathbf{M}$, $\ddot{\mathbf{u}}$, $\mathbf{f}^{\mathrm{int}}$ and $\mathbf{f}^{\mathrm{ext}}$ are the global mass matrix, and column matrices of the acceleration and the internal and external nodal forces, respectively. In practice, the so called consistent mass matrix presented here is often replaced by a diagonal matrix called the lumped mass matrix (see, *e.g.*, Zienkiewicz and Taylor, 2000). As shown

in the definition of the internal nodal forces (Eq. 2.23), the first Piola-Kirchhoff stress tensor $\mathbf{P}$ is often exchanged for the second Piola-Kirchhoff stress $\mathbf{S}$ for convenience, using the inverse of the relation given in Eq. 2.8.

The integrals in Eqns. 2.22-2.24 above are commonly evaluated numerically using Gauss quadrature

$$\int_{-1}^{1} f(x)\,dx \approx \sum_{i=1}^{N^{\mathrm{q}}} w^{\mathrm{q},i} f(x^{\mathrm{q},i}), \tag{2.25}$$

here shown for the standard interval of $[-1, 1]$, with known weights w^i and coordinates $x^{\mathrm{q},i}$ of the N^{q} integration (or Gauss) points.

In the special case of static or quasi-static problems, the inertia term in the equations of motion Eq. 2.21 vanishes and the resulting discrete equilibrium equation reads

$$\mathbf{f}^{\mathrm{int}} = \mathbf{f}^{\mathrm{ext}}. \tag{2.26}$$

Up to this point, the finite element equations are independent of the material studied and thus of the constitutive relation, *i.e.*, the relation of stresses and strains. The constitutive relation comes into play in the internal nodal forces. In this thesis, only hyperelastic material (see, *e.g.*, Tadmor, Miller, and Elliott, 2011) is considered, for which a strain energy density W exists, from which the stress can be obtained by derivation with respect to the conjugate deformation measure. The conjugate deformation measure of the second Piola-Kirchhoff stress tensor $\mathbf{S}$ is the Green-Lagrange strain tensor $\mathbf{E}$ (see, *e.g.*, Belytschko, Liu, and Moran, 2000), and thus

$$\mathbf{S} = \frac{\partial W(\mathbf{S}, \mathbf{E})}{\partial \mathbf{E}}. \tag{2.27}$$

Also, the material tangent (in this case the Lagrangian elasticity tensor $\mathbb{C}$) can be found as a second derivative of the strain energy density with respect to the Green-Lagrange strain tensor, *i.e.*,

$$\mathbb{C} = \frac{\partial^2 W(\mathbf{S}, \mathbf{E})}{\partial \mathbf{E}^2} = \frac{\partial \mathbf{S}}{\partial \mathbf{E}}. \tag{2.28}$$

This quantity is needed in the solution of Eq. 2.21 and Eq. 2.26.

2.1.5. Solution techniques

The equation of motion (Eq. 2.21) may be solved using explicit (*e.g.*, the central difference method) or implicit time integration (*e.g.*, the Newmark β-method). For an overview of the most common time integration methods, see, *e.g.*, Belytschko, Liu, and Moran

(2000). One algorithm which can also be used for explicit time integration is the Velocity Verlet algorithm, presented in Section 2.2.4.

The equilibrium equation (Eq. 2.26) generally is a nonlinear equation, which is commonly solved iteratively using the Newton-Raphson (NR) algorithm (see, *e.g.*, Zienkiewicz and Taylor, 2000). The NR algorithm will be briefly presented here for further reference. Before going into details, we first acknowledge the fact that the internal forces are generally nonlinear functions of the displacements $\mathbf{u}$, *i.e.*, $\mathbf{f}^{\text{int}} = \mathbf{f}^{\text{int}}(\mathbf{u})$.[2] Second, we assume so-called deadloading (*i.e.*, the external loading is independent of the deformation). In this case, the external forces are independent of the displacements. The equilibrium equation (Eq. 2.26) may thus be rearranged as

$$\mathbf{f}^{\text{ext}} - \mathbf{f}^{\text{int}}(\mathbf{u}) = \mathbf{0} = \mathbf{r}(\mathbf{u}), \tag{2.29}$$

where $\mathbf{r}$ is called a residual. Starting from a state of equilibrium at a discrete instance of time t^k, the Newton-Raphson algorithm aims to find the next state of equilibrium at t^{k+1}

$$\mathbf{r}^{k+1} = \mathbf{r}(\mathbf{u}^{k+1}) = \mathbf{f}^{\text{ext},k+1} - \mathbf{f}^{\text{int}}(\mathbf{u}^{k+1}) = \mathbf{0}, \tag{2.30}$$

by using a first order approximation of the residual

$$\mathbf{r}(\mathbf{u}^{k+1,(n+1)}) \approx \mathbf{r}(\mathbf{u}^{k+1,(n)}) + \left(\frac{\partial \mathbf{r}}{\partial \mathbf{u}}\right)^{k+1,(n)} \Delta\mathbf{u}^{k+1,(n)} = \mathbf{0}, \tag{2.31}$$

where n is the iteration and $\Delta\mathbf{u}^{k+1,(n)} = \mathbf{u}^{k+1,(n+1)} - \mathbf{u}^{k+1,(n)}$.

In this equation,

$$\mathbf{K} = -\frac{\partial \mathbf{r}}{\partial \mathbf{u}} = \frac{\partial \mathbf{f}^{\text{int}}}{\partial \mathbf{u}} \tag{2.32}$$

is called the stiffness matrix. In the derivation of this matrix (see, *e.g.*, Belytschko, Liu, and Moran, 2000), an explicit dependence on the stress measure (in this case $\mathbf{S}$) and on the material tangent (in this case $\mathbb{C}$) is revealed, *i.e.*, $\mathbf{K} = \mathbf{K}(\mathbf{S}, \mathbb{C})$.

After rearrangement of Eq. 2.31, the well-known iterative scheme

$$\mathbf{u}^{k+1,(n+1)} = \mathbf{u}^{k+1,(n)} + \left(\mathbf{K}^{k+1,(n)}\right)^{-1} \left(\mathbf{f}^{\text{ext},k+1} - \mathbf{f}^{\text{int}}(\mathbf{u}^{k+1,(n)})\right) \tag{2.33}$$

is found, which can be written more concisely by dropping the discrete time index as

$$\mathbf{u}^{(n+1)} = \mathbf{u}^{(n)} + \left(\mathbf{K}^{(n)}\right)^{-1} \left(\mathbf{f}^{\text{ext}} - \mathbf{f}^{\text{int}}(\mathbf{u}^{(n)})\right). \tag{2.34}$$

[2] As can be seen from Eq. 2.23, the internal nodal forces do not explicitly depend on the displacements, but rather, the dependence is implicitly included in the constitutive relation, *i.e.*, $\mathbf{S} = \mathbf{S}(\mathbf{E})$, $\mathbf{E} = \mathbf{E}(\mathbf{F})$, $\mathbf{F} = \mathbf{F}(\mathbf{u})$.

2.2. Statistical mechanics

This section gives a brief introduction into classical statistical mechanics and molecular dynamics. For further information, see, *e.g.*, Chandler and Wu (1987); Allen and Tildesley (1989); Frenkel and Smit (2001); Weiner (2002); Tuckerman (2010); Tadmor and Miller (2011).

Classical statistical mechanics aims to predict the macroscopic properties of many-body systems composed of classical particles (*e.g.*, atomic systems) based on the microscopic interactions and thus offers a microscopic foundation of thermodynamics. The rationale behind the theory is that the macroscopic properties of a many-body system do not explicitly depend on the specific behavior of every particle in the system, but rather reflect some kind of average behavior of the particles. The microscopic configuration of a system of N particles at time t is sufficiently characterized by the $3N$ particle positions $\mathbf{r}^1, \ldots, \mathbf{r}^N$ and the $3N$ particle momenta $\mathbf{p}^1, \ldots, \mathbf{p}^N$, where $\mathbf{p}^\alpha = m^\alpha \dot{\mathbf{r}}^\alpha$, with m^α being the particle mass and $\dot{\mathbf{r}}^\alpha = \frac{d\mathbf{r}^\alpha}{dt}$ being the particle velocity. These $6N$ quantities can be regarded as a specific point described by a vector $(\mathbf{r}^1, \ldots, \mathbf{r}^N, \mathbf{p}^1, \ldots, \mathbf{p}^N)$ in a $6N$-dimensional space, called the phase space Γ.

2.2.1. The concepts of statistical ensembles, ensemble averages and time averages

Intuition tells us, that there must be a large number of microscopic configurations of a many-body system, which fit to a set of given macroscopic constraints. For example, if the macroscopic constraint is the systems' total energy, it is immediately clear that there must exist a large number of different position and velocity distributions among the particles, which give rise to the same total energy. The collection of this large number of microscopic configurations is called an ensemble.

All microscopic configurations which belong to the same ensemble represent different points in phase space. A macroscopic property (a macroscopic observable) $\mathcal{A}$ at time τ may be found from an ensemble average as

$$\mathcal{A} = \langle A(\mathbf{r}, \mathbf{p}) \rangle = \int_\Gamma A(\mathbf{r}, \mathbf{p}) f(\mathbf{r}, \mathbf{p}, \tau)\, d\mathbf{r}\, d\mathbf{p}, \tag{2.35}$$

where $A(\mathbf{r}, \mathbf{p})$ is a corresponding microscopic phase space function and $f(\mathbf{r}, \mathbf{p}, \tau)$ is the phase space distribution function which satisfies $\int_\Gamma = f(\mathbf{r}, \mathbf{p}, \tau)\, d\mathbf{r}\, d\mathbf{p} = 1$.

This is tantamount to performing an average over all accessible microscopic configurations of the ensemble at a given time. A numerical realization to compute such ensemble averages is found in the Markov-Chain-Monte-Carlo methods.

The ergodic hypothesis implies that ensemble averages may be replaced by time averages of the form

$$\mathcal{A} = \overline{A(\mathbf{r}, \mathbf{p})} = \lim_{\tau^e \to \infty} \frac{1}{\tau^e} \int_0^{\tau^e} A(\mathbf{r}(\tau), \mathbf{p}(\tau))\, d\tau \,. \tag{2.36}$$

Here, in contrast to an ensemble average, not all accessible microscopic configurations are observed at a given time, but rather the trajectory of a single system in phase space is followed over time. This single system will take every accessible microscopic configuration in the observed period of time τ^e. A numerical realization to compute such time averages is found in the molecular dynamics simulation technique presented in Section 2.2.4.

The two most important ensembles are the microcanonical and the canonical ensemble which are briefly presented below. For information on various other ensembles such as the isobaric ensemble or the grand canonical ensemble, see, *e.g.*, Tuckerman (2010).

2.2.2. Microcanonical ensemble

The microcanonical ensemble is the collection of isolated systems (*i.e.*, systems which do no exchange heat or particles with its surroundings) of N identical particles in a container of volume Ω with fixed total energy E (see Fig. 2.3).[3]

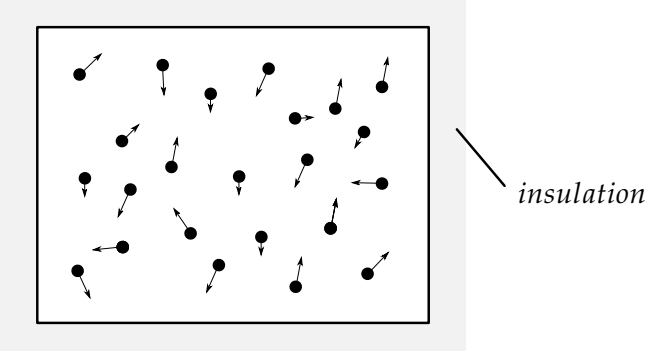

Fig. 2.3.: An isolated system of particles.

[3]Hence, the three macroscopic constraints of the system are N, Ω and E, which is why the microcanonical ensemble is also called the $N\Omega E$-ensemble.

Using the fundamental assumption of equal *a priori* probability (which assumes that for isolated systems in equilibrium, all accessible microscopic configurations are equally probable), the microcanonical ensemble average of a macroscopic observable A can be obtained as (Tuckerman, 2010)

$$\mathcal{A} = \langle A(\mathbf{r}, \mathbf{p}) \rangle = \frac{\int_\Gamma A(\mathbf{r}, \mathbf{p}) \delta(\mathcal{H}(\mathbf{r}, \mathbf{p}) - E)\, d\mathbf{r}\, d\mathbf{p}}{\int_\Gamma \delta(\mathcal{H}(\mathbf{r}, \mathbf{p}) - E)\, d\mathbf{r}\, d\mathbf{p}}. \tag{2.37}$$

In this equation, δ is the Dirac δ-function and $\mathcal{H}(\mathbf{r}, \mathbf{p})$ is the physical Hamiltonian of the many-body system

$$\mathcal{H}(\mathbf{r}, \mathbf{p}) = \mathcal{U}(\mathbf{r}^1, \ldots, \mathbf{r}^N) + \sum_{\alpha=1}^{N} \frac{1}{2m^\alpha} \mathbf{p}^\alpha \cdot \mathbf{p}^\alpha, \tag{2.38}$$

where the first term is the potential energy of the system and the second term is the kinetic energy of the system. The Lagrangian of the many-body system is found through the Legendre transformation as

$$\mathcal{L} = \sum_{\alpha=1}^{N} \mathbf{p}^\alpha \cdot \dot{\mathbf{r}}^\alpha - \mathcal{H}. \tag{2.39}$$

2.2.3. Canonical ensemble

As most real world experiments are conducted at a fixed temperature rather than at a fixed energy, the canonical, or $N\Omega T$-ensemble is of great importance to describe how the macroscopic observables measured in experiments are connected to the microscopic constituents. The basic idea to generate such an ensemble is to consider a system (system 1) embedded in its surroundings (system 2) such that the two systems can only exchange heat.

The total system (system 1 and system 2) is part of the microcanonical ensemble, and thus its energy $E = E^1 + E^2$ is conserved. The energies of the systems 1 and 2 can fluctuate. By assuming that system 2 is much larger than system 1 (system 2 is a "thermal reservoir" or "heatbath", *i.e.*, $N^2 \gg N^1$, $\Omega^2 \gg \Omega^1$, $E^2 \gg E^1$), the canonical ensemble average can be obtained as (see, *e.g.*, Tuckerman, 2010)

$$\mathcal{A} = \langle A(\mathbf{r}, \mathbf{p}) \rangle = \frac{\int_\Gamma A(\mathbf{r}, \mathbf{p}) \exp\left(-\beta \mathcal{H}(\mathbf{r}, \mathbf{p})\right) d\mathbf{r}\, d\mathbf{p}}{\int_\Gamma \exp\left(-\beta \mathcal{H}(\mathbf{r}, \mathbf{p})\right) d\mathbf{r}\, d\mathbf{p}}, \tag{2.40}$$

where the so-called thermodynamic beta $\beta = 1/(k^{\mathrm{B}} T)$ is used, with k^{B} being the Boltzmann constant and T being the total temperature of the thermal reservoir.

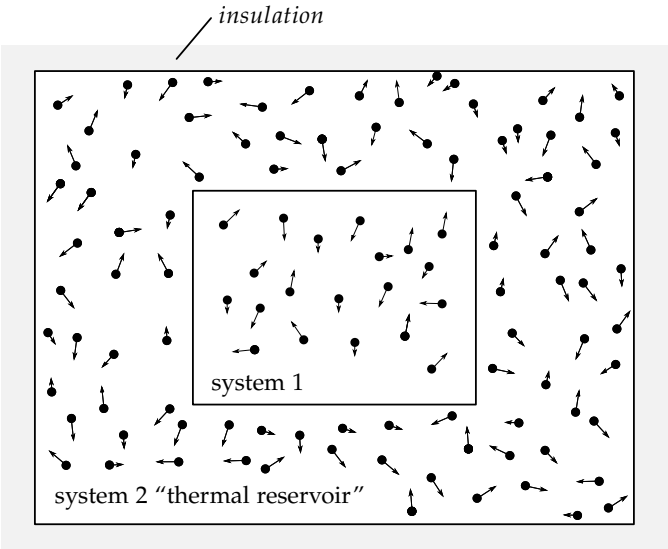

Fig. 2.4.: Two systems in contact. The total system is isolated.

2.2.4. Molecular dynamics

Molecular dynamics is a numerical simulation technique, which allows to study the evolution of a system of atoms over time via time integration of the atomic equations of motion. The system is subject to macroscopic constraints (*e.g.*, N, Ω, E in the microcanonical ensemble or N, Ω, T in the canonical ensemble) and spatial boundary conditions, which define the shape and the interaction of the atoms with its surroundings. Various spatial boundary conditions exist, such as vacuum boundary conditions (a system of atoms surrounded by vacuum) or periodic boundary conditions (a system of atoms interacting with an infinite array of adjacent copies of the system). The interaction between the atoms is governed through interatomic potentials.

Interatomic potentials

In the absence of externally applied potential fields, the potential energy of a system of atoms can be written as the series expansion

$$\mathcal{U}(\mathbf{r}^1, \ldots, \mathbf{r}^N) = \frac{1}{2!} \sum_{\substack{\alpha,\beta=1 \\ \alpha \neq \beta}}^{N} \mathcal{U}^{\text{pair}}(\mathbf{r}^\alpha, \mathbf{r}^\beta) + \frac{1}{3!} \sum_{\substack{\alpha,\beta,\gamma=1 \\ \alpha \neq \beta \neq \gamma \neq \alpha}}^{N} \mathcal{U}^3(\mathbf{r}^\alpha, \mathbf{r}^\beta, \mathbf{r}^\gamma) + \ldots, \tag{2.41}$$

where $\mathcal{U}^{\text{pair}}$ is a two-body term, $\mathcal{U}^3$ is a three-body term, *etc*.

Interatomic potentials give approximations to the potential energy of the atomic system which allow one to derive interatomic forces via $\mathbf{f}^\alpha = -\frac{\partial \mathcal{U}}{\partial \mathbf{r}^\alpha}$. There exists a vast amount of interatomic potentials, suitable to study numerous materials.

An example of a pair-potential is the Lennard-Jones potential (Jones and Chapman, 1924)

$$\mathcal{U}(\mathbf{r}^1, \ldots, \mathbf{r}^N) \approx \frac{1}{2!} \sum_{\substack{\alpha,\beta=1 \\ \alpha \neq \beta}}^{N} \mathcal{U}^{\text{pair,LJ}}(r^{\alpha\beta}) = \frac{1}{2!} \sum_{\substack{\alpha,\beta=1 \\ \alpha \neq \beta}}^{N} 4\varepsilon \left[\left(\frac{\sigma}{r^{\alpha\beta}} \right)^{12} - \left(\frac{\sigma}{r^{\alpha\beta}} \right)^{6} \right], \tag{2.42}$$

where ε is the depth of the potential well, σ is the distance at which the potential takes a value of zero and $r^{\alpha\beta}$ is the distance between two particles α and β.

An example of a multi-body potential is the Embedded Atom Model (EAM) (Daw and Baskes, 1984)

$$\mathcal{U}^{\text{EAM}}(\mathbf{r}^1, \ldots, \mathbf{r}^N) \approx \sum_{\alpha=1}^{N} F^\alpha \left(\sum_{\substack{\beta=1 \\ \beta \neq \alpha}}^{N} \rho^{\text{EAM}}(r^{\alpha\beta}) \right) + \frac{1}{2!} \sum_{\substack{\alpha,\beta=1 \\ \alpha \neq \beta}} \mathcal{U}^{\text{pair,EAM}}(r^{\alpha\beta}), \tag{2.43}$$

where F^α is an embedding energy function, which depends on the sum of the electron charge densities $\rho^{\text{EAM}}(r^{\alpha\beta})$ and $\mathcal{U}^{\text{pair,EAM}}$ is a pair-potential similar to the Lennard-Jones potential.

Molecular dynamics and the microcanonical ensemble

The Hamiltonian equations of motion of a system, which generates microscopic configurations of the microcanonical ensemble, can be derived from the physical Hamiltonian (Eq. 2.38) as (Tuckerman, 2010)

$$\dot{\mathbf{r}}^\alpha = \frac{\partial \mathcal{H}}{\partial \mathbf{p}^\alpha} = \frac{\mathbf{p}^\alpha}{m^\alpha}, \qquad \dot{\mathbf{p}}^\alpha = -\frac{\partial \mathcal{H}}{\partial \mathbf{r}^\alpha} = -\frac{\partial \mathcal{U}}{\partial \mathbf{r}^\alpha}. \tag{2.44}$$

These equations of motion conserve the Hamiltonian $\mathcal{H}(\mathbf{r}, \mathbf{p})$, which corresponds to the system's total energy E. They are simply a different form of the famous Newtonian equations of motion

$$m^\alpha \ddot{\mathbf{r}}^\alpha = -\frac{\partial \mathcal{U}}{\partial \mathbf{r}^\alpha}, \tag{2.45}$$

which can also be obtained from the Lagrangian $\mathcal{L}$ (Eq. 2.39) via the Euler-Lagrange equation $d/dt\,(\partial \mathcal{L}/\partial \dot{\mathbf{r}}) - \partial \mathcal{L}/\partial \mathbf{r} = \mathbf{0}$. Therefore, using the Newtonian equations of

motion in molecular dynamics automatically results in a system, which generates microscopic configurations of the microcanonical ensemble. There exist different time integration methods to integrate the equations of motion in molecular dynamics, which can, however, never exactly conserve the Hamiltonian $\mathcal{H}(\mathbf{r}, \mathbf{p})$ due to discretization errors.

Algorithms suitable for molecular dynamics must however satisfy the symplectic condition, which means that they conserve a so-called shadow Hamiltonian $\tilde{\mathcal{H}}(\mathbf{r}, \mathbf{p})$ which remains close to the true Hamiltonian $\mathcal{H}(\mathbf{r}, \mathbf{p})$ (Tuckerman, 2010). One time integration algorithm which is commonly used is the velocity Verlet algorithm (Swope *et al.*, 1982)

$$\mathbf{r}^{\alpha}(\tau + \Delta\tau) = \mathbf{r}^{\alpha}(\tau) + \dot{\mathbf{r}}^{\alpha}(\tau)\Delta\tau + \frac{\Delta\tau^2}{2m^{\alpha}}\mathbf{f}^{\alpha}(\tau), \tag{2.46}$$

$$\dot{\mathbf{r}}^{\alpha}(\tau + \Delta\tau) = \dot{\mathbf{r}}^{\alpha}(\tau) + \frac{\Delta\tau}{2m^{\alpha}}(\mathbf{f}^{\alpha}(\tau) + \mathbf{f}^{\alpha}(\tau + \Delta\tau)), \tag{2.47}$$

in these equations, $\Delta\tau$ is the numerical time step and $\mathbf{f}^{\alpha} = m^{\alpha}\ddot{\mathbf{r}}^{\alpha} = \dot{\mathbf{p}}^{\alpha} = -\frac{\partial \mathcal{U}}{\partial \mathbf{r}^{\alpha}}$ is the force on particle α. Another algorithm is the Gear sixth-order predictor-corrector scheme (Allen and Tildesley, 1989), which consists of a predictor step

$$\begin{bmatrix} {}^0\mathbf{r}^{\mathrm{P},\alpha}(\tau+\Delta\tau) \\ {}^1\mathbf{r}^{\mathrm{P},\alpha}(\tau+\Delta\tau) \\ {}^2\mathbf{r}^{\mathrm{P},\alpha}(\tau+\Delta\tau) \\ {}^3\mathbf{r}^{\mathrm{P},\alpha}(\tau+\Delta\tau) \\ {}^4\mathbf{r}^{\mathrm{P},\alpha}(\tau+\Delta\tau) \\ {}^5\mathbf{r}^{\mathrm{P},\alpha}(\tau+\Delta\tau) \end{bmatrix} = \begin{bmatrix} 1 & 1 & 1 & 1 & 1 & 1 \\ 0 & 1 & 2 & 3 & 4 & 5 \\ 0 & 0 & 1 & 3 & 6 & 10 \\ 0 & 0 & 0 & 1 & 4 & 10 \\ 0 & 0 & 0 & 0 & 1 & 5 \\ 0 & 0 & 0 & 0 & 0 & 1 \end{bmatrix} \begin{bmatrix} {}^0\mathbf{r}^{\alpha}(\tau) \\ {}^1\mathbf{r}^{\alpha}(\tau) \\ {}^2\mathbf{r}^{\alpha}(\tau) \\ {}^3\mathbf{r}^{\alpha}(\tau) \\ {}^4\mathbf{r}^{\alpha}(\tau) \\ {}^5\mathbf{r}^{\alpha}(\tau) \end{bmatrix} \tag{2.48}$$

and a corrector step,

$$\begin{bmatrix} {}^0\mathbf{r}^{\mathrm{C},\alpha}(\tau+\Delta\tau) \\ {}^1\mathbf{r}^{\mathrm{C},\alpha}(\tau+\Delta\tau) \\ {}^2\mathbf{r}^{\mathrm{C},\alpha}(\tau+\Delta\tau) \\ {}^3\mathbf{r}^{\mathrm{C},\alpha}(\tau+\Delta\tau) \\ {}^4\mathbf{r}^{\mathrm{C},\alpha}(\tau+\Delta\tau) \\ {}^5\mathbf{r}^{\mathrm{C},\alpha}(\tau+\Delta\tau) \end{bmatrix} = \begin{bmatrix} {}^0\mathbf{r}^{\mathrm{P},\alpha}(\tau+\Delta\tau) \\ {}^1\mathbf{r}^{\mathrm{P},\alpha}(\tau+\Delta\tau) \\ {}^2\mathbf{r}^{\mathrm{P},\alpha}(\tau+\Delta\tau) \\ {}^3\mathbf{r}^{\mathrm{P},\alpha}(\tau+\Delta\tau) \\ {}^4\mathbf{r}^{\mathrm{P},\alpha}(\tau+\Delta\tau) \\ {}^5\mathbf{r}^{\mathrm{P},\alpha}(\tau+\Delta\tau) \end{bmatrix} + \begin{bmatrix} 3/16 \\ 251/360 \\ 1 \\ 11/18 \\ 1/6 \\ 1/60 \end{bmatrix} \left({}^2\mathbf{r}^{\mathrm{C},\alpha} - {}^2\mathbf{r}^{\mathrm{P},\alpha} \right), \tag{2.49}$$

where the unique notation

$${}^n\mathbf{r}^{\alpha} = \frac{(\Delta\tau)^n}{n!}\frac{d^n\,\mathbf{r}^{\alpha}(\tau)}{d\tau^n} \tag{2.50}$$

is used and where ${}^2\mathbf{r}^{\mathrm{C},\alpha}$ is calculated by substituting ${}^0\mathbf{r}^{\mathrm{P},\alpha}$ into the equations of motion (Eq. 2.45).

Molecular dynamics and the canonical ensemble

There are many different approaches to study a system with molecular dynamics, which generates microscopic configurations of the canonical ensemble. These approaches are commonly known as thermostats (for an excellent review see, *e.g.*, Hünenberger, 2005). Widely used are the so-called extended phase space techniques, where additional variables are introduced into the physical phase space. An example is the Nosé-Hoover thermostat, which is governed by the Hamiltonian (Nosé, 1984; Hoover, 1985)

$$\mathcal{H}^{\mathrm{N}}(\mathbf{r},\mathbf{p}) = \mathcal{U}(\mathbf{r}^1,\ldots,\mathbf{r}^N) + \sum_{i=\alpha}^{N} \frac{1}{2m^\alpha s^2}\mathbf{p}^\alpha\cdot\mathbf{p}^\alpha + \frac{(p^s)^2}{2Q} + gk^{\mathrm{B}}T^\infty \ln s, \tag{2.51}$$

where s and p^s are two additional variables in the phase space that mimic the thermal reservoir, Q is a thermal "mass", g is the number of independent momentum degrees of freedom and T^∞ is the temperature of the thermal reservoir. The equations of motion of the Nosé-Hoover thermostat can, *e.g.*, be found in Tuckerman (2010). Another example of an extended phase space technique is presented in Chapter 4 for the isostress-isothermal ensemble.

An example of a thermostat which does not belong to the extended phase space techniques is the so-called Langevin thermostat. The equations of motion of the Langevin thermostat are (see, *e.g.*, Tuckerman, 2010)

$$m^\alpha\ddot{\mathbf{r}}^\alpha = -\frac{\partial\mathcal{U}}{\partial\mathbf{r}^\alpha} - m^\alpha\gamma\dot{\mathbf{r}}^\alpha + \mathbf{f}^{\mathrm{r}}, \tag{2.52}$$

where γ is a damping coefficient. The Langevin thermostat introduces damping forces $-m^\alpha\gamma\dot{\mathbf{r}}^\alpha$ and a random forces $\mathbf{f}^{\mathrm{r}}$, which are related by the dissipation-fluctuation theorem (Kantorovich, 2008a; Kantorovich, 2008b). As the random nature of the Langevin thermostat perturbs the systems' dynamics, it is often only used close to the system boundary, an approach which is known as stochastic boundary conditions. A version of the stochastic boundary conditions known as "Stadium damping" uses a spatially varying damping coefficient $\gamma = \gamma(\mathbf{x})$, with increasing values towards the outer boundary of the system (Holian and Ravelo, 1995; Qu *et al.*, 2005).

The time integration algorithms presented in Section 2.2.4 can also be used to integrate the equations of motion of the Nosé-Hoover and the Langevin thermostat (with slight modifications due to the additional variables and additional terms).

3. State of the art in atomistic-to-continuum multiscale methods

Atomistic-to-continuum multiscale methods can be divided into two categories (see Fig. 3.1). On one hand, there are concurrent methods (Fig. 3.1a), in which the physical body of interest is spatially decomposed into at least one continuum and one atomistic region, which are coupled at spatial interfaces. These models are suitable for the study of problems which exhibit a strong coupling of the scales. If, on the other hand, a separation of the length and time scales can be assumed, the so-called hierarchical methods (Fig. 3.1b) can be used. In these methods, no spatial coupling of the scales exists and both scales are present everywhere in the body. The scales are coupled only through the exchange of effective information. The coarse scale obtains constitutive quantities or, in more ambitious models, even the structure of its governing equations, from the fine scale, whereas the fine scale receives its boundary conditions from the coarse scale.

3.1. Concurrent methods

In concurrent methods, only regions in which critical details occur, are modeled with atomistic resolution (fine scale). The rest of the body is assumed to be modeled sufficiently accurate as a continuum (coarse scale). There are numerous concurrent methods available in the literature. An attempt to categorize and benchmark some of the most prominent methods in the static, *i.e.*, $0K$ limit, was made by Miller and Tadmor (2009). An overview of static and dynamic, finite temperature methods was made by Tadmor and Miller (2011). A comparison of several methods for the study of fracture as well as for dislocation modeling and heat conduction was made by Iacobellis and Behdinan (2013) and Xu and Chen (2019), respectively. According to Miller and Tadmor (2009), most methods can be categorized using three characteristic properties: i) They can be divided by their governing formulation into energy-based and force-based methods. In energy-based methods, a potential single function exists from which the governing equations of both scales are derived. In force-based methods,

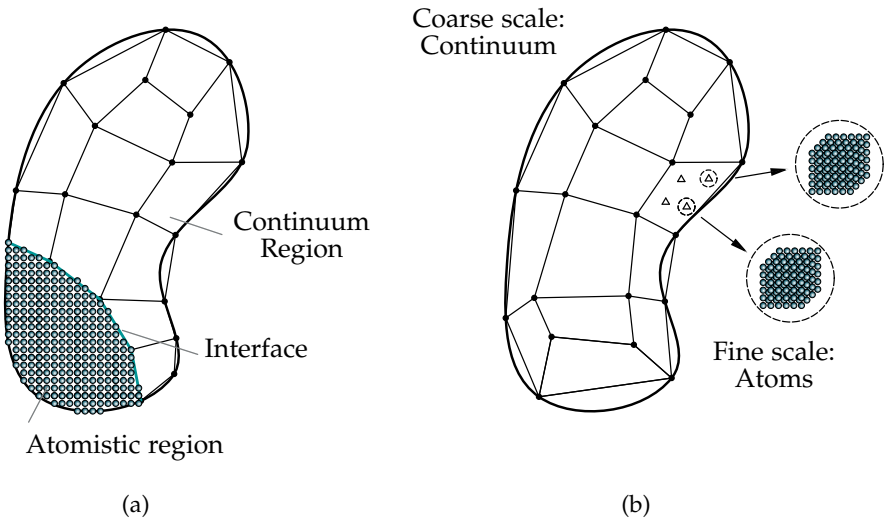

Fig. 3.1.: The classification of atomistic-to-continuum multiscale methods into (a) concurrent and (b) hierarchical methods.

no such potential function exists, and the coupling of the scales is defined at the level of forces. ii) The coupling of the regions at the spatial interface is highly non-trivial and subject of ongoing developments. Some methods use a sharp spatial interface, whereas other methods use a so-called handshake region, which is a transition region where some kind of mixing of the coarse and fine scale models exists. iii) The coupling between the scales may be performed using a strong compatibility, where the motion of both scales at the interface is in lock-step, or using weak compatibility, where the motion of the scales at the interface is only coupled in an averaged manner. Based on this categorization, the most important concurrent methods shall here be presented briefly.

The quasi-continuum (QC) method (Tadmor, Ortiz, and Phillips, 1996; Shenoy *et al.*, 1998; Shenoy *et al.*, 1999) is probably the most well-known atomistic-to-continuum multiscale method. It is an energy-based method with a sharp interface and a strong compatibility coupling. Finite temperature versions of QC have been published by Dupuy *et al.* (2005) and Tadmor *et al.* (2013). Several important improvements of the method have been proposed, *e.g.*, hyper-QC (Kim *et al.*, 2014), to overcome the time limitations of MD to accelerate the study of rare events or QCDFT (Lu, Tadmor, and Kaxiras, 2006), an extension to a quantum mechanical coupling.

The atomistic-to-continuum coupling in the coupling of length scales (CLS) method

(Abraham *et al.*, 1998; Broughton *et al.*, 1999; Abraham *et al.*, 2000) is very similar to the QC method. However, the CLS method additionally allows for an atomistic-to-quantum coupling by introducing atomistic regions which are modeled using the tight-binding approximation of quantum mechanics (Tadmor and Miller, 2011). The CLS method is inherently able to study dynamics and finite temperature.

The bridging domain method (BD) (Xiao and Belytschko, 2004) is an energy-based method which uses a handshake region with linear mixing of the atomistic and continuum energies. A weak compatibility coupling is employed using a Lagrange multiplier-based penalty method. A dynamic finite temperature version of BD was developed by Anciaux, Ramisetti, and Molinari (2012). Gracie and Belytschko (2009) and Gracie and Belytschko (2011) later combined the BD method with the extended finite element method (XFEM) for the modeling of dislocations and cracks.

The bridging scale method (BS) (Wagner and Liu, 2003; Qian, Wagner, and Liu, 2004) is an energy-based method with sharp interface and a mix between strong and weak compatibility coupling. The BS method conceptually differs from other concurrent methods, as it is envisioned that the displacements at every point of the body u consist of coarse-scale and fine-scale displacements $u = u' + u''$. Park, Karpov, and Liu (2004) extended the method to incorporate a finite temperature equation in the continuum.

The finite element/atomistic (FEAt) method (Kohlhoff, Gumbsch, and Fischmeister, 1991) was the first concurrent atomistic-to-continuum method published. It is a force-based method which uses a sharp interface and a strong compatibility coupling. While initially presented as capable of studying static and dynamic systems, it was later shown (Junge, Anciaux, and Molinari, 2015), that the dynamic version is unstable without additional precautions.

The atomistic-to-continuum (AtC) method (Fish *et al.*, 2007; Parks, Bochev, and Lehoucq, 2008; Badia *et al.*, 2008) is a force-based method which uses a handshake region with a linear mixing of the atomistic and continuum forces and a weak compatibility coupling. The method was developed for studying static systems and, to the author's best knowledge, no dynamic, finite temperature version of this method exists. The existence of another, unrelated, method (Wagner *et al.*, 2008; Templeton, Jones, and Wagner, 2010) which is often also referred to by the same name in the literature (*e.g.*, by Xu and Chen, 2019) may unfortunately lead to confusion. Whereas the first method only adopts a mechanical coupling between the scales, the latter method enables the study of a thermo-mechanical coupling with non-equilibrium heat transfer between the scales.

The Coupled Atomistic and Discrete Dislocation (CADD) method (Shilkrot, Miller, and Curtin, 2002; Shilkrot, Miller, and Curtin, 2004) is a force-based method which uses a sharp interface and a strong compatibility coupling. In fact, the coupling is essentially equivalent to the FEAt method. The unique feature of the CADD method

is that it allows crystal defects such as dislocations to exist not only in the atomistic but also in the continuum region by using the discrete dislocation methodology of Van der Giessen and Needleman (1995). Also, the method is able to perform a seamless two-way passing of defects over the spatial interface. Finite temperature versions of the method have been proposed by Qu *et al.* (2005); Shiari, Miller, and Curtin (2005), which either use a dynamic or quasi-static continuum model. Recently, the CADD method was extended from 2D to 3D (Anciaux *et al.*, 2018; Hodapp *et al.*, 2018; Cho *et al.*, 2018). The 2D finite temperature CADD method serves as a vehicle for the implementation of the two efficiency improvement approaches presented in Chapter 5 and Chapter 6 and is described in more detail in Section 5.2.1.

The concurrent atomistic-continuum (CAC) method (Xiong *et al.*, 2011; Chen, Shabanov, and McDowell, 2019) is also a force-based method with a strong compatibility and a sharp interface. In CAC, the continuum equations are derived directly from the atomistic behavior via an extension of the well-known Irving-Kirkwood procedure. The continuum is approximated with discontinuous finite elements, with the interatomic potential being the only constitutive relation. Due to the fact that the element faces are assumed to coincide with the glide planes of the atomic lattice, the method also allows the passing of dislocations between the scales (Xiong *et al.*, 2012).

3.2. Hierarchical methods

The hierarchical methods use a fundamentally different approach to multiscale modeling than the concurrent methods. In hierarchical methods, there exists no spatial decomposition of the body of interest into regions of different scales, and thus no spatial coupling between the scales. Instead, both scales exist everywhere in the body. The existing methods can be categorized by their general methodology into bottom-up and top-down methods, as well as by the way that information is passed between the scales into one- and two-way coupling methods.

Bottom-up methods aim to evolve the (*a priori* unknown) physics on the coarse-scale from the physics of a given fine-scale model. Top-down methods, on the other hand, assume that both the coarse-scale and fine-scale models and their governing equations are well defined *a priori*. In these methods, the fine-scale is required to deliver whatever data is missing in the coarse-scale computations. For top-down and bottom-up methods, general frameworks have been developed which provide general guidance on the proper design of the methods and provide means of uncertainty quantification for such methods.

In one-way coupling (or sequential) methods, the fine-scale model is executed in a pre-processing step, and thus there is only a one-way (fine- to coarse-scale) information

transport. The output of the fine-scale model (*e.g.*, missing data or the structure of the coarse-scale physics) is then used to perform the coarse-scale computations in a subsequent step. In two-way coupling methods, the fine-scale and coarse-scale computations are performed simultaneously with a two-way information transport. In these methods, the fine-scale model may, for example, be constrained by the current local macrostate at every discrete instance of coarse-scale time. This would be the information transport from the coarse to the fine scale. The missing data to evolve the coarse scale physics may then be extracted on the fly from the fine-scale model computations, which gives the information transport in the other direction.

The so-called equation-free approach (Kevrekidis *et al.*, 2003; Chen *et al.*, 2004; Kevrekidis, Gear, and Hummer, 2004) is a framework for bottom-up, two-way coupling methods to be used when a closed form of the coarse-scale evolution equations exists in principle, but is unavailable. The aim is to estimate the data that would be missing in the closed form of the macroscopic evolution equations by a series of properly designed experiments on the fine scale, spatial interpolation and temporal extrapolation.

An example of a top-down method with two-way coupling is the Generalized Mathematical Homogenization (GMH) approach (Chen and Fish, 2006; Fish, Chen, and Li, 2007; Li, Li, and Fish, 2008). In this approach, the coarse scale evolution equations are integrated by solving a molecular dynamics-like dynamic unit cell problem located in every Gauss point of the coarse scale. The dynamic unit cell problem is subject to the local deformation gradient and temperature on the coarse scale. The method was later included into the Adaptive Generalized Mathematical Homogenization (AGMH) framework, which combines both hierarchical and concurrent elements. AGMH focuses on the study of a collection of nanograins, where dislocation-free grains are modeled as a hierarchical continuum (Li, Li, and Fish, 2008) and grains containing dislocations are modeled with molecular dynamics.

The heterogeneous multiscale method (HMM) (E and Engquist, 2003; Engquist *et al.*, 2007; Abdulle *et al.*, 2012) is a widely used framework for top-down, two-way coupling methods. In HMM, the fine-scale model is reinitialized at every discrete instant of coarse-scale time and run until it has sufficiently relaxed. Then, data is extracted from the fine-scale to evolve the coarse scale for one coarse-scale time step. An extension of the HMM approach is the so-called seamless-HMM (E, Ren, and Vanden-Eijnden, 2009). The seamless-HMM avoids reinitializing of the fine-scale model at every discrete instant of coarse-scale time by using very small coarse-scale time steps. In contrast to HMM, data is exchanged in every fine-scale time step in the seamless-HMM. Hence, the two scales evolve in lock-step but use different clocks.

Li and E (2005); Li, Yang, and E (2010) developed a top-down, two-way coupling method in the framework of HMM which uses the finite volume method on the coarse scale to compute macroscopic fluxes from the fine scale model (molecular

dynamics). The fine scale is constrained by the local deformation gradient tensor, mean velocity and temperature. To improve efficiency, they use a weighted kernel function instead of simple time average in the evaluation of the microscopic data to accelerate convergence.

Ulz (2015b) also developed a top-down, two-way coupling method in the framework of HMM, which uses a mechanical coupling with a quasi-static finite element model on the coarse scale and molecular dynamics on the fine scale. To improve efficiency, the author proposed to adjust the duration for which the fine scale problem is tracked in each macroscopic iteration step. The idea is to save computational effort by tracking the fine scale only for a short, insufficient duration in the first coarse scale iterations in order to push the coarse scale solution field quickly towards the converged solution. In later iterations, the fine scale is tracked for a proper period of time in order to obtain well converged fine scale output. This method serves as a vehicle for the implementation of the efficiency improvement approach presented in Chapter 4 and is described in detail in Section 4.2. The string method was later applied to this method to explore the free energy landscape and compute minimum free energy paths by Ulz (2019). Also, a similar method in the framework of the seamless-HMM was proposed by Ulz (2015a), which uses a dynamic finite element model on the coarse scale.

Chockalingam and Wellford (2011) developed a top-down, two-way coupling method to study thermo-mechanical problems based on homogenization. In each coarse-scale Gauss point, a molecular dynamics-like problem is solved, which is restricted by the local coarse scale displacement gradient, temperature and temperature gradient to compute the atomic forces, virial stresses and atomic velocities needed to evolve the coarse scale physics. Another method with similar capabilities was proposed by Xiang *et al.* (2012).

Due to the great freedom of design offered by a one-way coupling, there exists a vast amount of top-down, one-way coupling methods. Notable contributions are, *e.g.*, by Keralavarma, Bower, and Curtin (2014), where various scales from quantum mechanics to continuum mechanics are used to predict the ductility loss in aluminium-magnesium alloys due to dynamic strain aging, or by Barton *et al.* (2011), where also a wide range of scales is used to model the material strength of tantalum and vanadium under the influence of changes in pressure, strain rate, temperature and dislocation density. Another example was given by Jahanshahi, Ahmadi, and Khoei (2020), where the authors evaluate the response of atomistic RVEs of defective nano-materials under different loading conditions in order to identify suitable strain energy functions to be used on the coarse scale. A review of top-down, one-way coupling methods used in the modeling of material failure was given, *e.g.*, by Budarapu *et al.* (2019).

4. A stochastic approximation approach to improve the convergence behavior of hierarchical atomistic-to-continuum multiscale methods

This chapter is a modified version of the peer-reviewed journal paper "A stochastic approximation approach to improve the convergence behavior of hierarchical atomistic-to-continuum multiscale models" published in the Journal of the Mechanics and Physics of Solids (Wurm and Ulz, 2016).

4.1. Introduction

In hierarchical top-down methods, the fine scale is used to supply the missing data for the coarse-scale calculations. In this data estimation-process, the fine-scale boundary conditions and constraints are dictated by the local macrostate on the coarse scale. Commonly, molecular dynamics is used as the fine-scale model, thus the missing data is computed through time averaging on some representative volume element (RVE). Herein lies one of the key challenges in hierarchical modeling. Inappropriately chosen RVEs and/or too short periods of time for data estimation lead to poor accuracy on the coarse scale. On the other hand, choosing large RVEs and sufficiently sampling the fine-scale quantities in phase space results in excessive computational cost for any practical problem. Therefore, the estimated data and hence the coarse-scale solution fields will be erroneous in practical calculations. Thus, the data estimation can be thought of as a measurement process, in which the measured value is erroneous or noise-corrupted. Naturally, one should always strive to reduce this error as far as possible.

This chapter discusses strategies for reducing the error without introducing further computational cost, by using techniques from stochastic approximation (Kushner and Yin, 2003; Spall, 2003). Stochastic approximation (SA) is generally concerned with finding roots or extrema of noise-corrupted functions and is used in different areas in science and economics. A great deal of focus is placed on machine learning algorithms

(Benaim, 1993; Cheng and Titterington, 1994; López-Rubio and Luque-Baena, 2011). But there are also fields of application in classical engineering, *e.g.*, in the optimization of shape designs (El Alem, El Hami, and Ellaia, 2011; Seyedpoor *et al.*, 2011), for estimating the thermal conductivity in boreholes (Wen-Long *et al.*, 2012) or damping approximation (Sultan, 2010). In order to improve convergence of SA iteration schemes, the two strategies "averaging of the iterates" and "averaging of the iterates and observations" are known. As their names imply, both strategies aim at effectively reducing the noise by using averaged quantities. It will be shown that hierarchical atomistic-to-continuum methods exhibit strong similarities to SA schemes, which justifies the use of those two averaging strategies to reduce the error in the coarse-scale solution fields and to improve the convergence behavior of the multiscale method.

4.2. Hierarchical multiscale method

This section introduces a prototypical hierarchical multiscale method coupling molecular dynamics and the finite element method. It will serve as a framework to test the performance of the two stochastic approximation averaging approaches. On the coarse scale of this method, a standard finite element formulation is employed and a constant uniform temperature is assumed. The fine scale is incorporated at each Gauss point of the coarse-scale domain in the shape of a MD cell. Each MD cell contains N atoms arranged in a perfect (defect-free) crystal. The MD cells are subject to periodic boundary conditions to simulate bulk material.

4.2.1. Coarse-scale model: Quasi-static finite element method

As the coarse scale model, a quasi-static finite element formulation with a hyperelastic constitutive relation (as presented in Section 2.1.4) is used, and the Newton-Raphson method is applied to solve the nonlinear equilibrium equations (see Section 2.1.5).

The Newton-Raphson iteration scheme (Eq. 2.34) can be rewritten to show the explicit dependences on the constitutive quantities (the second Piola-Kirchhoff stress tensor $\mathbf{S}$ and the Lagrangian elasticity tensor $\mathbb{C}$) as

$$\mathbf{u}^{(n+1)} = \mathbf{u}^{(n)} + \left(\mathbf{K}^{(n)}(\mathbf{S},\mathbb{C})\right)^{-1}\left(\mathbf{f}^{\text{ext}} - \mathbf{f}^{\text{int},(n)}(\mathbf{S})\right). \tag{4.1}$$

The constitutive quantities are obtained from the fine-scale model.

4.2.2. Fine-scale model: Molecular dynamics and the NFT ensemble

The fine scale employs a MD approach which enables one to apply stresses and strains onto a MD cell, while maintaining constant temperature. To this end, the three mutually orthogonal edge vectors $\mathbf{A}^k$ of the referential MD cell are defined, which transform to $\mathbf{a}^k$ due to deformation (see Fig. 4.1). The quantity $\mathbf{F}$ is introduced, which is consistent with the deformation gradient tensor from continuum mechanics. It allows a mapping of the edge vectors and atomic positions of the form

$$\mathbf{a}^k = \mathbf{F}\mathbf{A}^k, \qquad \text{and} \qquad \mathbf{r}^\alpha = \mathbf{F}\mathbf{s}^\alpha. \tag{4.2}$$

It is important to note that in this setting, the referential MD cell will preserve its shape but the atomic positions $\mathbf{s}^\alpha$ will change with $\mathbf{r}^\alpha$.

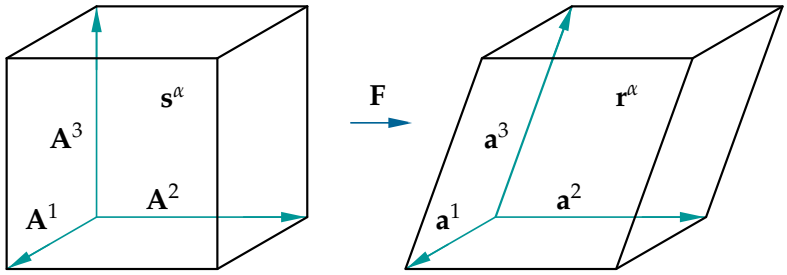

Fig. 4.1.: Mappings between referential and current MD cell with coordinates $\mathbf{s}^\alpha$ and $\mathbf{r}^\alpha$, respectively.

The following Hamiltonian is based on an extended phase space approach proposed by Ray and Rahman (1985) and is written in terms of continuum mechanics (Podio-Guidugli, 2010; Ulz, 2013; Ulz, 2015b).

$$\begin{aligned}\mathcal{H}^{\mathrm{R}} &= \mathcal{K}^{\mathrm{atoms}} + \mathcal{U}^{\mathrm{atoms}} + \mathcal{K}^{\mathrm{cell}} + \mathcal{U}^{\mathrm{cell}} + \mathcal{K}^{\mathrm{heatbath}} + \mathcal{U}^{\mathrm{heatbath}} \\ &= \mathbf{C}^{-1} : \frac{1}{2}\sum_{i=\alpha}^{N} \frac{1}{m^\alpha s^2}\mathbf{p}^\alpha \otimes \mathbf{p}^\alpha + \sum_{\alpha=1}^{N} \mathcal{U}^\alpha \\ &+ \mathbf{\Pi}^T\mathbf{\Pi} : \frac{1}{2}\mathbf{J}^{-1} + \Omega^0\mathbf{S}^{\mathrm{ext}} : \mathbf{E} + \frac{(p^s)^2}{2Q} + gk^{\mathrm{B}}T^\infty \ln(s).\end{aligned} \tag{4.3}$$

The Hamiltonian consists of kinetic terms $\mathcal{K}$ and potential terms $\mathcal{U}$. In this form, Eq. 4.3 is the Hamiltonian for the isostress-isothermal ($N\sigma T$) ensemble. However, slight modifications, allow us to obtain the Hamiltonian for the isostress-isenthalpic ($N\sigma H$) ensemble (Andersen, 1980; Parrinello and Rahman, 1981), the canonical NFT ensemble

(Nosé, 1984; Hoover, 1985; Hünenberger, 2005) or the microcanonical NFE ensemble.[1] In Eq. 4.3, $\mathbf{s}^\alpha$ and $\mathbf{p}^\alpha$ denote the atoms' coordinates in the referential MD cell and conjugate momenta, respectively. The generalized coordinates and momenta of the MD cell are $\mathbf{F}$ and $\mathbf{\Pi}$, respectively. A Nosé-Hoover thermostat (see Section 2.2.3) is included with the extra degree of freedom s, the conjugate momentum p^s and the thermal mass Q. The quantity $\mathbf{J} = \sum_{\alpha=1}^{N} m^\alpha \, \mathbf{s}^{\alpha 0} \otimes \mathbf{s}^{\alpha 0}$ is the referential inertia tensor, with $\mathbf{s}^{\alpha 0}$ being the atoms' initial positions in the referential MD cell. The volume in the referential configuration is given by Ω^0 and the externally applied stress is given by $\mathbf{S}^{\text{ext}}$, which is of the same character as the second Piola-Kirchhoff stress tensor from continuum mechanics. The associated quantity $\mathbf{E}$ corresponds to the Green-Lagrangian strain tensor and $\mathbf{C}^{-1} = \mathbf{F}^{-1}\mathbf{F}^{-T}$ is the inverse of the right Cauchy-Green deformation tensor. Eq. 4.3 further contains the Boltzmann constant k^{B} and the temperature of the heatbath T^∞. The quantity U^α denotes the potential energy of atom α.

The equations of motion can be found as (Ulz, 2015b)

$$\ddot{\mathbf{s}}^\alpha m^\alpha s^2 = -m^\alpha \left(s^2 \mathbf{C}^{-1} \dot{\mathbf{C}} + 2 s \dot{s} \right) \dot{\mathbf{s}}^\alpha - \sum_{\beta \neq \alpha}^{N} \frac{\partial_{r^{\alpha\beta}} \mathcal{U}^{\text{atoms}}}{r^{\alpha\beta}} \mathbf{s}^{\alpha\beta}, \tag{4.4}$$

$$\ddot{\mathbf{F}} \mathbf{J} = -\Omega^0 \mathbf{F} (\mathbf{S}^{\text{ext}} + \mathbf{S}^{\text{inst}}), \tag{4.5}$$

$$\ddot{s} Q = \frac{1}{s} \left(\sum_{\alpha=1}^{N} m^\alpha s^2 (\dot{\mathbf{s}}^\alpha)^T \mathbf{C} \, \dot{\mathbf{s}}^\alpha - g k^{\text{B}} T^\infty \right), \tag{4.6}$$

where $r^{\alpha\beta}$ equals the distance between atoms α and β in the current MD cell and $\mathbf{s}^{\alpha\beta} = \mathbf{s}^\alpha - \mathbf{s}^\beta$. The instantaneous microscopic stress tensor $\mathbf{S}^{\text{inst}}$ is found during derivation as

$$\mathbf{S}^{\text{inst}} = \frac{1}{\Omega^0} \left[-\mathbf{C}^{-1} \left(\sum_{\alpha=1}^{N} \frac{1}{m^\alpha s^2} \mathbf{p}^\alpha \otimes \mathbf{p}^\alpha \right) \mathbf{C}^{-1} + \frac{1}{2} \sum_{\alpha=1}^{N} \sum_{\beta \neq \alpha}^{N} \frac{\partial_{r^{\alpha\beta}} \mathcal{U}^{\text{atoms}}}{r^{\alpha\beta}} \mathbf{s}^{\alpha\beta} \otimes \mathbf{s}^{\alpha\beta} \right]. \tag{4.7}$$

The Hamiltonian in Eq. 4.3 is valid for the $N\sigma T$ ensemble and the equations of motion in Eqs. 4.4-4.6 generate microscopic configurations of this ensemble. In order to obtain the equations of motion which generate microscopic configurations of other ensembles, different constraints must be applied as shown in Tab. 4.1. In the following, the NFT ensemble will be used.

The purpose of the fine-scale model is to compute the constitutive quantities $\mathbf{S}$ and $\mathbb{C}$ for the coarse-scale computations. The microscopic counterparts to these constitutive

[1] The $N\Omega E$ and NFE ensembles are very similar. The difference is that in the $N\Omega E$ ensemble, only the volume Ω is kept constant, while in the NFE ensemble, the volume and the shape (controlled by $\mathbf{F}$) are fixed.

$N\sigma H$	$s = 1, \dot{s} = \ddot{s} = 0$		
NFT		$\mathbf{F} = \text{const.}, \dot{\mathbf{F}} = \ddot{\mathbf{F}} = \mathbf{0},$	$\mathbf{S}^{\text{ext}} = \mathbf{0}$
NFE	$s = 1, \dot{s} = \ddot{s} = 0,$	$\mathbf{F} = \text{const.}, \dot{\mathbf{F}} = \ddot{\mathbf{F}} = \mathbf{0},$	$\mathbf{S}^{\text{ext}} = \mathbf{0}$

Tab. 4.1.: Applied constraints used to simulate other ensembles than $N\sigma T$.

quantities shall be given here.

As shown in Section 2.1.4 for a hyperelastic constitutive relation, the second Piola-Kirchhoff $\mathbf{S}$ can be obtained from a given strain energy density W by derivation with respect to the Green-Lagrange strain tensor $\mathbf{E}$. An energy variable which is related the strain energy density is the Helmholtz free energy $\Psi = \Omega^0 W$. A fine-scale stress measure corresponding to the second Piola-Kirchhoff stress can hence be obtained by derivation of the Helmholtz free energy with respect to the Green-Lagrange strain tensor $\mathbf{E}$ (see, *e.g.*, Tadmor and Miller, 2011)

$$\mathbf{S} = \frac{1}{\Omega^0}\frac{\partial \Psi}{\partial \mathbf{E}} = \frac{1}{\Omega^0}\left\langle \frac{\partial \mathcal{H}^{\mathrm{R}}}{\partial \mathbf{E}} \right\rangle = \frac{1}{\Omega^0}\overline{\frac{\partial \mathcal{H}^{\mathrm{R}}}{\partial \mathbf{E}}} = \overline{\mathbf{S}^{\text{inst}}}, \tag{4.8}$$

where $\mathcal{H}^{\mathrm{R}}$ is the Hamiltonian given in Eq. 4.3 adapted for the NFT ensemble and $\mathbf{S}^{\text{inst}}$ is the instantaneous microscopic stress tensor given in Eq. 4.7. In the third equality of Eq. 4.8, the ensemble average is replaced with a time average.

The elasticity tensor is found as the second derivative of the Helmholtz free energy with respect to $\mathbf{E}$ as (Ulz, 2015b)

$$\mathbb{C} = \frac{1}{\Omega^0}\frac{\partial^2 \Psi}{\partial \mathbf{E}^2} = \frac{1}{\Omega^0}\left[\left\langle \frac{\partial^2 \mathcal{H}^{\mathrm{R}}}{\partial \mathbf{E}^2} \right\rangle - \frac{1}{k^{\mathrm{B}}T}\left(\left\langle \frac{\partial \mathcal{H}^{\mathrm{R}}}{\partial \mathbf{E}}\frac{\partial \mathcal{H}^{\mathrm{R}}}{\partial \mathbf{E}} \right\rangle - \left\langle \frac{\partial \mathcal{H}^{\mathrm{R}}}{\partial \mathbf{E}} \right\rangle \left\langle \frac{\partial \mathcal{H}^{\mathrm{R}}}{\partial \mathbf{E}} \right\rangle\right)\right]. \tag{4.9}$$

The computation of the averaged terms on the RHS of Eq. 4.9 requires a different quality of sampling to obtain sufficient accuracy. While the first term involving the second derivative is less demanding, the terms in the round brackets need a very thorough sampling in phase space. In order to ensure reasonable computational cost, these latter terms will be neglected in the method, *i.e.*,

$$\mathbb{C} \approx \frac{1}{\Omega^0}\left\langle \frac{\partial^2 \mathcal{H}^{\mathrm{R}}}{\partial \mathbf{E}^2} \right\rangle = \frac{1}{\Omega^0}\overline{\frac{\partial^2 \mathcal{H}^{\mathrm{R}}}{\partial \mathbf{E}^2}} = \overline{\mathbb{C}^{\text{inst}}}. \tag{4.10}$$

The impact of this simplification depends on the considered material and the tempera-

ture level. For the materials and temperatures used in this work (single-crystal copper at room temperature), the omitted terms only contribute $3-5\%$ to the total elasticity tensor $\mathbb{C}$ (Çain and Pettitt, 1989) and may hence be neglected. The instantaneous microscopic elasticity tensor is found as

$$\mathbb{C}^{\text{inst}} = \mathbb{C}^{\text{inst,kin}} + \mathbb{C}^{\text{inst,pot}} \tag{4.11}$$

$$C^{\text{inst,kin}}_{IJKL} = -\frac{2}{\Omega^0}\left(C^{-1}_{IK}S^{\text{inst}}_{JL} + S^{\text{inst}}_{IL}C^{-1}_{JK}\right) \tag{4.12}$$

$$\begin{aligned}\mathbb{C}^{\text{inst,pot}} = \frac{1}{\Omega^0}\Bigg[&-\frac{1}{2}\sum_{\alpha=1}^{N}\sum_{\beta\neq\alpha}^{N}\partial_{r^{\alpha\beta}}\mathcal{U}^{\text{atoms}}\frac{\mathbf{s}^{\alpha\beta}\otimes\mathbf{s}^{\alpha\beta}\otimes\mathbf{s}^{\alpha\beta}\otimes\mathbf{s}^{\alpha\beta}}{(r^{\alpha\beta})^3} \\ &+\frac{1}{2}\sum_{\alpha=1}^{N}\sum_{\beta\neq\alpha}^{N}\frac{\partial}{\partial\mathbf{E}}\left(\partial_{r^{\alpha\beta}}\mathcal{U}^{\text{atoms}}\right)\frac{\mathbf{s}^{\alpha\beta}\otimes\mathbf{s}^{\alpha\beta}}{(r^{\alpha\beta})^2}\Bigg].\end{aligned} \tag{4.13}$$

4.2.3. Details of the hierarchical multiscale method

The hierarchical multiscale method will now be described in detail. The connection between the two scales of the method is sketched in Fig. 4.2.

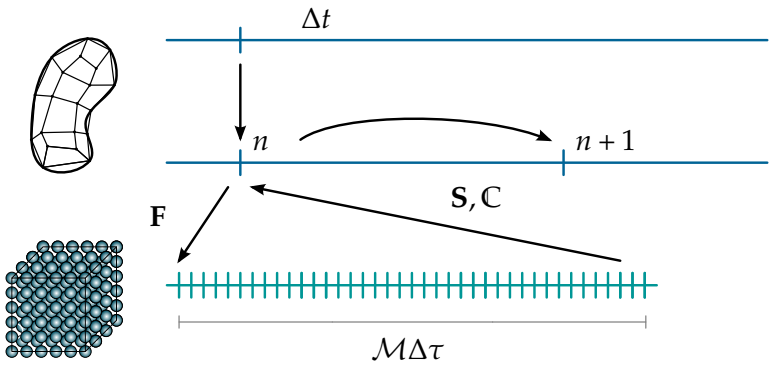

Fig. 4.2.: Information exchange between coarse and fine scale. The top two lines represent the coarse-scale time with the time step Δt and the Newton-Raphson iterations at every discrete instant of coarse-scale time t. The bottom line shows the fine-scale time with the time step $\Delta\tau$. The choice of $\Delta\tau$ must ensure that the atomic vibrations are traced appropriately.

On the coarse scale, the domain of interest is discretized using a sufficient amount of finite elements. Each finite element employs a number of Gauss points whereas each Gauss point is assigned to a MD cell on the fine scale (Fig. 4.3). Every time a new displacement field is obtained on the coarse scale, the deformation gradient in every

Gauss point is computed. Each MD cell is constrained by its associated deformation gradient tensor according to the Cauchy-Born rule (Ericksen, 2008) and the constant temperature T^{∞}, which already implies that the subsequent MD simulation is carried out under NFT conditions. During this simulation, the MD cell is tracked for $\mathcal{M}$ fine-scale time steps, and the second Piola-Kirchhoff stress tensor $\mathbf{S}$ (Eq. 4.8) and elasticity tensor $\mathbb{C}$ (Eq. 4.10), *i.e.*, the macroscopic observables of interest, are computed through time averages. In the next step, the coarse scale uses these quantities to compute a new displacement field for the next iteration in the Newton-Raphson scheme.

The MD simulation consists of two stages:

(a) Reconstruction: initialize the macroscopic constraints and let the system equilibrate (for a number of fine-scale time steps $\mathcal{M}^a$).

(b) Data estimation: follow the fine-scale model over a sufficiently large sampling time interval $[0, \tau^{\mathrm{e}}]$ and compute the macroscopic observable $\mathcal{A}$ from a time average $\overline{A(\mathbf{r}, \mathbf{p})}$ using the microscopic equivalent $A(\mathbf{r}, \mathbf{p})$ (see Section 2.2.1). This integral can be readily approximated by a sum over the fine-scale time steps $\mathcal{M}^b = \lceil \tau^e / \Delta\tau \rceil$[2]

$$\mathcal{A} = \overline{A(\mathbf{r}, \mathbf{p})} \approx \frac{1}{\tau^{\mathrm{e}}} \int_0^{\tau^{\mathrm{e}}} A(\mathbf{r}(\tau), \mathbf{p}(\tau))\, d\tau = \frac{1}{\mathcal{M}^b} \sum_{j=1}^{\mathcal{M}^b} A^j. \tag{4.14}$$

The sampling time interval $[0, \tau^{\mathrm{e}}]$ is sufficiently large if the time average converges. Specifically, the stress tensor $\mathbf{S}$ and the elasticity tensor $\mathbb{C}$ are computed from their (instantaneous) microscopic equivalents as

$$\mathbf{S} = \frac{1}{\mathcal{M}^b} \sum_{j=1}^{\mathcal{M}^b} \mathbf{S}^{\mathrm{inst},j}, \qquad \mathbb{C} = \frac{1}{\mathcal{M}^b} \sum_{j=1}^{\mathcal{M}^b} \mathbb{C}^{\mathrm{inst},j}. \tag{4.15}$$

The use of sufficiently large intervals $[0, \tau^{\mathrm{e}}]$ on the fine scale demands immense computational cost and is often not feasible in practical calculations. If the interval $[0, \tau^{\mathrm{e}}]$ is insufficient, the obtained macroscopic observables for the multiscale method are erroneous and may be written as

$$\mathbf{S} = \widetilde{\mathbf{S}} + \Delta\mathbf{S}, \qquad \mathbb{C} = \widetilde{\mathbb{C}} + \Delta\mathbb{C}, \tag{4.16}$$

where the tilde denotes the converged quantities and the Δ denotes the error (noise). Rendering the error to a minimum demands large molecular systems and/or a thorough sampling in the computation (*i.e.*, sufficiently large τ^{e} for the time average).

[2]The notation $\lceil \bullet \rceil$ denotes the ceil function $\lceil x \rceil = \min\{n \in \mathbb{Z} | n \geq x\}$.

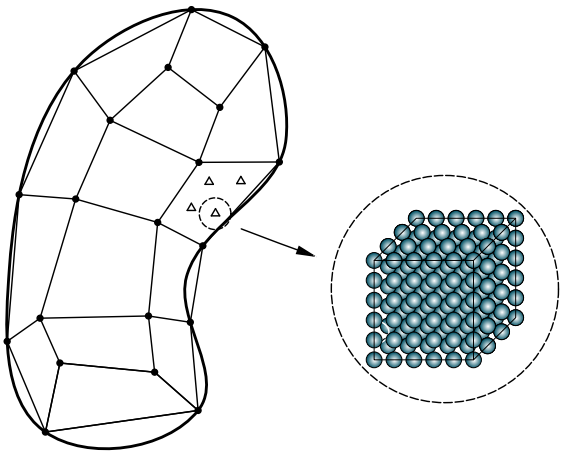

Fig. 4.3.: A MD cell is located at each Gauss point of the discretized macroscopic body.

Ulz (2015b) proposed a strategy in which the sampling time interval for data estimation is varied at each coarse-scale iteration. The sampling time interval per iteration is increased from very short intervals in the first iterations to a sufficiently long interval in the very last iteration. Thus the fine scale is sufficiently sampled only at the very last coarse-scale iteration to yield converged macroscopic observables. It is argued that a significant saving in computational cost is achieved with no accompanied loss in accuracy. However, the increase in the sampling time interval with each iteration was chosen arbitrarily rather than based on a sound mathematical treatment. This is in contrast to the present work. While the basic idea proposed by Ulz (2015b) is adopted, the increase in the sampling time interval per coarse-scale iteration is adapted to meet certain assumptions from stochastic approximation. This is further discussed in Section 4.4.

4.3. Stochastic approximation (SA)

Stochastic approximation addresses the problem of finding roots or extrema of noisy functions. In contrast to recursive methods used in classical numerical analysis (*e.g.*, the Newton-Raphson method), the function itself, $\mathbf{g}(\boldsymbol{\theta})$, is not known, but noisy measurements are available at any desired value of $\boldsymbol{\theta}$ (Kushner and Yin, 2003).

Two prototypical algorithms are presented in the literature. The Robbins-Monro algorithm for root finding problems, and the Kiefer-Wolfowitz algorithm for extremum problems.

Robbins and Monro (1951) proposed the recursive scheme

$$\boldsymbol{\theta}^{(n+1)} = \boldsymbol{\theta}^{(n)} + \varepsilon^{(n)}(\boldsymbol{\alpha} - \mathbf{Y}^{(n)}). \tag{4.17}$$

which aims at finding a root $\boldsymbol{\theta}^*$ of a function $\boldsymbol{\alpha} - \mathbf{g}(\boldsymbol{\theta}) = \mathbf{0}$, where $\mathbf{g}(\boldsymbol{\theta})$ is assumed to be nondecreasing.

Here, $\{\varepsilon^{(n)} > 0\}$ is an appropriate gain sequence which eventually goes to zero and $\mathbf{Y}^{(n)} = \mathbf{Y}(\boldsymbol{\theta}^{(n)})$ is a noisy measurement of $\mathbf{g}(\boldsymbol{\theta}^{(n)})$. As $\varepsilon^{(n)}$ goes to zero, the rate of change in $\boldsymbol{\theta}$ slows down accordingly.

The measurement $\mathbf{Y}^{(n)}$ can be written as

$$\mathbf{Y}^{(n)} = \mathbf{g}(\boldsymbol{\theta}^{(n)}) + \mathbf{e}(\boldsymbol{\theta}^{(n)}), \tag{4.18}$$

if the noise term $\mathbf{e}$ is dependent on $\boldsymbol{\theta}^{(n)}$. Variations of Eq. 4.18 are possible, *e.g.*, the noise could also be correlated to $\{\boldsymbol{\theta}^{(i)}, i \leq n\}$ (Kushner and Yin, 2003).

To get a better idea of the role of $\varepsilon^{(n)}$, Eq. 4.17 can be rewritten as

$$\begin{aligned}\boldsymbol{\theta}^{(n+1)} &= \boldsymbol{\theta}^{(n)} + \varepsilon^{(n)}(\boldsymbol{\alpha} - \mathbf{g}(\boldsymbol{\theta}^{(n)})) - \varepsilon^{(n)}\mathbf{e}(\boldsymbol{\theta}^{(n)}) \\ &= \underbrace{\boldsymbol{\theta}^{(n)} + \varepsilon^{(n)}(\boldsymbol{\alpha} - \mathbf{g}(\boldsymbol{\theta}^{(n)}))}_{\text{“deterministic” part}} + \underbrace{\varepsilon^{(n)}(\mathbf{g}(\boldsymbol{\theta}^{(n)}) - \mathbf{Y}^{(n)})}_{\text{“stochastic” part}}.\end{aligned} \tag{4.19}$$

Assuming that the function $\mathbf{g}(\boldsymbol{\theta})$ is continuous, the recursion will converge if the “stochastic” part in the above equation vanishes eventually. In principle, there are two approaches to drive the “stochastic” part to zero:

(a) The noise $\mathbf{e}$ is driven to zero in the progress of the iteration, which is of course not always possible in practice, or
(b) a properly chosen gain sequence $\{\varepsilon^{(n)}\}$ is introduced, which eventually goes to zero itself.

The choice of the gain sequence $\{\varepsilon^{(n)}\}$ greatly influences the efficiency of the scheme and is required to meet certain convergence conditions (see, *e.g.*, Kushner and Yin, 2003; Spall, 2003).

In case of an extremum problem, for example the search for a minimum $\boldsymbol{\theta}^*$ of $L(\boldsymbol{\theta})$, the corresponding set of equations reads as:

$$\mathbf{g}(\boldsymbol{\theta}) = \frac{\partial L}{\partial \boldsymbol{\theta}} = \mathbf{0}. \tag{4.20}$$

Needless to say, this requires proper conditions to ensure that a root of Eq. 4.20 is a minimum. If direct measurements of the noisy derivatives $\mathbf{g}(\boldsymbol{\theta})$ are available, the associated solution algorithms are called stochastic gradient or gradient-based methods (Spall, 2003). However, if only noisy measurements of $L(\boldsymbol{\theta})$ are available, the gradients can only be estimated, *e.g.*, via finite differences using the noisy measurements y. This method is the multivariate extension of the Kiefer-Wolfowitz algorithm (Kiefer and Wolfowitz, 1952):

$$\boldsymbol{\theta}^{(n+1)} = \boldsymbol{\theta}^{(n)} - \varepsilon^{(n)} \widehat{\mathbf{g}}^{(n)}(\boldsymbol{\theta}^{(n)}), \tag{4.21}$$

where $\{\varepsilon^{(n)}\}$ is required to meet the same convergence conditions as before, and $\widehat{\mathbf{g}}^{(n)}(\boldsymbol{\theta}^{(n)})$ is the finite difference estimate at the iterate $\boldsymbol{\theta}^{(n)}$ which is usually either approximated one-sided or two-sided. The two-sided approximation for a p-dimensional problem reads as:

$$\widehat{\mathbf{g}}^{(n)}(\boldsymbol{\theta}^{(n)}) = \begin{bmatrix} \dfrac{y(\boldsymbol{\theta}^{(n)} + c^{(n)}\boldsymbol{\xi}^1) - y(\boldsymbol{\theta}^{(n)} - c^{(n)}\boldsymbol{\xi}^1)}{2c^{(n)}} \\ \cdots \\ \dfrac{y(\boldsymbol{\theta}^{(n)} + c^{(n)}\boldsymbol{\xi}^p) - y(\boldsymbol{\theta}^{(n)} - c^{(n)}\boldsymbol{\xi}^p)}{2c^{(n)}} \end{bmatrix}. \tag{4.22}$$

In this scheme, $\{c^{(n)}\}$ denotes another gain sequence with similar conditions as $\{\varepsilon^{(n)}\}$ and additionally $\sum_{n=0}^{\infty}(\varepsilon^{(n)})^2/(c^{(n)})^2 < \infty$. The quantity $\boldsymbol{\xi}^i$ is a vector which has the value one at its i-th component and zero in all other places.

Because of the large amount of measurements needed, these finite difference approximations are becoming quite costly for high-dimensional problems. This can be tackled using the simultaneous perturbation approach introduced by Spall (1992).

Next to the two prototypical iteration schemes presented, there is a vast variety on stochastic approximation algorithms and possible choices for the gain sequences $\{\varepsilon^{(n)}\}$ and $\{c^{(n)}\}$ in the literature. In particular adaptive SA algorithms are of interest for the present work, where some knowledge of the Jacobian and/or Hessian is used in the method to improve the overall convergence behavior. An interesting algorithm of this class was proposed by Spall (2000) and may be written as

$$\boldsymbol{\theta}^{(n+1)} = \boldsymbol{\theta}^{(n)} + \varepsilon^{(n)} \left(\mathbf{U}(\boldsymbol{\theta}^{(n)}) \right)^{-1} \left(\boldsymbol{\alpha} - \mathbf{Y}^{(n)} \right), \tag{4.23}$$

which recasts the classical Robbins-Monro root finding problem. Here, $\mathbf{U}(\boldsymbol{\theta}^{(n)})$ denotes the estimate of the Jacobian matrix of $\mathbf{g}$ at $\boldsymbol{\theta}^{(n)}$, and is calculated in a separate recursive calculation using function measurements $\mathbf{Y}$ in the simultaneous perturbation approach.

4.3.1. Averaging of the iterates

Depending on the selected gain sequence $\{\varepsilon^{(n)}\}$, the sample average

$$\boldsymbol{\Theta}^{(n)} = \frac{1}{N^{\text{off}}} \sum_{i=n-N^{\text{off}}+1}^{n} \boldsymbol{\theta}^{(i)} \tag{4.24}$$

can be a better estimate of the desired solution $\boldsymbol{\theta}^*$ than $\boldsymbol{\theta}^{(n)}$. In this expression, N^{off} determines the window of averaging. This procedure is here referred to as "offline" averaging, as it does not influence the actual stochastic approximation algorithm, but rather replaces its final estimate with an average of previous estimates.

It is commonly known that if $\varepsilon^{(n)}$ approaches zero more slowly than $1/n$, averaging of the iterates may be preferable. This was originally found by Polyak and Juditsky (1992), a proof was given by Kushner and Yang (1993). One possible choice of $\varepsilon^{(n)}$ that fulfills this criterion is

$$\varepsilon^{(n)} = \frac{\kappa}{\kappa + n} \qquad \kappa > 1. \tag{4.25}$$

For further information see, *e.g.*, Kushner and Yin (2003); Spall (2003).

4.3.2. Averaging of the iterates and observations

Another way to improve the convergence behavior under certain conditions is to use the following scheme, which was originally proposed by Bather (1989)

$$\boldsymbol{\theta}^{(n+1)} = \breve{\boldsymbol{\theta}}^{(n)} + n\varepsilon^{(n)}(\boldsymbol{\alpha} - \breve{\mathbf{Y}}^{(n)}), \tag{4.26}$$

This algorithm uses averaged values of the iterates and observations in the form

$$\breve{\boldsymbol{\theta}}^{(n)} = \frac{1}{n}\sum_{i=1}^{n} \boldsymbol{\theta}^{(i)}, \qquad \breve{\mathbf{Y}}^{(n)} = \frac{1}{n}\sum_{i=1}^{n} \mathbf{Y}^{(i)}. \tag{4.27}$$

Clearly, the averaging procedure influences the stochastic approximation algorithm itself and it is therefore referred to as "online" averaging.

When comparing this algorithm with the Robbins-Monro scheme (Eq. 4.17), not only the use of averaged quantities but also the additional factor n becomes apparent. The need for this factor stems from the use of averaged quantities in the algorithm and it ensures that the convergence conditions of the gain sequence mentioned in Section 4.3 are satisfied. For further information see, *e.g.*, Schwabe (1994).

4.4. Application of SA to the hierarchical multiscale method

Upon closer examination, the Newton-Raphson iteration scheme (Eq. 4.1) shows striking similarities to the adaptive stochastic approximation scheme (Eq. 4.23), with the displacements $\mathbf{u}$ corresponding to $\boldsymbol{\theta}$. In stochastic approximation, one is interested in finding the values of $\boldsymbol{\theta} = \boldsymbol{\theta}^*$ which give a root of the function $\boldsymbol{\alpha} - \mathbf{g}(\boldsymbol{\theta}) = \mathbf{0}$, while only noise-corrupted measurements $\mathbf{Y}$ are available. The same applies to the multiscale method, where one is interested in finding a nodal displacement vector $\mathbf{u} = \mathbf{u}^*$ which fulfills $\mathbf{f}^{\text{ext}} - \mathbf{f}^{\text{int}} = \mathbf{0}$, while only noise-corrupted measurements of $\mathbf{f}^{\text{int}}(\mathbf{S})$ are available.

Furthermore, the estimate of the Jacobian matrix, $\mathbf{U}(\boldsymbol{\theta}^{(n)})$, corresponds to the stiffness matrix $\mathbf{K}$.[3]

The role of $\varepsilon^{(n)}$ in the multiscale method shall now be discussed in detail. At first, using a similar approach as in Eq. 4.19 and using Eq. 4.16, Eq. 4.1 can be rewritten as

$$\begin{aligned}
\mathbf{u}^{(n+1)} &= \mathbf{u}^{(n)} + \left[\mathbf{K}^{(n)}(\widetilde{\mathbf{S}} + \Delta\mathbf{S}, \widetilde{\mathbb{C}} + \Delta\mathbb{C})\right]^{-1} \left[\mathbf{f}^{\text{ext}} - \mathbf{f}^{\text{int},(n)}(\widetilde{\mathbf{S}} + \Delta\mathbf{S})\right] \\
&= \underbrace{\mathbf{u}^{(n)} + \left[\mathbf{K}^{(n)}(\widetilde{\mathbf{S}}, \widetilde{\mathbb{C}})\right]^{-1} \left[\mathbf{f}^{\text{ext}} - \mathbf{f}^{\text{int},(n)}(\widetilde{\mathbf{S}})\right]}_{\text{“deterministic” part}} \\
&\quad + \underbrace{\left[\mathbf{K}^{(n)}(\widetilde{\mathbf{S}}, \widetilde{\mathbb{C}})\right]^{-1} \left[-\mathbf{f}^{\text{int},(n)}(\Delta\mathbf{S})\right] + \left[\mathbf{K}^{(n)}(\Delta\mathbf{S}, \Delta\mathbb{C})\right]^{-1} \left[\mathbf{f}^{\text{ext}} - \mathbf{f}^{\text{int},(n)}(\widetilde{\mathbf{S}}) - \mathbf{f}^{\text{int},(n)}(\Delta\mathbf{S})\right]}_{\text{“stochastic” part}},
\end{aligned} \tag{4.28}$$

where the additive decompositions $\mathbf{K}^{(n)}(\widetilde{\mathbf{S}} + \Delta\mathbf{S}, \widetilde{\mathbb{C}} + \Delta\mathbb{C}) = \mathbf{K}^{(n)}(\widetilde{\mathbf{S}}, \widetilde{\mathbb{C}}) + \mathbf{K}^{(n)}(\Delta\mathbf{S}, \Delta\mathbb{C})$ and $\mathbf{f}^{\text{int},(n)}(\widetilde{\mathbf{S}} + \Delta\mathbf{S}) = \mathbf{f}^{\text{int},(n)}(\widetilde{\mathbf{S}}) + \mathbf{f}^{\text{int},(n)}(\Delta\mathbf{S})$ are used.

Clearly, the same situation as in Section 4.3 is revealed. The recursion will converge if the “stochastic” part in the above equation vanishes eventually. In Section 4.3, two possible approaches to reach this goal were presented. We refrain from the first approach, *i.e.*, introducing a gain sequence, due to concerns of the validity of such an approach in the theoretical background of the Newton-Raphson method. Furthermore, introducing a gain sequence would certainly hinder the general applicability to other hierarchical methods. Instead, the second approach is used, *i.e.*, the noise is steadily reduced over

[3] In most classical adaptive SA algorithms it is assumed that the estimate of the Jacobian matrix $\mathbf{U}(\boldsymbol{\theta}^{(n)})$ is not directly accessible, but needs to be approximated. However, in the case of the presented multiscale method, the corresponding quantity $\mathbf{K}$ is directly accessible, *i.e.*, it can be computed from directly measured quantities.

the iterations by gradually increasing the number of fine-scale time steps per iteration $\mathcal{M}^{(n)}$ for a longer sampling of the fine-scale (Fig. 4.4).

To further reduce the impact of the noise on the calculations, the SA averaging concepts (Secs. 4.3.1 and 4.3.2) are applied on the multiscale method. These averaging concepts are employed in SA, if the gain sequence $\varepsilon^{(n)}$ cannot be properly chosen. Here, we find ourselves (to some extent) in such a situation and expect an improvement in the multiscale method.

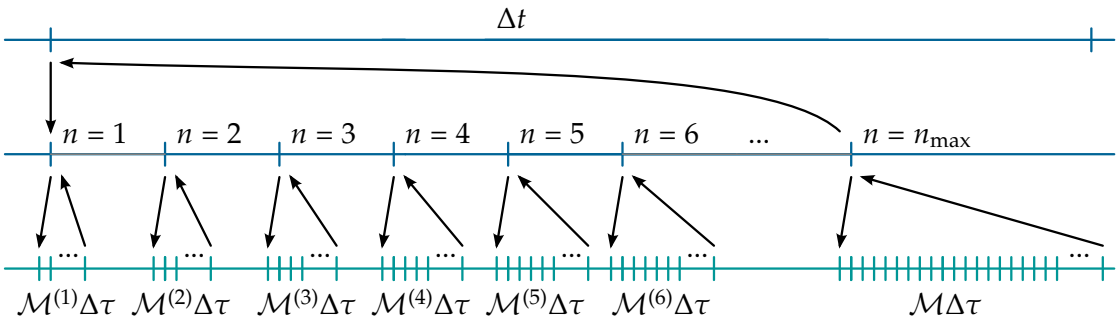

Fig. 4.4.: Coarse-scale and fine-scale time lines of the described multiscale method. The number of fine-scale time steps per iteration is increased gradually.

For reasons of consistency, the relation for $\mathcal{M}^{(n)}$ is chosen according to the gain sequence $\{\varepsilon^{(n)}\}$.

A possible choice for $\varepsilon^{(n)}$ was presented in Eq. 4.25, which is also suitable for "offline" averaging. However, a direct application of this sequence yields a very small number of fine-scale time steps and improper averaging results on the fine scale. Therefore, the following sequence in the atomistic-to-continuum setting is advocated

$$\mathcal{M}^{(n)} = \frac{\kappa + n}{\kappa}\lambda. \tag{4.29}$$

The introduction of the multiplier $\lambda > 0$ ensures a reasonable number of fine-scale time steps. This factor does not violate the criterion which led to Eq. 4.25.

To sum up, the general idea of this work is to diminish the noise in a multiscale method by the combination of two strategies adopted from SA. Firstly, a reduction of the noise over the course of the iterations is achieved by increasing the number of fine-scale time steps gradually in each iteration. Secondly, two averaging schemes ("averaging of the iterates" and "averaging of the iterates and observations") are applied to further improve the convergence behavior.

4.4.1. "Offline" averaging

Two different search paths in a two-dimensional space are shown in Fig. 4.5 as described by Spall (2003). The two-dimensional search path can be thought of as the nodal position in a two-dimensional finite element simulation. If the nodal point shows similar behavior to Fig. 4.5a, *i.e.*, it fluctuates in a small area in which we can expect the root $\boldsymbol{\theta}^*$ rather than strictly approaching this point as shown in Fig. 4.5b, "offline" averaging will potentially improve the iteration result. In fact, we will see in Section 4.5 that thermal fluctuations cause the nodal points to behave in a similar manner as shown in Fig. 4.5a. Therefore, one can expect a better estimate of the correct nodal displacement vector $\mathbf{u}^*$ when using "offline" averaging.

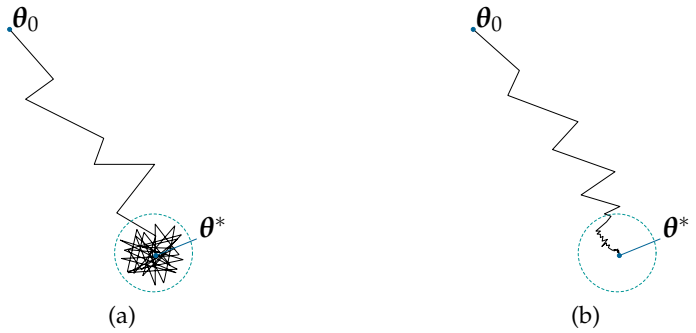

Fig. 4.5.: Two different scenarios of search paths in a two-dimensional SA problem. "Offline" averaging is expected to improve the result of the scenario in (a), but certainly will not improve the outcome of the scenario in (b). Figures taken from Spall (2003).

4.4.2. "Online" averaging

"Online" averaging was discussed in Section 4.3.2 as a second method for improving the results of SA schemes. While "offline" averaging did not influence the iteration process, "online" averaging interferes with the SA scheme as both the iterates and the observations are constantly averaged.

It was found that Bather's original algorithm (Eqs. 4.26, 4.27) does not perform well for the multiscale method and for this reason two modifications were made.

Firstly, the factor $n\varepsilon^{(n)}$ in the second term on the RHS of Eq. 4.26 is omitted. This change is mainly introduced due to the missing one-to-one equivalence of the SA algorithm with the NR iteration scheme. Since there is no gain sequence in the multiscale method (please see the discussion at the beginning of this section), there is no need to artificially introduce the factor n to satisfy the convergence criteria for the involved gain sequence.

Secondly, instead of accounting for all previous iterates and observations in the averages, only the last N^{on} are taken in the form of a constant window of averaging

$$\check{\boldsymbol{\theta}}^{(n)} = \frac{1}{N^{\text{on}}} \sum_{i=n-N^{\text{on}}+1}^{n} \boldsymbol{\theta}^{(i)}, \qquad \check{\mathbf{Y}}^{(n)} = \frac{1}{N^{\text{on}}} \sum_{i=n-N^{\text{on}}+1}^{n} \mathbf{Y}^{(i)}. \tag{4.30}$$

This change is introduced to speed up the algorithm and to prevent the first few (usually more erroneous) iterates and observations from influencing the later iterations.

The application of this algorithm changes the NR iteration scheme in Eq. 4.1 to

$$\mathbf{u}^{(n+1)} = \check{\mathbf{u}}^{(n)} + \left[\mathbf{K}^{(n)}(\check{\mathbf{S}}, \check{\mathbb{C}})\right]^{-1} \left[\mathbf{f}^{\text{ext}} - \mathbf{f}^{\text{int},(n)}(\check{\mathbf{S}})\right], \tag{4.31}$$

using averages of N^{on} preceding NR iterations

$$\check{\mathbf{u}}^{(n)} = \frac{1}{N^{\text{on}}} \sum_{i=n-N^{\text{on}}+1}^{n} \mathbf{u}^{(i)}, \qquad \check{\mathbf{S}} = \frac{1}{N^{\text{on}}} \sum_{i=n-N^{\text{on}}+1}^{n} \mathbf{S}^{(i)}, \qquad \check{\mathbb{C}} = \frac{1}{N^{\text{on}}} \sum_{i=n-N^{\text{on}}+1}^{n} \mathbb{C}^{(i)}. \tag{4.32}$$

4.4.3. Stress distribution

It is important to note that an accurate displacement field does not necessarily result in an accurate stress distribution. A reasoning for this behavior is provided below.

In Section 4.2.3, it was shown that the stresses are computed on the fine scale by an averaging procedure. The obtained stresses in a Gauss point can be written as

$$\mathbf{S}(\mathbf{u}) = \widetilde{\mathbf{S}}(\mathbf{u}) + \Delta\mathbf{S}(\mathbf{u}), \tag{4.33}$$

where $\widetilde{\mathbf{S}}(\mathbf{u})$ again is the correct stress response (converged average) for some nodal displacement vector $\mathbf{u}$ and $\Delta\mathbf{S}$ is the error. Even if the correct nodal displacement vector $\mathbf{u}^*$ were found, the stress response obtained would still be erroneous, *i.e.*,

$$\mathbf{S}(\mathbf{u}^*) = \widetilde{\mathbf{S}}(\mathbf{u}^*) + \Delta\mathbf{S}(\mathbf{u}^*). \tag{4.34}$$

As a result, insufficient fine-scale sampling will still render the stress distribution erroneous, even if "offline" or "online" averaging yield displacements arbitrarily close to the desired displacement field.

The stress distribution may be improved using an additional "offline" averaging of the stresses. This idea is along the same lines of averaging the displacements and will not cause any additional computational cost.

4.5. Numerical examples

To show the effectiveness of the proposed strategies, three numerical examples are studied. An elongated plate under uniaxial tension serves as an introductory example. In the second example, a plate with a circular notch under uniaxial tension is investigated. Finally, the third example is concerned with a plate with a single crack which is also subject to uniaxial tension. In the examples, the evolution of the displacements and stresses over the NR iterations at characteristic points in the macroscopic domain will be investigated and give an insight in the averaging behavior. Furthermore, the stress distributions of the numerical simulation will be compared with analytical solutions.

All three examples are studied under conditions of plane strain at 300 K. A copper single crystal denotes the modeled material. The domain will be discretized by the finite element method with either linear quadrilaterals or triangles using the Newton-Raphson method as the coarse-scale solver.

The Gauss quadrature rule is applied, using 2×2 quadrature points for the linear quadrilaterals and one quadrature point for the linear triangle elements. The recovery of the nodal stresses is achieved by extrapolating the stresses from the quadrature points to the nodes and subsequent averaging.

The Gear sixth-order predictor-corrector scheme (see Section 2.2.4) gives the time integration algorithm on the fine scale in an MD program implemented in Fortran. The initial cubic MD cell at each coarse-scale Gauss point contains 500 atoms in a face-centered cubic (fcc) lattice and has periodic boundary conditions. Furthermore, the simulation box is oriented along the crystallographic axes with the x-axis coinciding with [100]. An EAM potential gives the atomic interaction according to the presented functions and parameters by Zhou *et al.* (2001); a cut-off radius of 2.5 times the unit cell length is taken. The fine-scale time step is set to 0.375 fs.

In the light of the preceding section, the simulation scenarios are summarized in Tab. 4.2.

In all three examples, the number of fine-scale time steps per iteration is increased according to Eq. 4.29 using $\kappa = 1.1$ and $\lambda = 50$. These values ensure a computationally managable amount of total fine-scale time steps for the problems presented below. The parameter for the window of averaging in case *sa2* (Eq. 4.32) is chosen to be $N^{\text{on}} = 10$ in all three examples. A sensitivity analysis yielded that the results are rather insensitive in regards to the choice of these three parameters, although a detailed analysis was not performed and may be a topic for future research.

std	NR iteration scheme according to Eq. 4.1 standard case, no averaging procedures from SA are applied
sa1	NR iteration scheme according to Eq. 4.1 & **"offline"** averaging of the **displacements** (Section 4.4.1) & **"offline"** averaging of the **stresses** (Section 4.4.3)
sa2	NR iteration scheme according to Eq. 4.31, which involves **"online"** averaging of the **displacements** and **stresses** (Section 4.4.2) & **"offline"** averaging of the **displacements** (Section 4.4.1) & **"offline"** averaging of the **stresses** (Section 4.4.3)

Tab. 4.2.: Compared methods. For the sake of brevity, the abbreviations in the first column are introduced.

4.5.1. Stretched plate

A plate with dimensions $200 \times 100 \times 1\,\text{mm}$ is uniaxially loaded with $p = 1\,\text{GPa}$. The plate is discretized by two standard 4-node quadrilaterals and is subject to Dirichlet boundary conditions as shown in Fig. 4.6.

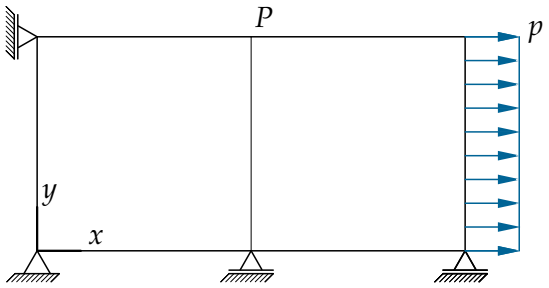

Fig. 4.6.: Geometry and boundary conditions of the stretched plate.

The load is applied in a single coarse-scale time step in which $n^{\max} = 150$ Newton-Raphson iterations are performed. In order to gain insight into the averaging behavior of the proposed strategies, the displacements and stresses of a characteristic node P in the macroscopic domain are investigated.

In contrast to the following two examples, the simplicity of this example allows for a thorough sampling of the fine-scale quantities in a reasonable computational time. A reference case can therefore be introduced, which uses only well converged averaged quantities on the fine scale for computation. The reference case shows 15 Newton-Raphson iterations with 1.4 million fine-scale time steps each for sampling.

Fig. 4.7 shows the displacement of node P over the total number of fine-scale time steps for the cases *std*, *sa1*, *sa2* and the reference case. The noise clearly manifests in the

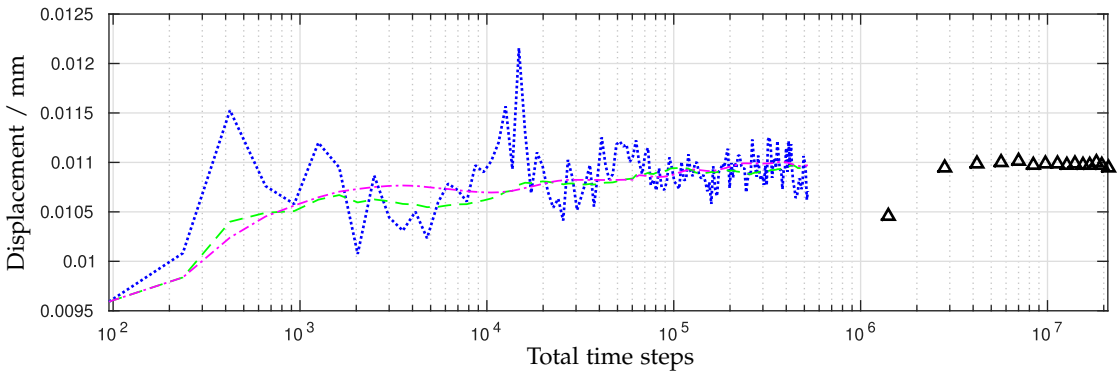

Fig. 4.7.: Displacement of node P for the stretched plate. The dotted line shows the *std* case, the dashed and dot-dashed line represent the cases *sa1* and *sa2*, respectively. The triangles show the results for the reference case, where only well converged averaged quantities are used. For the *std* case, the displacement is simply $u^{(n)}$ of the corresponding scheme, whereas for cases *sa1* and *sa2* it is the average over N^{off} previous iterations $\frac{1}{N^{\text{off}}} \sum_{i=n-N^{\text{off}}+1}^{n} u^{(i)}$ where $N^{\text{off}} = 50$.

fluctuations of the displacement for the *std* case. Both averaging strategies reduce the impact of this noise on the resulting displacement and smoothen the curve.

One can also see that the reference case yields very similar displacements, but of course at a much higher computational expense (note that the total number of fine-scale time steps is plotted on a logarithmic scale).

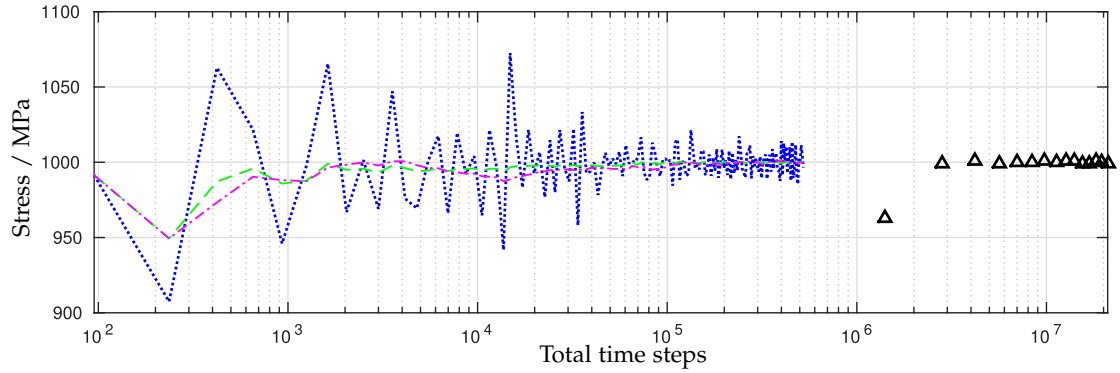

Fig. 4.8.: Normal stress in x-direction at node P for the stretched plate. The dotted line shows the *std* case, the dashed and dot-dashed line represent the cases *sa1* and *sa2*, respectively. The triangles show the results for the reference case, where only well converged averaged quantities are used. For the *std* case, the stress is simply $\sigma_{xx}^{(n)}$, whereas for *sa1* and *sa2* it is the average over N^{off} previous iterations $\frac{1}{N^{\text{off}}} \sum_{i=n-N^{\text{off}}+1}^{n} \sigma_{xx}^{(i)}$ where $N^{\text{off}} = 50$.

The same applies to the normal stress in x-direction at node P shown in Fig. 4.8. The benefits of the two averaging strategies become even clearer in an alternative

representation shown in Fig. 4.9, where the percentual error of the stress for the cases *std*, *sa1*, *sa2* and the reference case is shown.

It can be seen that both averaging strategies significantly reduce the error in comparison to the *std* case and result in errors $< 0.1\%$ after a total of about $400,000$ fine-scale time steps. The reference case, which uses well converged averaged quantities, needs at least 4.2 million fine-scale time steps to yield an error $< 0.1\%$. In this example, both averaging schemes provide a saving of about 90% of computational effort in comparison to the well converged reference case.

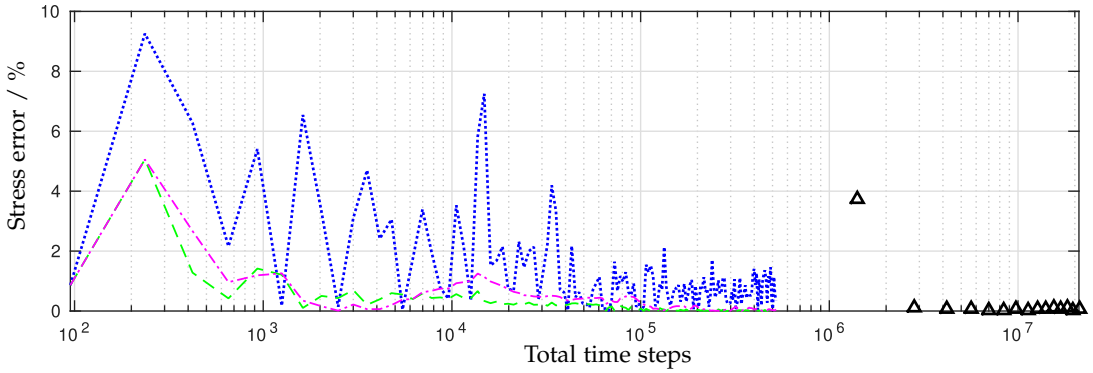

Fig. 4.9.: Percentual error of normal stress in x-direction at node P for the stretched plate. The target stress value is 1 GPa. The dotted line shows the *std* case, the dashed and dot-dashed line represent the cases *sa1* and *sa2*, respectively. The triangles show the results for the reference case, where only well converged averaged quantities are used. For the *std* case, the stress used in the evaluation is simply $\sigma_{xx}^{(n)}$, whereas for *sa1* and *sa2* it is the average over N^{off} previous iterations $\frac{1}{N^{\text{off}}} \sum_{i=n-N^{\text{off}}+1}^{n} \sigma_{xx}^{(i)}$ where $N^{\text{off}} = 50$.

4.5.2. Plate with a circular notch under uniaxial tension

A plate with dimensions $723 \times 723 \times 1$ mm and a centrical circular notch of radius $a = 21.69$ mm is considered as shown in Fig. 4.10a. The plate is loaded in y-direction with $p = 667$ MPa. Due to the symmetry of the problem, only a quarter is investigated with accordingly chosen boundary conditions to avoid unnecessary computational cost (Fig. 4.10b). As the stress gradients in close distance to the notch are assumed to be much higher than those on the outer edges, the element sizing is adapted accordingly, resulting in a total amount of 546 standard 3-node triangle elements (see Fig. 4.10c). Again, the load is applied in a single coarse-scale time step, although in this example $n^{\max} = 70$.

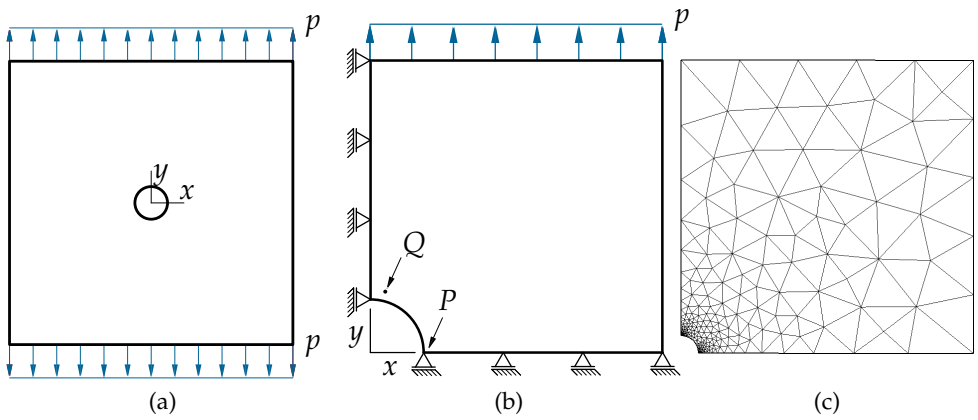

Fig. 4.10.: (a) Plate with a circular notch under uniaxial tension. (b) Modeled system and boundary conditions. (c) FEM mesh.

Comparison of the averaging behavior

In Section 4.4.1 it was mentioned that "offline" averaging is expected to improve the final estimate of the displacement field if the nodal points' motion over the iterations shows similar behavior to Fig. 4.5a. To show that this is the case, a characteristic node Q (see Fig. 4.10b), located at $x = 6.804\,\text{mm}$ and $y = 24.098\,\text{mm}$ is selected. The node moves along a two-dimensional displacement path as shown in Fig. 4.11. A comparison with Fig. 4.5a shows that the assumptions made in Section 4.4.1 apply and, hence, "offline" averaging can be expected to improve the displacement field.

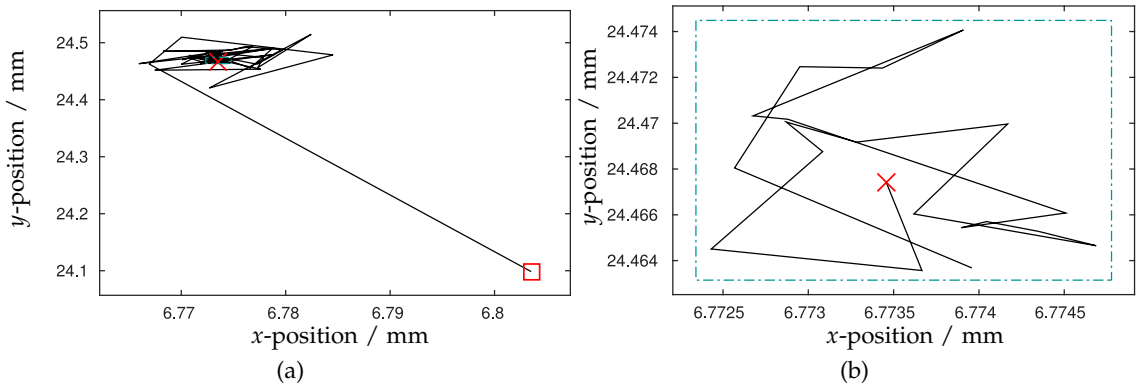

Fig. 4.11.: (a) Position of node Q over the iterations. The initial and final positions of Q are given with (□) and (×), respectively. (b) An enlarged view of the area that contains the last 20 iterations.

A node P located directly at the notch, at $x = 21.69\,\text{mm}$ and $y = 0\,\text{mm}$, is investigated

next. The evolution of the displacement in x-direction and the stress in y-direction at this node over the NR iterations is shown in Figs. 4.12 and 4.13, respectively. The proposed averaging strategies clearly smoothen the curves and show faster convergence. It can be seen that both strategies give a good estimate of the final displacement and s

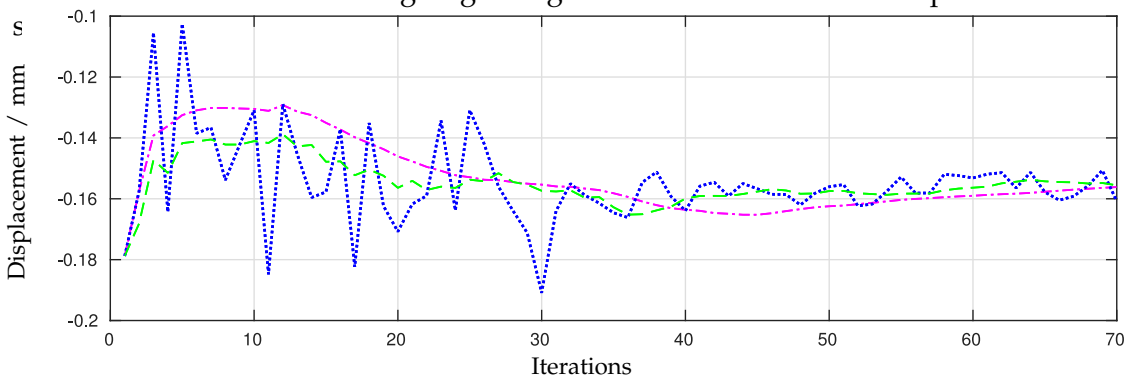

Fig. 4.12.: Displacement of node P over the iterations. The dotted, dashed and dot-dashed lines show the results for the cases *std*, *sa1* and *sa2*, respectively. For the *std* case, the displacement is simply $u^{(n)}$ of the corresponding scheme, whereas for cases *sa1* and *sa2* it is the average over N^{off} previous iterations $\frac{1}{N^{\text{off}}} \sum_{i=n-N^{\text{off}}+1}^{n} u^{(i)}$ where $N^{\text{off}} = 10$.

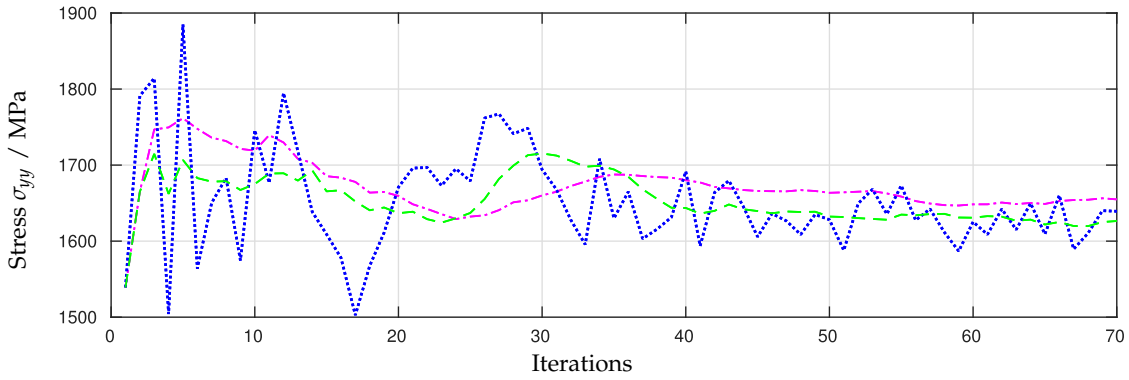

Fig. 4.13.: Normal stress at node P over the iterations. The dotted, dashed and dot-dashed lines show the results for the cases *std*, *sa1* and *sa2*, respectively. For the *std* case, the stress is simply $\sigma_{yy}^{(n)}$, whereas for *sa1* and *sa2* it is the average over N^{off} previous iterations $\frac{1}{N^{\text{off}}} \sum_{i=n-N^{\text{off}}+1}^{n} \sigma_{yy}^{(i)}$ where $N^{\text{off}} = 10$.

Comparison of the stress distributions

The final estimates of the stress distributions (*i.e.*, at $n = n^{\max}$) for the cases *std*, *sa1* and *sa2* will now be compared with an analytical solution. For this purpose, the normal stresses $\sigma_{xx}^{(n^{\max})}$ and $\sigma_{yy}^{(n^{\max})}$ are normalized by p and plotted along the x- and y-axis in Figs. 4.14 to 4.17. The analytical solution as given by Lekhnitskii (1968) (elastic constants taken from Lazarus (1949) for copper) is presented by a solid line in all of these figures.

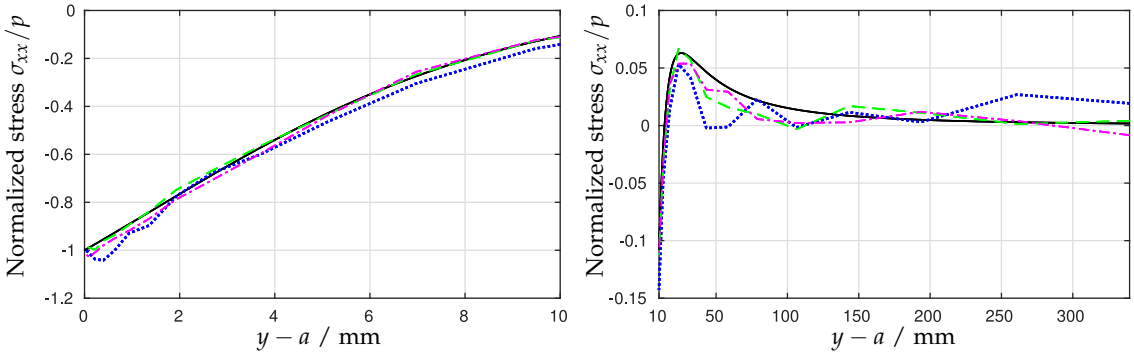

Fig. 4.14.: Normalized normal stress along the y-axis. The dotted, dashed and dot-dashed lines show the results for the cases *std*, *sa1* and *sa2*, respectively. The analytical solution is given as a solid line. For the *std* case, the normalized stress is simply $\sigma_{xx}^{(n^{\max})}/p$, whereas for *sa1* and *sa2* it is the normalized average over N^{off} previous iterations $\frac{1}{pN^{\text{off}}} \sum_{i=n^{\max}-N^{\text{off}}+1}^{n^{\max}} \sigma_{xx}^{(i)}$ where $N^{\text{off}} = 10$.

The stress distributions show a good overall agreement with the analytical solution. This implies that the used multiscale method combined with the proposed SA averaging schemes is appropriate for this example. For the majority of the displayed results, the curves obtained for the averaging strategies *sa1* and *sa2* show less deviation from the analytical solution than the *std* case.

To quantify these results, the mean absolute error (MAE)

$$\text{MAE}_{ij} = \frac{1}{N^{\text{nodes}}} \sum_{I=1}^{N^{\text{nodes}}} \left| \tilde{\sigma}_{ij}^{(n^{\max}),I} - \sigma_{ij}^{*I} \right|, \tag{4.35}$$

is introduced, which compares the absolute deviation of the stress component $\tilde{\sigma}_{ij}^{(n_{\max})}$ obtained by *std*, *sa1* or *sa2* with the analytical solution. The results in Tab. 4.3 show that both averaging schemes are able to reduce the MAE significantly, by up to about 20%.

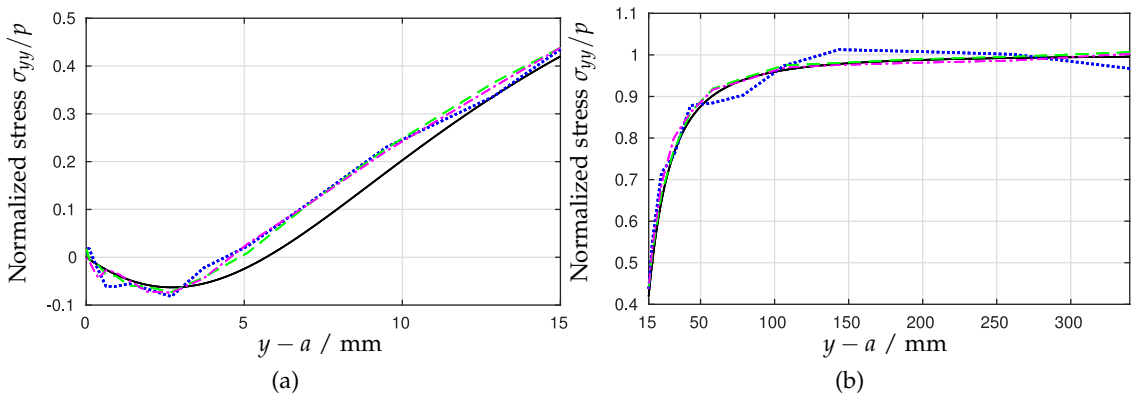

Fig. 4.15.: Normalized normal stress along the y-axis. The dotted, dashed and dot-dashed lines show the results for the cases *std*, *sa1* and *sa2*, respectively. The analytical solution is given as a solid line. For the *std* case, the normalized stress is simply $\sigma_{yy}^{(n^{\max})}/p$, whereas for *sa1* and *sa2* it is the average over N^{off} previous iterations $\frac{1}{pN^{\text{off}}}\sum_{i=n^{\max}-N^{\text{off}}+1}^{n^{\max}}\sigma_{yy}^{(i)}$ where $N^{\text{off}} = 10$.

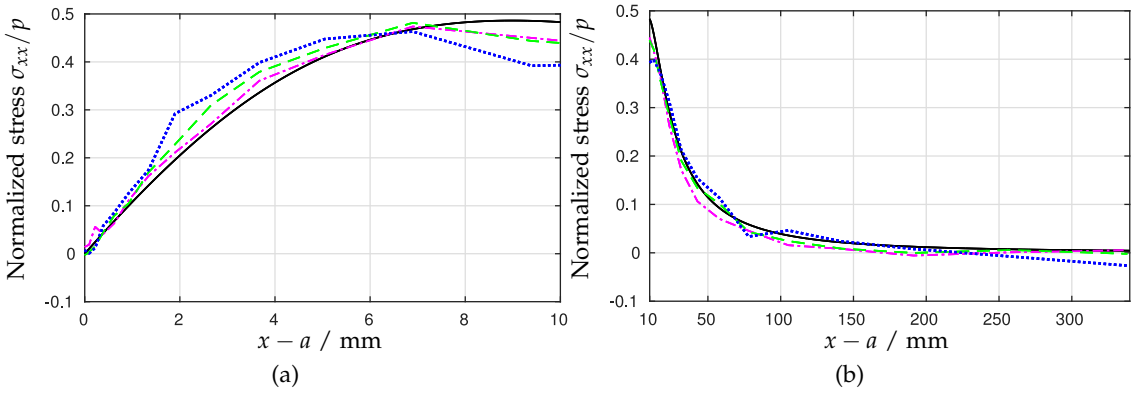

Fig. 4.16.: Normalized normal stress along the x-axis. The dotted, dashed and dot-dashed lines show the results for the cases *std*, *sa1* and *sa2*, respectively. The analytical solution is given as a solid line. For the *std* case, the normalized stress is simply $\sigma_{xx}^{(n^{\max})}/p$, whereas for *sa1* and *sa2* it is the average over N^{off} previous iterations $\frac{1}{pN^{\text{off}}}\sum_{i=n^{\max}-N^{\text{off}}+1}^{n^{\max}}\sigma_{xx}^{(i)}$ where $N^{\text{off}} = 10$.

Figs. 4.12 and 4.13 showed that both averaging strategies yield good estimates of the final displacements and stresses at early stages of the simulation. To further investigate this behavior, the calculations have been repeated for $n_{\max} = 25$. For the sake of brevity, only the results for the MAE will be given here (see Tab. 4.4). It is evident that both averaging strategies yield even greater relative reduction of the MAE in comparison to the calculations for $n^{max} = 70$ (Tab. 4.3), reducing the error by up to 50%. Furthermore,

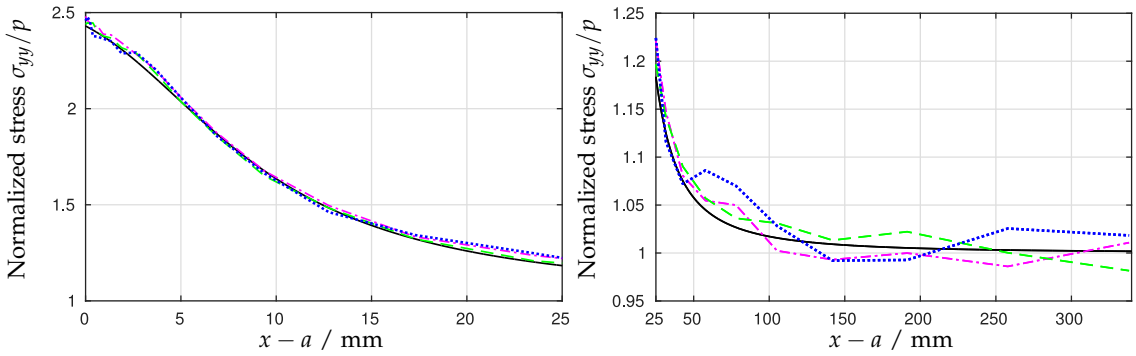

Fig. 4.17.: Normalized normal stress along the x-axis. The dotted, dashed and dot-dashed lines show the results for the cases *std*, *sa1* and *sa2*, respectively. The analytical solution is given as a solid line. For the *std* case, the normalized stress is simply $\sigma_{yy}^{(n^{\max})}/p$, whereas for *sa1* and *sa2* it is the average over N^{off} previous iterations $\frac{1}{pN^{\text{off}}}\sum_{i=n^{\max}-N^{\text{off}}+1}^{n^{\max}}\sigma_{yy}^{(i)}$ where $N^{\text{off}} = 10$.

	MAE_{xx}	$\pm\%$	MAE_{yy}	$\pm\%$	MAE_{xy}	$\pm\%$
std	29.15	0	31.90	0	15.79	0
sa1	21.50	-26.21	28.23	-11.48	12.05	-23.67
sa2	23.25	-20.24	30.06	-5.78	12.60	-20.22

Tab. 4.3.: Comparison of the MAE (in MPa) of the proposed strategies for the plate with a circular notch for $n^{\max} = 70$ iterations.

	MAE_{xx}	$\pm\%$	MAE_{yy}	$\pm\%$	MAE_{xy}	$\pm\%$
std	52.27	0	56.51	0	24.19	0
sa1	22.17	-57.58	30.04	-46.84	11.92	-50.73
sa2	24.30	-53.51	30.31	-46.37	13.70	-43.36

Tab. 4.4.: Comparison of the MAE (in MPa) of the proposed strategies for the plate with a circular notch for $n^{\max} = 25$ iterations.

at $n^{\max} = 25$, both averaging strategies yield smaller MAEs than the *std* case after $n^{\max} = 70$ iterations.

4.5.3. Plate with a crack under uniaxial tension

A crack of length $2a = 43.38\,\text{mm}$ is placed along the x-axis of a plate with dimensions $723 \times 723 \times 1\,\text{mm}$ (Fig. 4.18a). The plate is loaded in y-direction with $p = 667\,\text{MPa}$ and only a quarter of the system is investigated as shown in Fig. 4.18b. The mesh has a total of 573 3-node triangle elements and is chosen to be sufficiently fine around the crack tip (see Fig. 4.18c). The load is applied in a single coarse-scale time step with $n^{\max} = 70$ iterations.

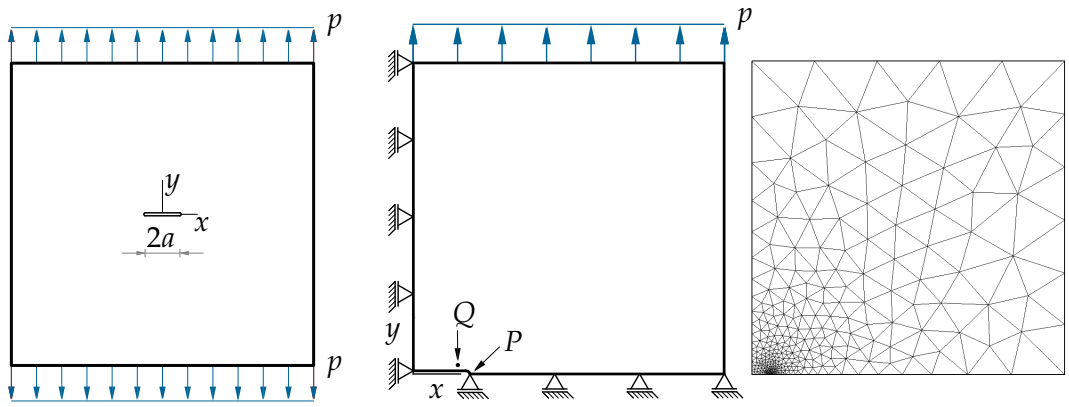

Fig. 4.18.: (a) Plate with a crack under uniaxial tension. (b) Modeled system and boundary conditions. (c) FEM mesh.

Comparison of the averaging behavior

Two characteristic nodes P and Q are selected and displayed in Fig. 4.18b. Node P is located at the crack tip, $x = 21.69\,\text{mm}$ and $y = 0\,\text{mm}$, and node Q at $x = 17.144\,\text{mm}$ and $y = 3.467\,\text{mm}$ in the undeformed configuration.

The search path of node Q is shown in Fig. 4.19. Clearly, node Q does not strictly approach its final destination but rather fluctuates in a limited area. The considerations made in Section 4.4.1 apply and therefore justify the use of "offline" averaging.

The evolution of the displacement in x-direction and the stress in y-direction of node P over the NR iterations is shown in Figs. 4.12 and 4.13, respectively. Once again, the strategies *sa1* and *sa2* smoothen the curves significantly, and good estimates of the final displacement and stress are obtained (at about 30 NR iterations).

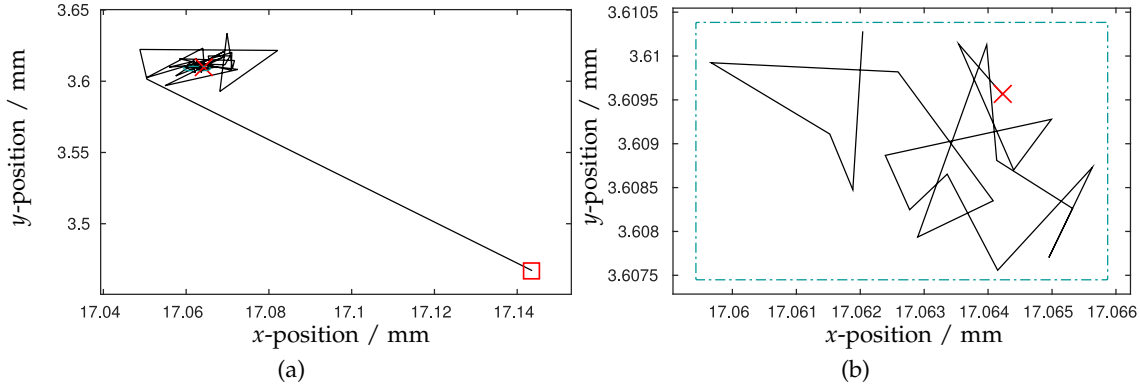

Fig. 4.19.: (a) Position of node Q over the iterations. The initial and final positions of Q are given with (□) and (×), respectively. (b) An enlarged view of the area that contains the last 20 iterations.

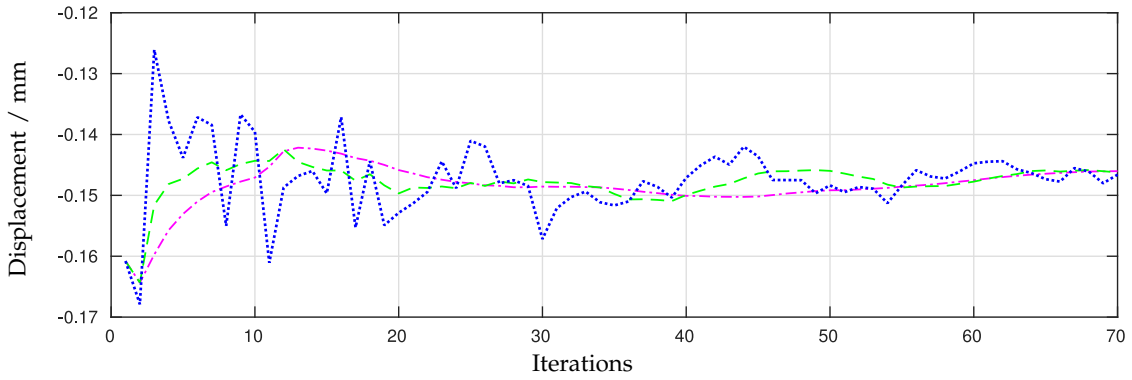

Fig. 4.20.: Displacement of node P over the iterations. The dotted, dashed and dot-dashed lines show the results for the cases *std*, *sa1* and *sa2*, respectively. For the *std* case, the displacement is simply $u^{(n)}$ of the corresponding scheme, whereas for cases *sa1* and *sa2* it is the average over N^{off} previous iterations $\frac{1}{N^{\text{off}}} \sum_{i=n-N^{\text{off}}+1}^{n} u^{(i)}$ where $N^{\text{off}} = 10$.

Comparison of the stress distributions

The final estimates of the stress distributions (*i.e.*, at $n = n^{\max}$) for the cases *std*, *sa1* and *sa2* will now again be compared to the analytical solution. The normal stresses $\sigma_{xx}^{(n^{\max})}$ and $\sigma_{yy}^{(n^{\max})}$ normalized by p along the x-axis are plotted in Figs. 4.22 and 4.23. The analytical solution is again taken from Lekhnitskii (1968) (elastic constants from Lazarus (1949) for copper) and given by a solid line in both figures.

Similar to the last example, the stresses obtained using the averaging strategies *sa1* and *sa2* show less deviation from the analytical solution than the *std* case. In Tab. 4.5 the MAE (Eq. 4.35) is used once more to verify this observation for the entire macroscopic

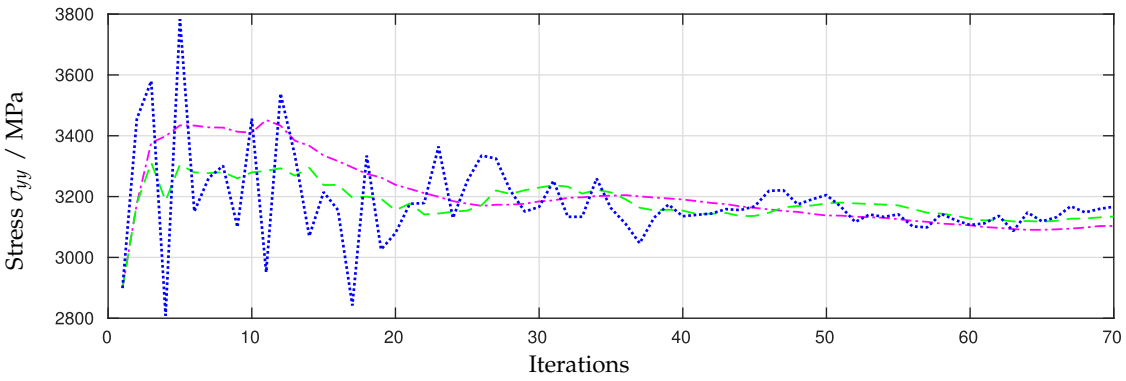

Fig. 4.21.: Normal stress at node P over the iterations. The dotted, dashed and dot-dashed lines show the results for the cases *std*, *sa1* and *sa2*, respectively. For the *std* case, the stress is simply σ^n_{yy}, whereas for *sa1* and *sa2* it is the average over N^{off} previous iterations $\frac{1}{N^{\text{off}}} \sum_{i=n-N^{\text{off}}+1}^{n} \sigma^i_{yy}$ where $N^{\text{off}} = 10$.

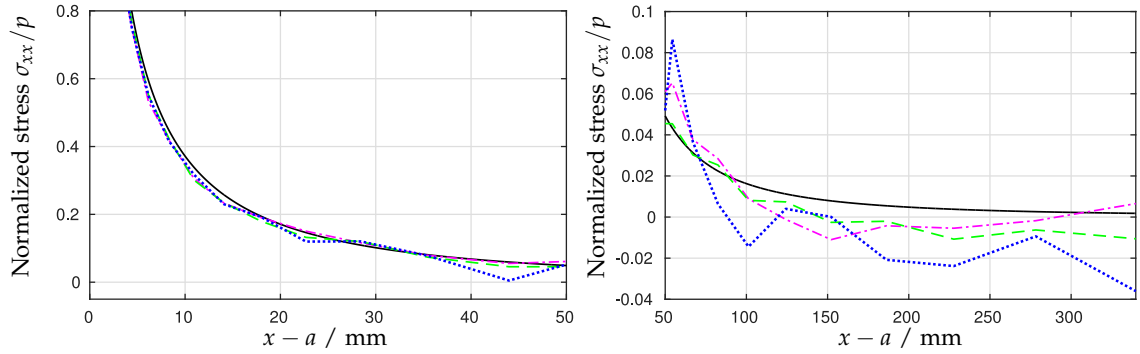

Fig. 4.22.: Normalized normal stress along the x-axis. The dotted, dashed and dot-dashed lines show the results for the cases *std*, *sa1* and *sa2*, respectively. The analytical solution is given as a solid line. For the *std* case, the normalized stress is simply $\sigma^{(n^{\max})}_{xx}/p$, whereas for *sa1* and *sa2* it is the average over N^{off} previous iterations $\frac{1}{pN^{\text{off}}} \sum_{i=n^{\max}-N^{\text{off}}+1}^{(n^{\max})} \sigma^{(i)}_{xx}$ where $N^{\text{off}} = 10$.

region[4]. The results show similar behavior to the last example, both averaging strategies can reduce the MAE by up to about 15%.

Similar to the last example, the calculations have been repeated for $n^{\max} = 25$. The results for the MAE are shown in Tab. 4.6.

[4]The analytical solution shows a stress singularity at the crack tip. Therefore, the vicinity of the crack tip (a circle with radius 1 mm) is excluded from the calculations for the MAE in Tables 4.5 and 4.6.

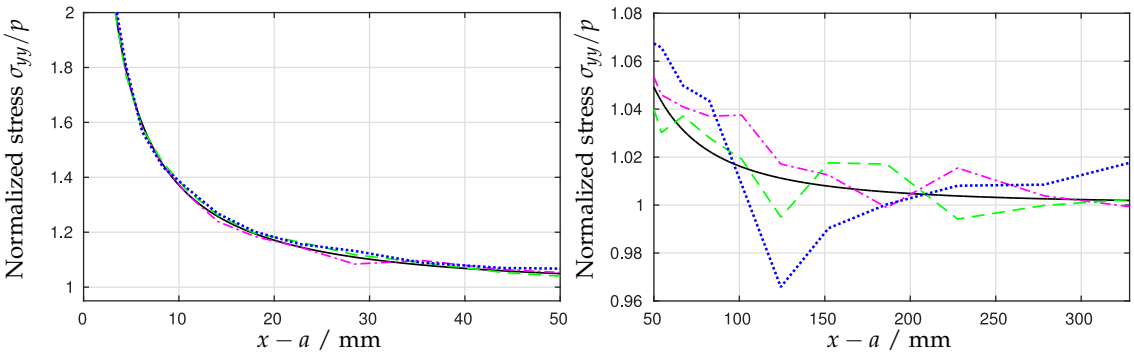

Fig. 4.23.: Normalized normal stress along the x-axis. The dotted, dashed and dot-dashed lines show the results for the cases *std*, *sa1* and *sa2*, respectively. The analytical solution is given as a solid line. For the *std* case, the normalized stress is simply $\sigma_{yy}^{(n^{\max})}/p$, whereas for *sa1* and *sa2* it is the average over N^{off} previous iterations $\frac{1}{pN^{\text{off}}}\sum_{i=n^{\max}-N^{\text{off}}+1}^{(n^{\max})}\sigma_{yy}^{(i)}$ where $N^{\text{off}} = 10$.

	MAE $_{xx}$	±%	MAE $_{yy}$	±%	MAE $_{xy}$	±%
std	21.65	0	20.25	0	18.47	0
sa1	18.31	-15.45	17.71	-14.01	15.50	-16.05
sa2	18.63	-13.95	17.32	-14.48	15.54	-15.84

Tab. 4.5.: Comparison of the MAE (in MPa) of the proposed strategies for the plate with a single crack for $n_{\max} = 70$ iterations.

	MAE $_{xx}$	±%	MAE $_{yy}$	±%	MAE $_{xy}$	±%
std	45.94	0	30.18	0	20.75	0
sa1	17.96	-60.90	16.96	-43.79	14.69	-29.22
sa2	21.12	-54.03	19.52	-35.30	14.78	-28.80

Tab. 4.6.: Comparison of the MAE (in MPa) of the proposed strategies for the plate with a single crack for $n^{\max} = 25$ iterations.

Just like in the preceding example, both averaging strategies result in greater relative MAE reduction in comparison to the calculation for $n^{\max} = 70$ iterations (Tab. 4.6) and also yield smaller MAEs at $n^{\max} = 25$ than the *std* case after $n^{\max} = 70$ iterations.

5. Demand-based coupling of the scales in concurrent atomistic-to-continuum methods at finite temperature

This chapter is a modified version of the peer-reviewed journal paper "Demand-based coupling of the scales in concurrent atomistic-to-continuum models at finite temperature" published in the Journal of the Mechanics and Physics of Solids (Wurm and Ulz, 2020).

5.1. Introduction

In the finite temperature versions the CADD method (and other concurrent methods), the coarse and fine scale are coupled at fixed intervals of time, *i.e.*, an information transfer between the scales occurs in every or in every few fine-scale time steps. With a focus on the continuum, this means that its solution fields are computed at fixed intervals of time. However, in times when there is negligible deformation at the spatial coupling interface and when the external (non-interfacial) boundary conditions on the continuum do not change, these computations are unnecessary. During these times, solving the continuum only causes the coupling interface to fluctuate around its equilibrium position and thereby conveys (possibly unwanted) thermal energy into the continuum. Yet, there is no qualitative change in the continuum solution fields - the numerical effort on the continuum computation is in vain. The transition from coupling the scales in such a fixed interval fashion towards a coupling which is based on current demand promises to yield substantial computational savings, as the continuum computations may be skipped in large portions of the simulation time.

To achieve such a demand-based coupling, the use of an algorithm which decides if the coupling is necessary, is proposed. The algorithm judges the state of deformation close to the spatial coupling interface by monitoring the relative motion between a band of atoms and the interface. If the algorithm detects non-negligible deformation, *i.e.*, deformation that is larger than some known equilibrium limit, the continuum solution

is computed ("the continuum is activated"). Otherwise, the continuum computations are skipped to save computational time. To this end, the algorithm requires knowledge of the deformation at the interface, *i.e.*, the mechanical component of the relative atomic motion between the band and the interface. Besides the mechanical component of interest, the motion also consists of a thermal component which manifests itself in random thermal fluctuations. These thermal fluctuations complicate the determination of the state of deformation and a clear separation of the mechanical and thermal component is not feasible. However, it is assumed that the mechanical component is of lower frequency than large parts of the thermal component, allowing for an approximate separation (Mathew, Picu, and Bloomfield, 2011). Filtering out high frequency components of the motion therefore provides reasonable knowledge of the mechanical component of the relative atomic motion and enables the algorithm to reliably estimate whether or not there is a demand for the continuum solution. This filtering operation is conveniently accomplished by using well-established low-pass filters from digital signal processing.

Filtering techniques have already been applied to atomistic-to-continuum multiscale models by other researchers (*e.g.*, Mathew, Picu, and Bloomfield, 2011; Ramisetti, Anciaux, and Molinari, 2013; Ramisetti, Anciaux, and Molinari, 2014). In these contributions, the filtering techniques were used to reduce the problem of high frequency phonon reflection at the spatial coupling interface between the scales. Their underlying strategy was to divide the phonon spectrum into low and high frequency components, adopting the idea of an approximate separation of the mechanical and thermal components. The distinction between the two frequency ranges is made in such a way that the low frequency components are admissible to the coarse scale as mechanical waves. The remaining high frequency components are considered as purely thermal. To this end, the Generalized Langevin Equation (GLE) was used as the governing equation of motion for a portion of atoms close to the interface. The filter kernel is used in the damping term of the GLE to filter out the high frequency phonons, reducing the kinetic energy of the atoms. This missing energy is, *e.g.*, restituted by the random force term in the GLE by Mathew, Picu, and Bloomfield (2011) and Ramisetti, Anciaux, and Molinari (2014). The filter therefore directly influences the motion of parts of the atomic region through the GLE.

In this work, the filtering techniques are used in a different way. The presented algorithm and the filtering operation included herein do not modify the governing equations of the concurrent multiscale model at hand (which in case of this work is CADD), but instead estimate the demand to couple the scales in the way that is inherent to the model.

To the author's best knowledge, such a demand-based coupling has not been studied

in the literature. A reason for this might be that the continuum is generally assumed to be computationally inexpensive in comparison to the atomistic region. However, large continuum regions with many degrees of freedom and continuum models of higher complexity result in a non-negligible computational effort spent on the continuum. The approach which is presented in this work is general in the sense that it is applicable to many concurrent atomistic-to-continuum models. However, the CADD method is especially well suited to test the performance of the algorithm, as it incorporates a model in the continuum region which is more complex than others. On top of a standard finite element formulation, CADD has additional features such as the detection and passing of dislocations between the two scales and the time evolution of the discrete continuum dislocations. These features shift computational burden towards the continuum region.

5.2. Demand-based coupling

5.2.1. The CADD method and coupling of the scales

At the heart of all atomistic-to-continuum models lies the spatial decomposition of the solid body of interest into at least one atomistic and one continuum region. Specifically in CADD, a given initial boundary value problem is solved by considering three subproblems (see Fig. 5.1).

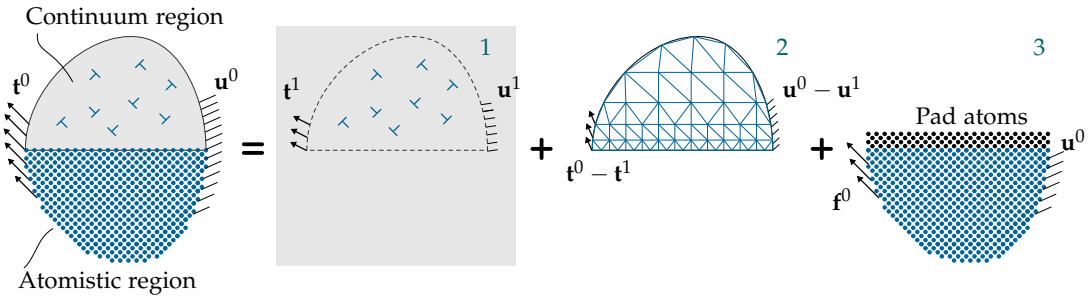

Fig. 5.1.: The three subproblems used in the solution procedure of CADD (see text).

Subproblems 1 & 2 are concerned with the continuum, in which the discrete dislocation methodology of Van der Giessen and Needleman (1995) for isotropic solids is employed. In this methodology, the solution of subproblem 1 yields the displacements and tractions in an infinite isotropic medium due to the discrete dislocations. In subproblem 2, a linear-elastic finite element model (either dynamic or quasi-static[1]) with plane strain

[1]The two approaches are compared in Section 6.2.1.

conditions is used. To correct for the boundary tractions $\mathbf{t}^1$ and displacements $\mathbf{u}^1$, resulting from the discrete dislocations, the boundary conditions in subproblem 2 are modified as shown in Fig. 5.1. In the linear-elastic dynamic FE model, the equation of motion (Eq. 2.21) simplifies to $\mathbf{M}\ddot{\mathbf{u}} + \mathbf{K}\mathbf{u} = \mathbf{f}^{\text{ext}}$, as the internal nodal forces become a linear function of the displacements. If damping is applied, the equation reads $\mathbf{M}\ddot{\mathbf{u}} + \mathbf{D}\dot{\mathbf{u}} + \mathbf{K}\mathbf{u} = \mathbf{f}^{\text{ext}}$, where $\mathbf{D}$ is the damping matrix. In the linear-elastic quasi-static FE model, the discrete equilibrium equation (Eq. 2.26) simplifies to $\mathbf{K}\mathbf{u} = \mathbf{f}^{\text{ext}}$. In contrast to subproblem 1, subproblem 2 may be fully anisotropic.[2]

Subproblem 3 shows the atomistic problem with the pad atoms, which project into the continuum region. These special atoms are attached to the finite elements in which they reside to ensure proper coordination of the atoms close to the interface. The CADD method uses a sharp interface between the regions (instead of a handshake region). At this clearly defined interface, the finite elements are fully resolved down to the resolution of the lattice spacings, so that every interface node is associated with an interface atom and vice versa. To alleviate the important problem of high frequency phonon reflection and ensure temperature stability, Langevin damping (see Section 2.2.4) is commonly used in the finite temperature CADD method.

Like the majority of concurrent atomistic-to-continuum multiscale models, the finite temperature version of CADD uses a fixed time interval coupling (see Fig. 5.2). In this approach, the two scales are coupled at every discrete fine-scale time, *i.e.*, $\Delta t = n\Delta\tau$ with $n = 1$ or at any other number $n > 1$ of fine-scale time steps, with the continuum being quasi-static or dynamic. If a dynamic continuum is used, $n = 1$ is usually chosen, whereas for a quasi-static continuum $n > 1$, (n commonly $\mathcal{O}(10^1) - \mathcal{O}(10^3)$).[3,4]

The coupling of the continuum and atomistic region in the CADD method shall now be described in more detail. First, we focus on the case of $n = 1$, *i.e.*, when both scales use the same time step. Assuming all quantities are known at some discrete instant of time t^n, the evolution of the system to the next discrete instant of time t^{n+1} starts by updating the atomistic region. In this step, the boundary conditions on the atoms imposed by the continuum are given in terms of the pad atom positions, which are dictated by the deformation in the continuum time t^n. In the next step, the continuum is updated to t^{n+1} using the, now known, displacements of the interface atoms at t^{n+1} as the boundary conditions for the finite element interface nodes (see Fig. 5.2).

[2]The isotropic elastic constants needed in the solution of subproblem 1 may, *e.g.*, approximately be found from a set of anisotropic elastic constants by averaging (see, *e.g.* Anderson, Hirth, and Lothe, 2017).

[3]In this work, a dynamic continuum with $n = 1$, *i.e.*, equal time steps on both scales, $\Delta t = \Delta\tau$, is used. However, the presented algorithm is also valid, *e.g.*, for a quasi-static continuum with $n > 1$, *i.e.*, $\Delta t > \Delta\tau$.

[4]It will be shown in Chapter 6 that the choice of n for a quasi-static continuum model is nontrivial and has great impact on the accuracy of the method.

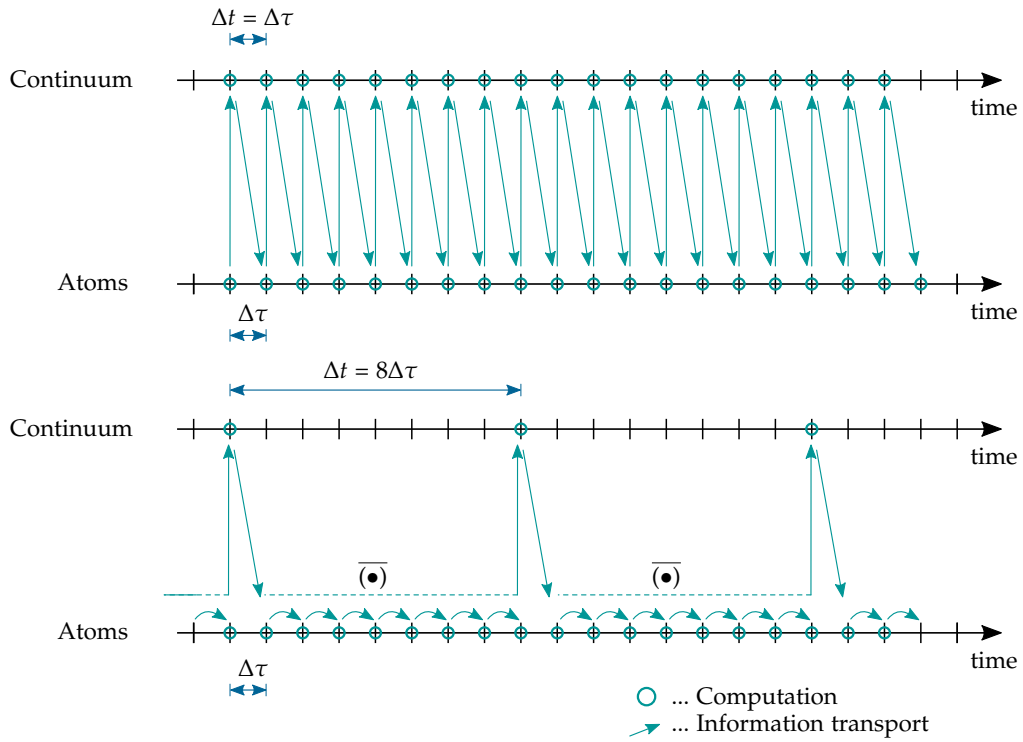

Fig. 5.2.: Two schematics of the information transport between the scales and the sequence of computations in the finite temperature CADD method for the fixed time interval coupling. Both versions have been used in the literature (Qu *et al.*, 2005; Shiari, Miller, and Curtin, 2005). The schematics are similar for other concurrent atomistic-to-continuum multiscale methods. (Top) Coupling of the scales in every fine-scale time step, *i.e.*, $n = 1$. (Bottom) Coupling of the scales in every $n = 8$ fine-scale time steps. The $\overline{(\bullet)}$ symbol represents a time average of the atomic information relevant to the continuum.

For the case that $n > 1$, *i.e.*, when a coarser time step in the continuum is used, the coupling is slightly different. The atomistic region is still updated from one discrete instant of fine-scale time to the next, using the pad atom positions given at the last discrete instant of coarse-scale time. The displacements of the interface atoms are, however, averaged over the fine-scale time steps that happen during a coarse-scale time step. These time averages are then used as the boundary conditions for the finite element interface nodes, to update the continuum to the next discrete instant of coarse-scale time (see Fig. 5.2).

Instead of a fixed time interval coupling, the use of a demand-based coupling to decrease the computational cost while maintaining the same quality of results (see Fig. 5.3) is proposed. In this approach, the atomistic computation is still performed in every fine-scale time step in order to properly trace the dynamics in the atomistic

region. The continuum computation, however, is only performed if demanded. A demand may either originate from the continuum boundary at the interface, if there is a non-negligible deformation in the adjacent atomistic region, or, more trivially, if the boundary conditions of the continuum change at a non-interfacial boundary. For the former scenario, it is therefore essential to observe the deformation close to the coupling interface.

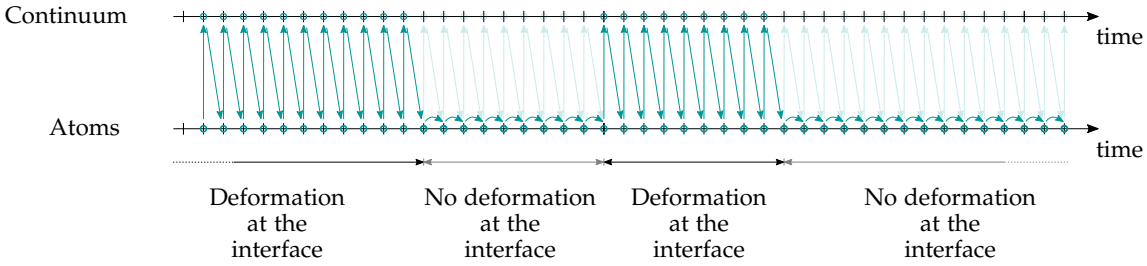

Fig. 5.3.: Schematics as in Fig. 5.2 for the demand-based coupling in case of $n = 1$. For simple illustration, it is assumed that the non-interfacial boundary conditions on the continuum do not change. The schematic for any other $n > 1$ can be given analogously.

This may be achieved by using an algorithm that features a low-pass filter. To facilitate comprehension, a brief introduction to digital filtering is given.

5.2.2. Introduction to digital filtering

Digital filters are used to manipulate discrete signals (*e.g.*, discrete signals in time) in many fields of science and engineering. Mathematically, the output signal y of a finite impulse response (FIR) digital filter may be represented by a convolution of the input signal x and the filter kernel k (Smith, 2002),

$$y^i = \sum_{j=0}^{M-1} k^j \, x^{i-j}, \tag{5.1}$$

where y^i is the value of the output signal at time t^i, x^{i-j} is the value of the input signal at time t^{i-j} and M is the length of the finite filter kernel. This can be written in the usual shorthand notation as $y = k * x$.

More specifically, low-pass filters manipulate signals by passing signal components of frequencies below a defined cut-off frequency, while attenuating signal components of higher frequencies. Examples of low-pass filter kernels and their frequency responses are shown in Fig. 5.4.

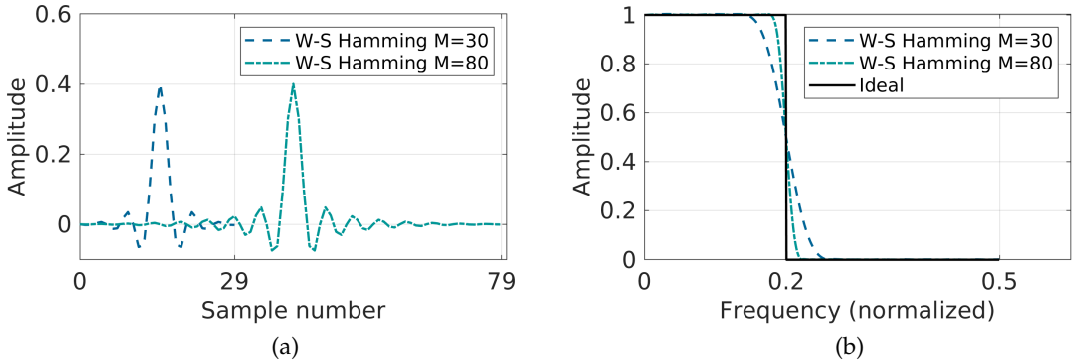

Fig. 5.4.: (a) Two examples of low-pass filter kernels. The ideal filter kernel (not shown) is infinitely long and the windowed-sinc filter kernels are of finite length. (b) Frequency responses of the filter kernel examples. The ideal filter kernel has no transition band, *i.e.*, it yields the desired abrupt change in amplitude at the transition from passband to stopband. The windowed-sinc filter kernels can only approximate the ideal kernel behavior and therefore exhibit a finite transition band.

In practice, the so-called windowed-sinc filter kernels are commonly used. These filters shift the phase of the output signal with respect to the input signal by a time delay of

$$\Delta t^{\text{delay}} = (M-1)/(2f^{\text{s}}), \tag{5.2}$$

where f^{s} is the sampling rate of the input signal. A number of different windows can be used for the windowed-sinc filter kernel, each having its own characteristics (Smith, 2002). For example, the value of a windowed-sinc filter kernel with Hamming window at time t^j is given by[5]

$$k^j = K^{\text{f}} \frac{\sin\left(2\pi f^{\text{c}*}(j-M/2)\right)}{j-M/2} \left(0.54 - 0.46\cos\left(2\pi j/M\right)\right). \tag{5.3}$$

The kernels shown in Fig. 5.4a are representatives of this type of kernel. In the above equation, K^{f} is a normalization constant and $f^{\text{c}*}$ is the normalized cut-off frequency given by $f^{\text{c}*} = f^{\text{c}}/f^{\text{s}}$. The normalized cut-off frequency takes only values $0 \leq f^{\text{c}*} \leq 0.5$ due to the Nyquist-Shannon sampling theorem (Smith, 2002). The two quantities needed to design these kernels are the cut-off frequency f^{c} and the kernel length M. The proper choice of these quantities is discussed in the next sections.

[5]The case $j = M/2$ must be treated separately.

5.2.3. The algorithm in detail

Detection of deformation

In the detection of deformation, the common continuum mechanics approach of defining local deformation as the change in distance between two material points in close proximity, is applied. To this end, the algorithm monitors the relative motion of the coupling interface and a band of atoms close to the interface (see Fig. 5.5).

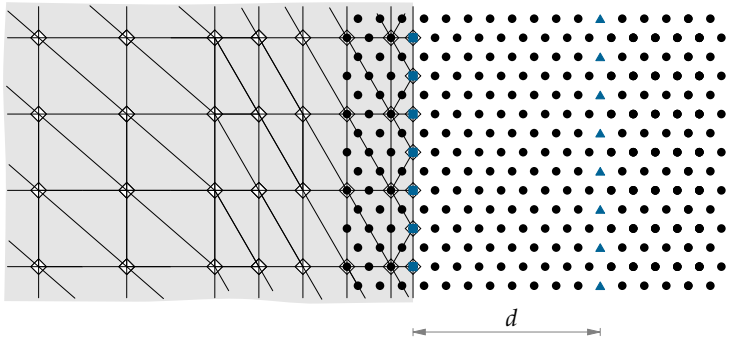

Fig. 5.5.: Close-up view of the spatial interface in the CADD method with the continuum region on the left side and the atomistic region on the right side. The relative motion of the interface atoms (blue squares) and a band of atoms (blue triangles) in distance d to the interface is monitored by the algorithm.

Pairs of atoms are generated by associating each band atom with the closest interface atom (see Fig. 5.6a) in the initial configuration. The relative motion of these pairs is monitored subsequently (see Fig. 5.6b and Fig. 5.6c).

As explained above, a windowed-sinc low-pass filter with Hamming window[6] in each spatial direction α is applied to every pair to approximately eliminate the thermal fluctuations in the relative motion. The input signal for every filter is the relative motion of the respective pair $\mathbf{r}^{\mathrm{B}} - \mathbf{r}^{\mathrm{I}}$, the output signal

$$\mathbf{y} = \mathbf{k} * \left(\mathbf{r}^{\mathrm{B}} - \mathbf{r}^{\mathrm{I}} \right) \tag{5.4}$$

gives a satisfactory representation of the deformation in the pair[7]. Fig. 5.7 shows exemplarily the application of the filter to a pair in equilibrium in a one-dimensional

[6]The use of other filter windows is readily possible.

[7]Due to the distributivity property of the convolution operation, $k * (a + b) = k * a + k * b$, this is equal to applying the filter separately to the motion of the two atoms in the pair and subsequently subtracting the individual output signals.

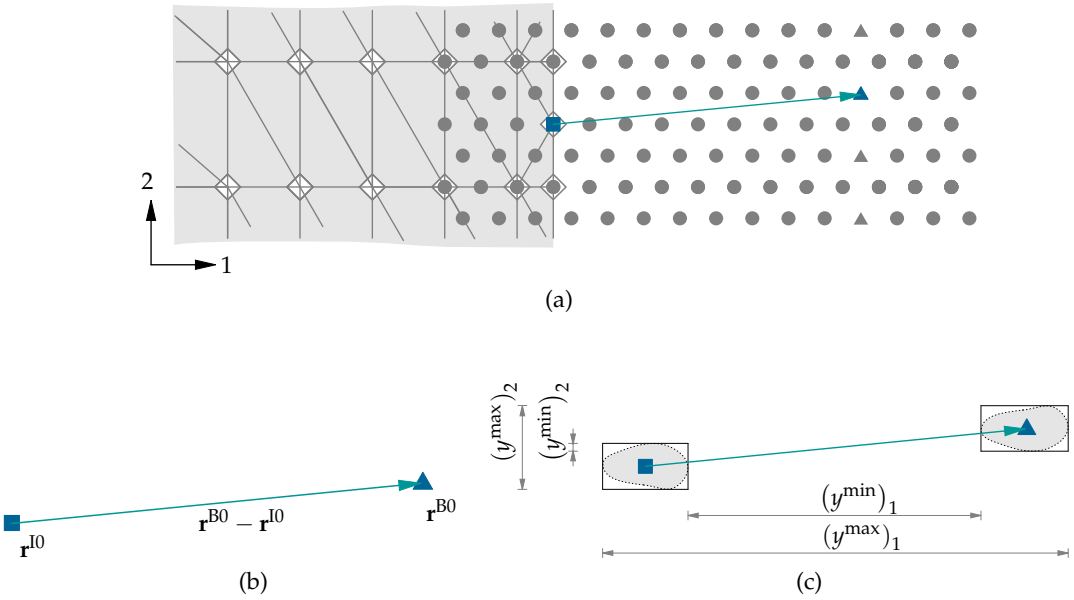

Fig. 5.6.: Illustration of the detection of deformation in the algorithm. (a) A band atom B (blue triangle) and its associated interface atom I (blue square). (b) Initial position. (c) After tracing the system.

problem. The filter is clearly able to yield an output signal which is practically void of frequency components above the chosen cut-off frequency.

Furthermore, this figure also illustrates the fact that the filter output is not vanishing, even despite no external deformation being applied. As mentioned above, a strict separation of the mechanical and thermal components in the atomic motion is not possible. Thus, the low frequency phonons passing the filter are also carrying thermally induced information. The output signal (the deformation) in equilibrium therefore shows finite fluctuations of amplitude $\Delta\mathbf{y} = \mathbf{y}^{max} - \mathbf{y}^{min}$ around the relative equilibrium distance of the pair atoms, the magnitude of which is characteristic for the system at hand (*e.g.*, lattice type, temperature level, *etc.*). Only deformation that exceeds these equilibrium fluctuations should be considered as relevant by the algorithm. It is therefore necessary to determine the magnitude of these fluctuations before the algorithm can be applied to a given problem. This can practically be done by tracing the system at hand in equilibrium for a brief period of time and keeping track of the fluctuations in the output signals of the filters. It should be noted, that the computational time spent on this task, however, commonly does not represent an additional effort. This is because in most practical finite temperature simulations, the system at hand has to undergo a transient period to reach thermal equilibrium before the actual problem is studied. This preliminary period can conveniently be used to record the magnitude of the equilibrium fluctuations. Also, in case of multiple simulations of the same system,

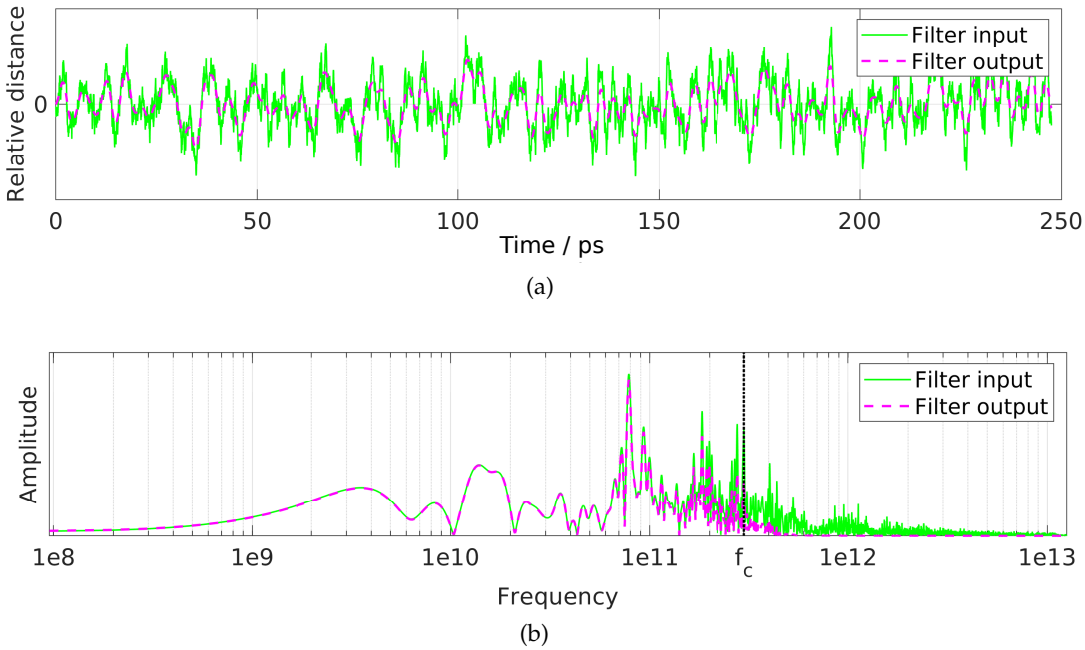

Fig. 5.7.: Application of the filter to a pair of band atoms and interface atoms in a one-dimensional problem at equilibrium. (a) Despite no external deformation being applied, the filter output is not vanishing (see text). Windowed-sinc filters have a time delay. For clearer presentation, the output signal was shifted to account for this time delay. (b) The frequency response of the filter output is practically void of any components of higher frequency than the cut-off frequency $f^c = 3 \times 10^{11}$ Hz.

the magnitude of equilibrium fluctuations must only be recorded once and can then be reused.

Non-negligible deformation is therefore detected by the algorithm if the condition

$$y_i^{\min} \leq y_i \leq y_i^{\max} \tag{5.5}$$

is violated for any spatial coordinate i.

Once this condition is violated, the continuum is activated at least for a time interval Δt^c. This is to ensure that the detected deformation at the band has enough time to travel to the interface, before the continuum becomes inactive again. The time interval Δt^c therefore depends on the lowest relevant phase velocity in the system and the distance d. If the condition in Eq. 5.5 is violated during the active continuum time, the interval is refreshed.

Low-pass filter design

The two parameters needed in the low-pass filter design are the kernel length M and the cut-off frequency f^{c}.

The kernel length is chosen to give a proper balance of efficiency and accuracy. Larger kernel lengths yield a narrower transition band (see Fig. 5.4b) and therefore represent the ideal kernel behavior more accurately. On the other hand, larger kernel lengths also increase the computational cost of the convolution operation and its associated memory consumption. As mentioned above (see Eq. 5.2), the kernel length also directly affects the time delay of the filter. Thus, the algorithmic detection of deformation is delayed in time, which means that the band of atoms must not be chosen too close to the interface, to account for this delay. The continuum might otherwise be activated too late, probably missing the deformation. The distance of the band atoms from the interface d can be easily adjusted to the time delay $\Delta t^{\mathrm{delay}}$ and the maximum phase velocity.

The cut-off frequency represents the (artificial) limit between the mechanical and thermal frequency components. A natural choice for the cut-off frequency is given by the maximum admissible continuum frequency f^{FE}. Only phonons with frequencies below f^{FE} are admissible as mechanical waves to the continuum, whereas all higher frequency phonons will be (unphysically) reflected in the continuum. Caution must however be taken if large, *e.g.*, micron-sized, elements are present in the finite element mesh, which results in a low maximum admissible continuum frequency. In this case, the choice $f^{\mathrm{c}} = f^{\mathrm{FE}}$ may lead to large filter delays for adequate filter quality and may result in exceedingly large distances d of the band of atoms from the interface. Or worse, $f^{\mathrm{c}} = f^{\mathrm{FE}}$ may even be below the smallest frequency of the atomic motion $f^{A,\mathrm{min}}$, which depends on the size of the atomistic region. In both of these cases, the choice $f^{\mathrm{c}} = f^{\mathrm{FE}}$ is inappropriate, and a larger cut-off frequency must be chosen. An appropriate choice hence must always satisfy $f^{\mathrm{c}} > f^{A,\mathrm{min}}$ and must yield an adequate distance of the band atoms from the interface.

Efficiency

A number of simple measures can be introduced to cut the costs of the algorithm, which are dominated by the convolution operation (Eq. 5.1). These measures include a limitation of the kernel length M, and the number of band atoms N^{B}, using Fast Fourier Transform (FFT) convolution and downsampling of the filter input signal.

The last measure requires a brief explanation. Downsampling lowers the filter input signal rate f^{s} close to the lowest possible alias-free sampling rate f^{Ny} (the Nyquist

sampling rate[8]). This corresponds to a downsampling operation, *i.e.*,

$$\hat{x}^i = x^{Di} \qquad D \in \mathbb{N} \tag{5.6}$$

using a positive integer factor D. Small numerical time steps must commonly be used in molecular dynamics. As a consequence, the atomic motion has a large sampling rate in the order of 10^{15} Hz, while the maximum frequency of the atomic vibration is commonly 1-2 orders of magnitude smaller. This allows for a downsampling by $D \sim \mathcal{O}(10^1 - 10^2)$, thus reducing the total number of convolution operations performed by a factor of D. Additionally, the downsampling allows for a reduction of the kernel length M by the same factor, while maintaining the accuracy of the filter (*i.e.*, the same transition band width). Smaller kernel lengths reduce the individual cost of every convolution operation performed. In summary, the use of downsampling therefore reduces the computational cost of the filter operation by a factor of $\mathcal{O}(D^2)$, while being straightforward to implement.

Memory-wise, the algorithm requires to save a record of the band atom position vector in time with the size of the kernel length M, the memory requirement of which can be computed (for double-precision storage) as $\mathrm{Mem} = 8\,\mathrm{Byte} \times \mathrm{N_d} \times M \times N^{\mathrm{b}}$, where $\mathrm{N^d}$ is the number of spatial dimensions and N^{b} is the number of band atoms. For most applications, this memory consumption should be negligible.

The computational savings provided by the application of the algorithm for each of the examples presented is given below. In the case of the in-house software and examples used in this study, the potential savings outweigh its cost by a factor of 60 to 65.

Continuum energy

The algorithm manipulates the coupling by skipping the continuum computation at certain times, which is tantamount to freezing the continuum. During these inactive periods, the potential energy of the continuum is preserved, as the positions of the finite element nodes are kept constant. If a quasi-static continuum (Qu *et al.*, 2005) is used, there is no kinetic energy in the continuum, which means that the algorithm preserves the total energy of the continuum in the inactive periods. If a dynamic continuum (Shiari, Miller, and Curtin, 2005) is used on the other hand, the presence of kinetic energy poses the question of how to treat this quantity which is governed by the velocities of the finite element nodes. It was found that the most obvious choice, preserving the kinetic energy, is also the most adequate. This means that in addition to the nodal positions, the nodal velocities are also frozen in inactive periods. Therefore,

[8]The Nyquist sampling rate is twice the maximum frequency of the input signal.

the total energy of the continuum is also preserved in the inactive periods for the dynamic continuum.

In comparison to the fixed time coupling, the application of the proposed algorithm obviously leads to altered dynamics of the continuum as the motion of the continuum is frozen from time to time. However, it can be noted that this issue is often negligible. In most cases, the main task of the continuum region is to provide the proper elastic response to give correct boundary conditions for the atomistic region. Therefore, the specific dynamics in the continuum region are often of secondary importance, as long as proper boundary conditions on the atomistic region are generated. Naturally, if accurate continuum dynamics are of particular interest to the researcher, or if the altered continuum dynamics are assumed to significantly affect the atomistic regions, the application of the algorithm is not advised.

Overview

The steps involved in the algorithm can be summarized as follows:

Preliminary steps

1. Design the filter by defining the parameters M and f^{c}.
2. Select the band atoms in distance d and associate each with the nearest interface atom.
3. Trace the system in equilibrium and record the equilibrium fluctuations $\Delta\mathbf{y}$ for every pair of band atom / interface atom.

Execution The low-pass filter is applied in every spatial direction α to the relative motion of each atom pair. If the condition in Eq. 5.5 is violated or if the non-interfacial boundary conditions on the continuum change, the continuum solution is computed. If not, the continuum computations are skipped and the subsequent steps in the model at hand are performed (see Fig. 5.8).

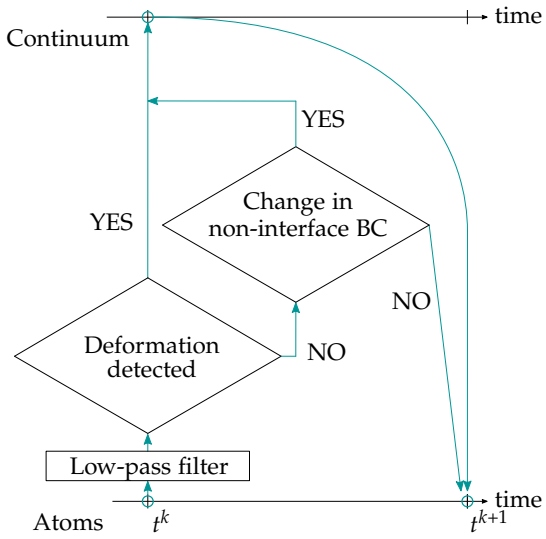

Fig. 5.8.: Flow diagram of the execution phase.

5.3. Numerical Examples

To show the potential savings of the proposed demand-based coupling approach, three numerical examples are studied. In the first two examples, the propagation of pulses in a one- and a two-dimensional domain is studied, respectively. The third example is concerned with nanoindentation in a two-dimensional domain.

Aluminium is the material of interest in all examples, and the Lennard-Jones (LJ) potential (see Section 2.2.4) is used as the interatomic potential with parameters from Halicioğlu and Pound (1975). A cut-off radius of 3 times the equilibrium lattice spacing is applied. The continuum region in the examples is discretized with linear 1D elements (in the 1D example) and linear triangle elements (in the 2D examples). The anisotropic elastic constants and mass densities of the continuum as well as the equilibrium lattice spacings at the studied temperatures are found by separate MD simulations using the given interatomic potential.

The velocity verlet algorithm (see Section 2.2.4) is used as a time integrator to evolve the equations of motion in both regions. A fine-scale step of $\Delta\tau = 1\,\mathrm{fs}$ is used in all examples. In the finite element approximation, a lumped mass matrix is used, which is obtained by row-summation (see, *e.g.*, Zienkiewicz and Taylor, 2000).

5.3.1. Pulse propagation (1D)

In this example, the propagation of longitudinal pulses of different characteristic frequency spectra is studied. The pulses propagate from an atomistic to a continuum region in the 1-dimensional body shown in Fig. 5.9. The left end of the continuum region is clamped and the right side of the atomistic region is used to introduce the pulses. To this end, the motion of the 3 atoms on the far right is controlled. The atomistic region consists of 500 aluminum atoms at a temperature of 100 K and an equilibrium atomic spacing of $a = 2.95\,\text{Å}$.

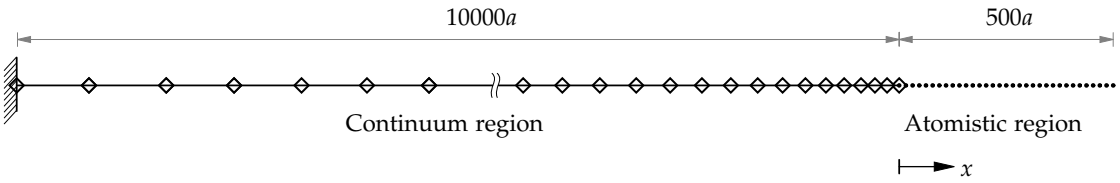

Fig. 5.9.: Geometry of the 1-dimensional example.

Standard Newtonian dynamics is used for all atoms, except those in the Langevin damping region given by the first 6 atoms next to the interface. The equations of motion for the damped atoms are (*cf.* Eq. 2.52)

$$m\ddot{x} = f - m\gamma(x)\dot{x} + f^{\mathrm{r}}, \tag{5.7}$$

where $\ddot{x}$, $\dot{x}$ and m are the acceleration, velocity and mass of the atom and f is the interatomic force acting on the atom. The Langevin damping introduces the damping force $-m\gamma(x)\dot{x}$ and the random force f^{r}, which are related by the fluctuation-dissipation theorem (Kantorovich, 2008a; Kantorovich, 2008b). Here, the so-called stadium damping approach (Holian and Ravelo, 1995; Qu *et al.*, 2005), is used where the damping coefficient is linearly increasing towards the interface from zero to the maximum damping coefficient γ. From separate MD simulations, $\gamma = 4.52 \times 10^{12}\,\mathrm{s}^{-1}$ was found as a suitable choice, which ensures temperature stability and proper canonical temperature fluctuations. The chosen value for γ corresponds to the dimensionless value $\gamma^* = 1$ in reduced LJ units, *i.e.*, $\gamma^* = \gamma\sigma\sqrt{m/\varepsilon} = 1$, where σ is the distance at which the potential takes a value of zero and ε is the depth of the potential well in the LJ potential. Generally, γ should neither be chosen too small, as this leads to poor temperature control, nor too large, as this leads to significantly perturbed dynamics (see, *e.g.*, Hünenberger, 2005). The proposed algorithm should not be sensitive to the choice of γ, although a detailed analysis was not performed and is left for future research. The same value for γ is used in all presented examples.

In the continuum region, a dynamic finite element formulation with a mesh that consists of 464 nodes is used. The maximum admissible frequency for the continuum is given

as

$$f^{\mathrm{FE}} = \frac{6}{\pi}\sqrt{\frac{2\varepsilon}{m}}\frac{1}{h^{\max}} \approx 3 \times 10^{11}\,\mathrm{Hz}, \tag{5.8}$$

where and $h^{\max} = 41a$ is the length of the largest finite element.

The system is studied for 500 ps and a time step of $\Delta t = \Delta\tau = 1\,\mathrm{fs}$ is used in both regions. In the 1-dimensional example, the band of atoms which is monitored by the algorithm reduces to a single atom. The atom in a distance of $d = 50a$ to the interface is chosen as the band atom. The time interval Δt^{c} is chosen to be 2.5 ps and a transient period of 50 ps is used to record the equilibrium fluctuation of the band atom. A kernel length of $M = 38$ is used in the filter design, which ensures adequate accuracy and time delay and a cut-off frequency of $f^{\mathrm{c}} = f^{\mathrm{FE}}$. Furthermore, a downsampling is applied to the atomic position over time with an integer of $D = 40$. This yields a sampling rate for the input signal of $f^{\mathrm{s}} = 2.5 \times 10^{13}\,\mathrm{Hz}$, which is above the Nyquist sampling rate $f^{\mathrm{Ny}} = 2f^{\max} = 2.172 \times 10^{13}\,\mathrm{Hz}$, where $f^{\max}$ is the maximum frequency of the atomic vibration given as

$$f^{\max} = \frac{6}{a\pi}\sqrt{\frac{2\varepsilon}{m}}. \tag{5.9}$$

The results for the algorithm applied to CADD (*CADD+A*) are compared against the reference solution of the plain CADD method (*CADD*). Fig. 5.10 shows the results of this study, where the system's mechanical behavior is studied through the evolution of the positions over time at various points. The graph for $x \in (497a, 500a)$ shows the boundary condition imposed on the rightmost atoms. The motion of these atoms is controlled to introduce the same two pulses followed by a permanent deformation in both simulations. As can be seen in the figure, the algorithm applied to CADD is able to produce results which are of the same quality as the plain CADD solution, while using far fewer continuum computations. It was also verified that the temperature in the atomistic region behaves similarly in both simulations (not shown).

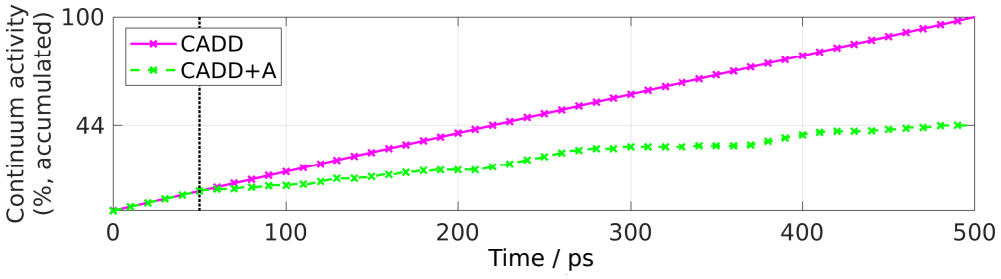

Fig. 5.11.: Comparison of the accumulated number of active continuum time steps for *CADD vs. CADD+A*.

The application of the algorithm causes the continuum to be activated only when

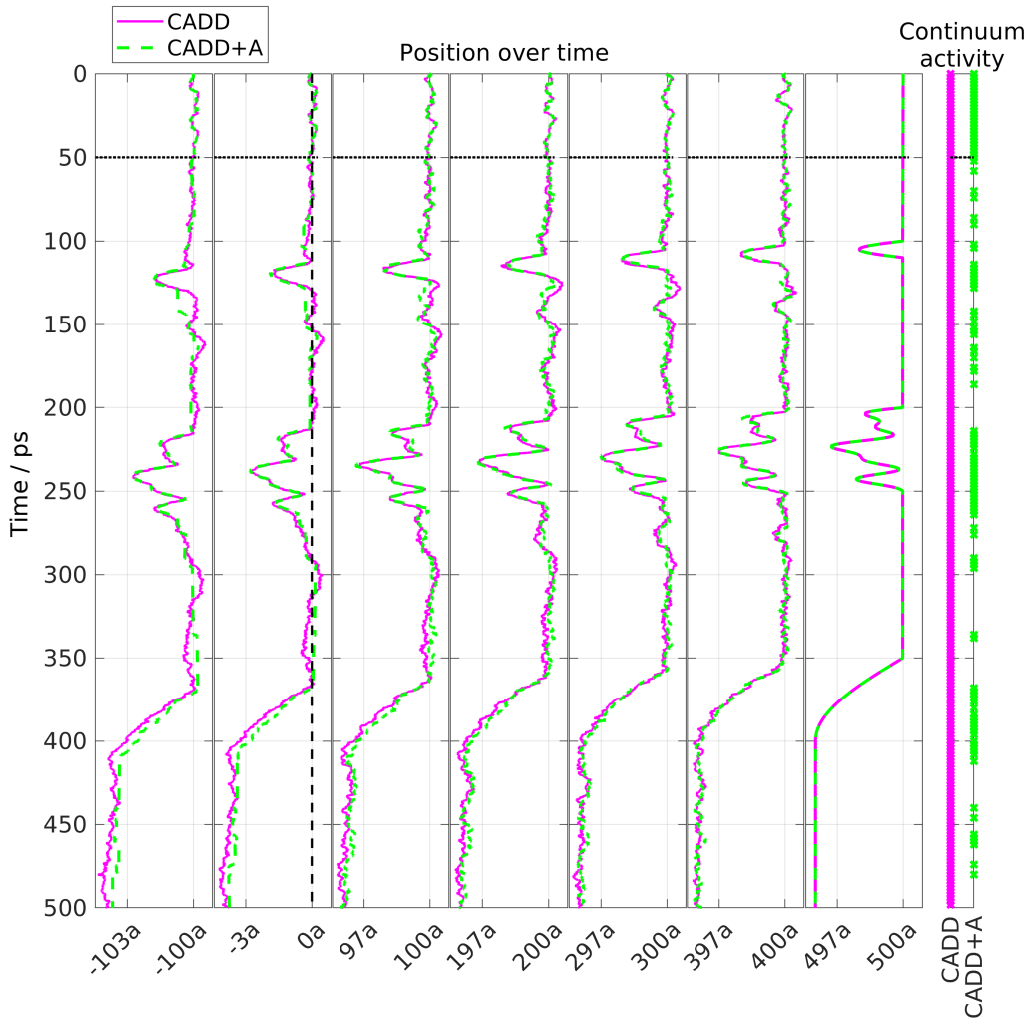

Fig. 5.10.: Results of the 1-dimensional problem. The evolution of the position of a number of points for *CADD* and *CADD+A* are compared. The initial position of the interface is given by the vertical dashed black line. The two graphs on the far left therefore show the position of two finite element nodes and the other graphs show atom positions. The end of the transient period used to record the equilibrium fluctuations is given by the horizontal dotted black line. The graph on the very right shows the activity in the continuum for *CADD vs. CADD+A*.

deformation is taking place at the interface, while skipping the intermediate continuum computations. As a consequence, more than half of the continuum computations can be skipped in this example (56%). This amounts to a saving of 22% of the total simulation

time. This is also illustrated in Fig. 5.11, where the accumulated number of active continuum time steps are compared.

5.3.2. Pulse propagation (2D)

The propagation of pulses is now studied in a 2-dimensional example adapted from the literature (see Qu *et al.*, 2005). The geometry of the example is shown in Fig. 5.12 and the parameters used are given in Tab. 5.1.

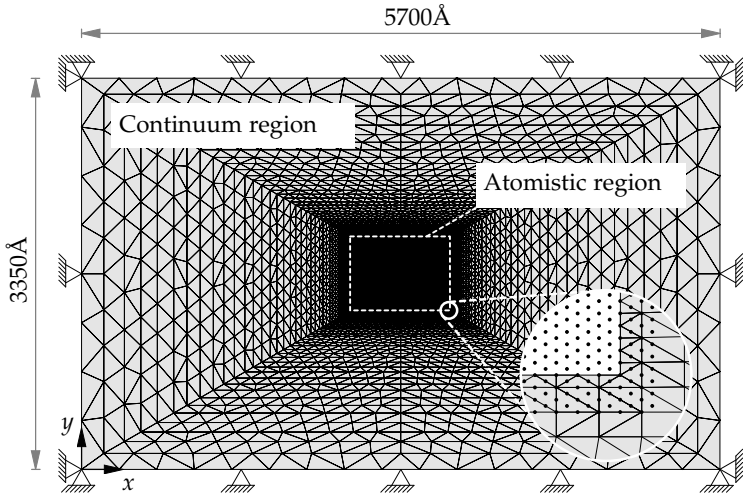

Fig. 5.12.: Geometry of the 2-dimensional pulse propagation example.

γ	$4.52 \times 10^{12}\,\mathrm{s}^{-1}$
a	2.9158 Å
d	$50a$
M	38
f^{c}	3×10^{11} Hz
Δt^{c}	2.5 ps
Transient period	50 ps
D	40
T	50 K

Tab. 5.1.: Parameters used.

The material studied is hexagonal aluminum with the c-axis aligned normal to the x, y-plane. The lattice orientation is such, that the x- and y-axes are aligned with the $[\bar{1}100]$- and $[11\bar{2}0]$-directions of the crystal, respectively. In the atomistic region, 200 atomic planes in the x- and 150 atomic planes in the y-direction are used, which results in a total of 60351 atoms. Furthermore, a radially outwards propagating pulse is introduced in the center of the atomistic region by applying a radial displacement of the form (Wagner and Liu, 2003)

$$\Delta r = A \frac{\exp[-r^2/\Lambda^2] - \exp[-(r^{\mathrm{cut}})^2/\Lambda^2]}{1 - \exp[-(r^{\mathrm{cut}})^2/\Lambda^2]} \qquad r \leq r^{\mathrm{cut}} \tag{5.10}$$

to all atoms inside a circle with midpoint at the center of the atomistic region and a radius equal to the cut-off radius. The maximum amplitude is chosen as $A = 2$ Å. The characteristic frequency spectrum of the pulse is governed by the quantity Λ, which is chosen as $\Lambda = 3a$.

The system is allowed to reach thermodynamic equilibrium and the equilibrium fluctuations are recorded in a transient period of 50 ps (the transient period is not shown in the results). The simulation is started subsequently and the system's response is studied for 40 ps in total. A pulse according to Eq. 5.10 is introduced at $t = 1$ ps. Fig. 5.14 shows the comparison of the pulse propagation for *CADD* and *CADD+A*. The evolution of the temperature of the undamped atomistic region is compared in Fig. 5.13.

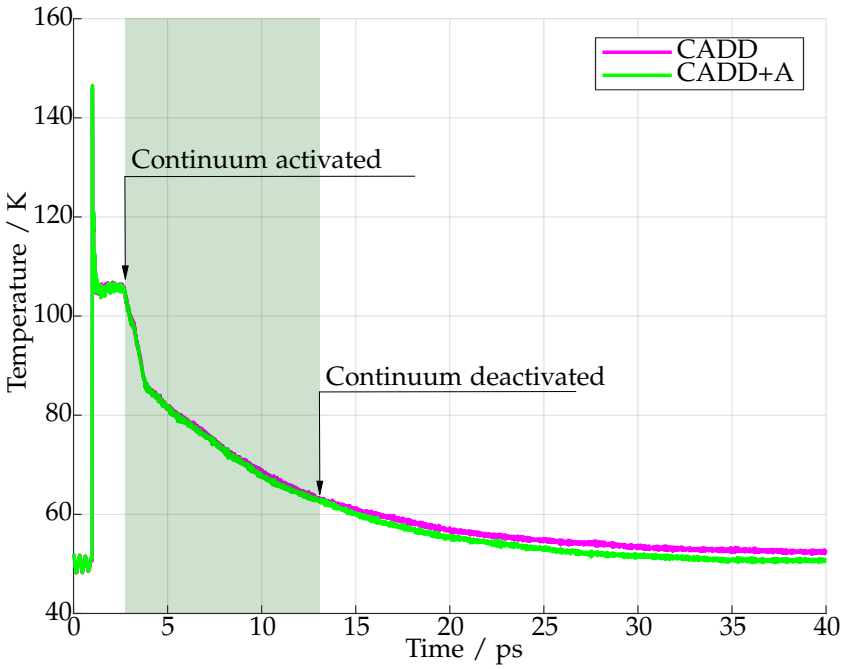

Fig. 5.13.: Temperature of the undamped atomistic region over time.

The algorithm detects a non-negligible deformation at $t = 2.9$ ps and activates the continuum. The pulse is fully located in the continuum region after $t = 6.5$ ps, and the deformation close to the coupling interface returns to a regular level at $t = 10.4$ ps. When the time interval $\Delta t^{\mathrm{c}} = 2.5$ ps has passed after this last activation, the continuum is deactivated at $t = 12.9$ ps. This example demonstrates nicely that in such a case, a full tracking of the dynamic evolution of the continuum, can be considered as nonessential. The displacement field in the continuum is frozen from this point onwards (see Fig. 5.14) as accuracy is only required in the atomistic region.

In Fig. 5.13, it can be seen that the system cools down slightly faster for *CADD+A* than for *CADD*, which is due to unphysical phonon reflection in the finite element mesh (*i.e.*, energy is transported back towards the atomistic region). This influence can be reduced, for example, by using continuum damping or using stronger damping in the

stadium damping region.

Comparing the simulation time after the pulse has reached the continuum, the savings in terms of skipped continuum computations are 73% in this example. This amounts to a saving of 29% of the total simulation time.

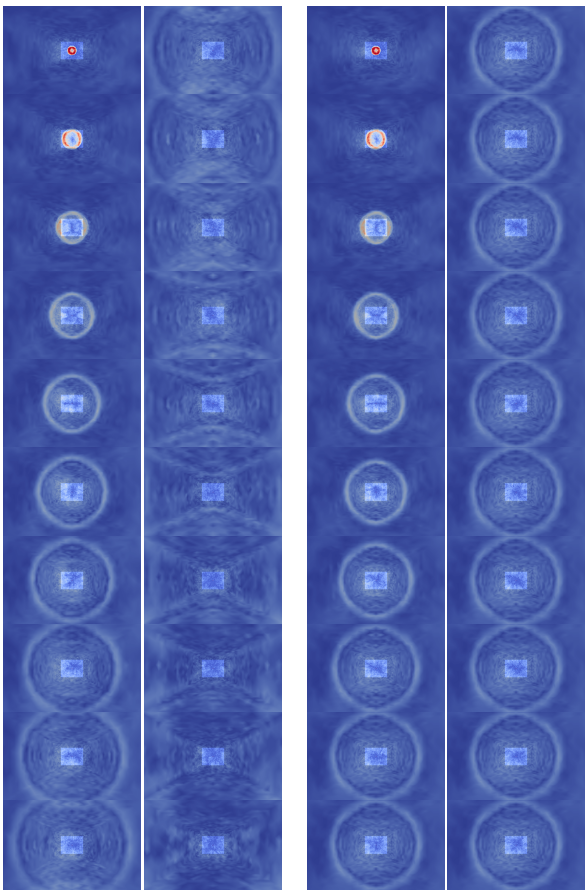

(a) (b)

Fig. 5.14.: Snapshots of the outwards propagating pulse at every 1.5 ps from 2 to 30.5 ps. (a) *CADD*, (b) *CADD+A*.

5.3.3. Nanoindentation (2D)

The performance of the presented algorithm is now demonstrated in combination with a unique feature of CADD, this being the detection of dislocations and their passing

from one domain to the other. To this end, a two-dimensional nanoindentation problem is studied, the geometry of which is shown in Fig. 5.15b.

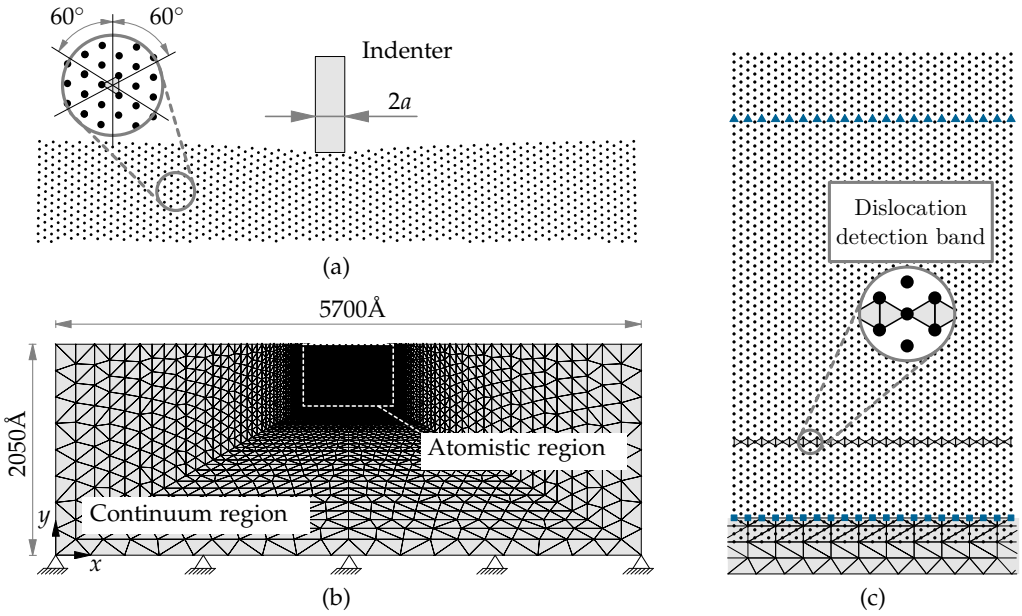

Fig. 5.15.: (a) Close-up view of the indenter shortly before the nucleation of the first dislocation pair. (b) Geometry of the 2-dimensional nanoindentation example. (c) Close-up view of the spatial interface region. The dislocation detection band should not be confused with the band of atoms that is used to detect deformation by the presented algorithm (the "deformation detection band").

The same material, atomistic potential, size of the atomistic region, simulation parameters and algorithm parameters (see Tab. 5.1) are used as in the last example. The material has three slip systems, one of which is aligned with the vertical direction and the other two are $\pm 60^\circ$ from the vertical (see Fig. 5.15a). The indentation is performed with a rigid square indenter of width $2a$ (see Fig. 5.15a), which is simulated by controlling the motion of 3 layers of atoms of the width as mentioned at the top of the atomistic region. The indenter is driven into the material at a speed of about 140 m/s and causes the generation of six pairs of closely spaced Shockley partial dislocations. The indentation takes place from $t = 1$ ps to $t = 16.6$ ps and the response of the system is tracked for 25 ps.

The nucleation and propagation of the dislocation pairs for *CADD* and *CADD+A* is compared in Fig. 5.16. The dislocations travel towards the interface in the vertical slip system. Once the dislocations are close to the interface, they are detected by the dislocation detection band[9], inherent to the CADD method, and then passed to the

[9]In the CADD method, the so-called dislocation detection band continuously monitors the motion of

continuum. The dislocation detection band is shown in Fig. 5.15c. In *CADD+A*, the algorithm detects non-negligible deformation at $t = 7\,\mathrm{ps}$ and activates the continuum.

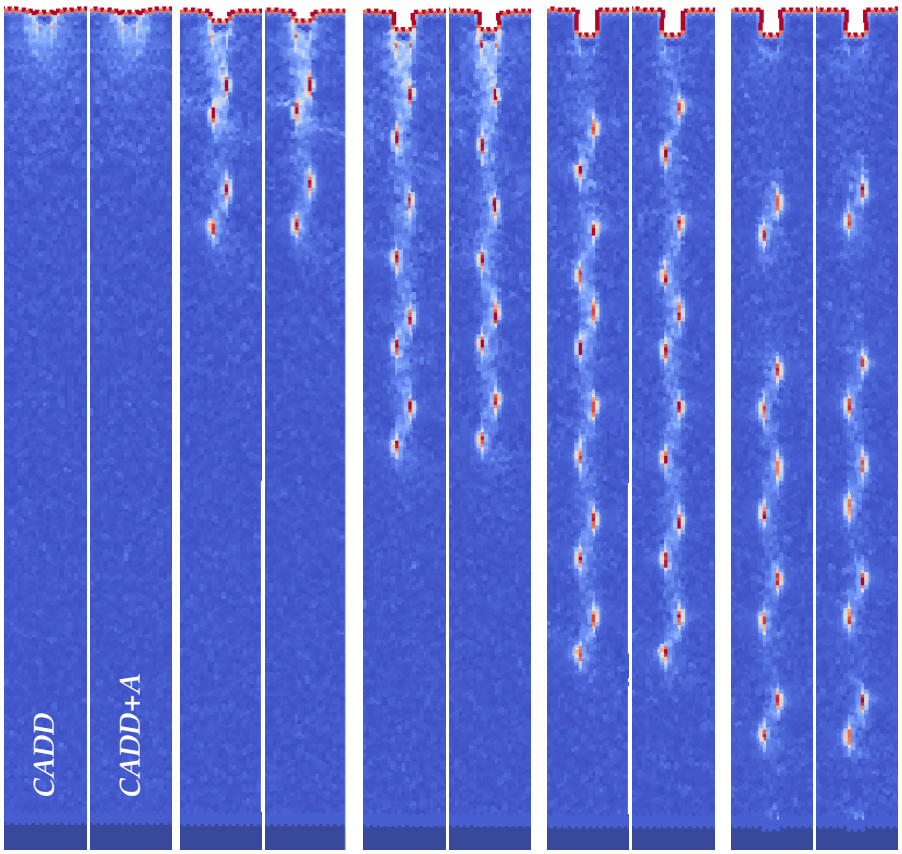

(a) $t = 4.6\mathrm{ps}$ (b) $t = 9.2\mathrm{ps}$ (c) $t = 13.8\mathrm{ps}$ (d) $t = 18.4\mathrm{ps}$ (e) $t = 23\mathrm{ps}$

Fig. 5.16.: Snapshots of the edge dislocations traveling towards the interface at five instances of time. The dislocations are made visible using the local difference in potential energy. In (e), the first pair of dislocations is already inside the continuum.

The vertical force on the indenter of *CADD* and *CADD+A* is compared in Fig. 5.17. The nucleation of the dislocations is clearly visible as force peaks. The two dislocations of pairs 1 and 2 nucleate practically simultaneously. The two dislocations of pairs 3 to 6 nucleate with a temporal offset of $0.6 - 1.3\,\mathrm{ps}$, which is noticeable by two distinguished force peaks in each case. As a reference, the vertical force on the indenter for the case of a rigid continuum (*CADD rigid*) is included, to show how strongly the deformation of

its atoms to identify possible dislocations that pass the band. To detect the dislocations, a version of the algorithm developed by Stukowski (2014) is used.

the continuum affects the nucleation of the pairs. In fact, the reduced elastic deformation due to the rigid continuum causes the nucleation of a 7-th pair of dislocations.

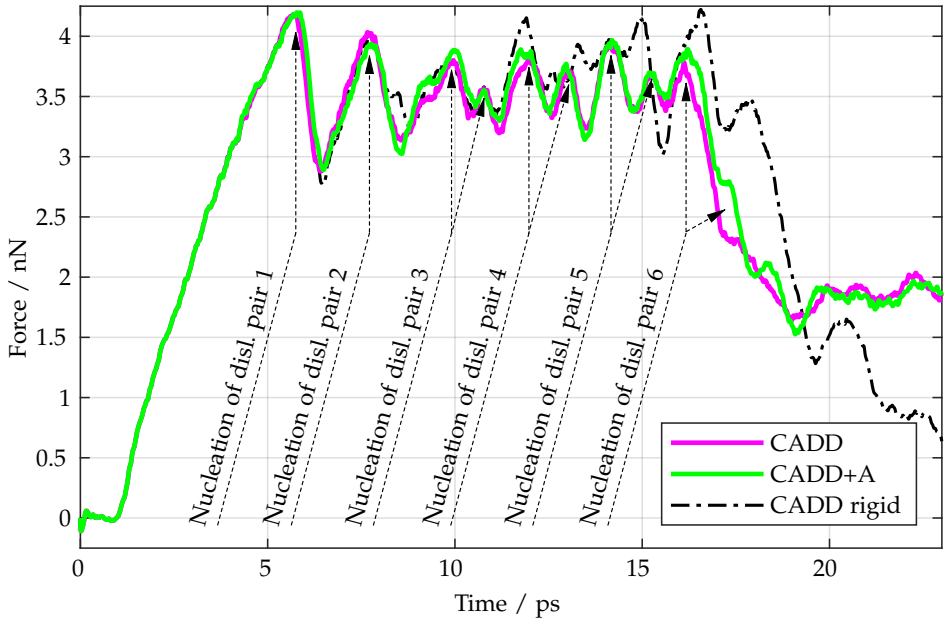

Fig. 5.17.: Force over time. To reduce the effect of the thermal fluctuations, the force was averaged over a period of 0.5 ps.

The savings in terms of skipped continuum computations are 30% in this example. This amounts to a saving of 12% of the total simulation time. Further to this, there is an additional advantage when the presented algorithm is used in combination with a dislocation detection. By means of a sensible placement of the deformation detection band with respect to the dislocation detection band, the dislocation detection algorithm does not have to be continuously active. Dislocations traveling towards the interface will first be detected as deformation by the presented algorithm. The dislocation detection algorithm therefore only needs to be active if deformation has been detected beforehand, saving additional computational time.

Special care must be taken if the continuum is deactivated after dislocations have been passed to the continuum, which show the tendency to continue traveling. Once deactivation happens, these dislocations are trapped in place. If their trapped position is near the interface, newly approaching dislocations in the atomistic region will experience their influence due to the long range nature of dislocation interaction. This will then lead to altered global dislocation dynamics. This issue can be prevented in the following way. If there are any moving continuum dislocations in the interfacial

vicinity, the continuum should not be deactivated until these dislocations have moved beyond a certain distance from the interface. As the dislocation interactions decay linearly with distance, r^{-1} (Anderson, Hirth, and Lothe, 2017), the distance should be at least 100 times the Burgers vectors magnitude b. It was numerically verified, that at $140b$, the influence of the trapped dislocations is negligible. On the other hand, if the near-interface continuum dislocations do not show the tendency to move away from the interface, the issue is not immanent and the continuum may be deactivated safely once these dislocations have settled.

6. A hybrid continuum model for dynamic concurrent atomistic-to-continuum methods

This chapter is a modified version of a manuscript which is in preparation for submission as of the writing of this thesis.

6.1. Introduction

The continuum region in concurrent atomistic-to-continuum methods is usually either dynamic or quasi-static (*cf.* Section 5.2.1) with a dynamic continuum model being much more common. This is easily explained considering that a dynamic continuum model (in combination with the dynamic atomistic model, *i.e.*, molecular dynamics) ensures maximum compatibility between the scales. However, a dynamic continuum model introduces a practical drawback which has been pointed out by Qu *et al.* (2005). When studying problems that require large continuum regions, a change in the external boundary conditions (BCs) of the continuum takes an exceedingly long time to affect the atomistic region. This is critical, as the time intervals that can be studied with these methods are very limited, even with the use of high-performance parallel computing. Qu *et al.* (2005) solved this issue ad-hoc by using a quasi-static continuum model instead. In this way, the continuum is instantaneously brought into an equilibrium state, causing the external BCs to immediately affect the atomistic region. The quasi-static continuum does, however, introduce two other issues. First, the quasi-static solution obviously suppresses all physical dynamics in the continuum (*e.g.*, there are no traveling waves in the continuum). This may be acceptable in those problems in which the dynamics in the continuum are neither of particular interest nor have a significant impact on the atomistic region. Second, as will be demonstrated, the quasi-static continuum generally increases unphysical wave reflection at the interface to the atomistic domain. This disturbs the atomistic dynamics and causes overheating of the atomistic region. This outcome is generally not acceptable.

It is evident that both dynamic and quasi-static continuum models have their own advantages and drawbacks, and the decision as to which one is more suitable is problem-specific. In this chapter, an approach which combines the advantages of both models, while removing the drawbacks, is presented. This novel approach is called the hybrid (dynamic and quasi-static) continuum model. The approach is based on the superposition of two complementary subproblems. One subproblem uses a quasi-static continuum model, and, the other, a dynamic continuum model. The basic idea is to apply the external BCs to the quasi-static subproblem and the internal BCs (which arise from the coupling to the atomistic region) to the dynamic subproblem. In doing so, the best aspects from both models are extracted. Applying the external BCs only to the quasi-static subproblem ensures that they take effect immediately on the atomistic region, even in large continuum regions. Applying the internal BCs only to the dynamic subproblem ensures low wave reflection and allows outwards propagating waves to exist in the continuum.

As the superposition property is limited to linear systems, the approach naturally is limited to dynamic methods that use a linear elastic continuum model. This is the case for the CLS method (Abraham *et al.*, 1998; Broughton *et al.*, 1999; Abraham *et al.*, 2000), the finite temperature CADD method (Qu *et al.*, 2005; Shiari, Miller, and Curtin, 2005) and the finite temperature BD method Anciaux, Ramisetti, and Molinari (2012), all of which were introduced in Section 3.1. It should also be highlighted that it is straightforward to exchange the continuum model in all atomistic-to-continuum methods as has been pointed out by Miller and Tadmor (2009). Therefore, if one of the currently static methods is recast into a dynamic version with a linear elastic continuum model, our approach is also applicable[1]. Our approach is, therefore, applicable in principle to all dynamic concurrent atomistic-to-continuum methods, as long as a linear elastic continuum is used. The approach is also suitable for the study of most problems with one important exception. As the external BCs are applied in a quasi-static manner, it is naturally not suitable for problems which explicitly require the external BCs to be applied dynamically (*e.g.*, to model inward traveling waves into the atomistic region). In this case, neither the hybrid nor the quasi-static continuum model is suitable and a dynamic continuum model must be used.

As discussed in Section 3.1, the three eligible methods (*i.e.*, CLS, finite temperature CADD, finite temperature BD) differ in their key characteristics. (i) The CLS and the finite temperature BD methods use an energy-based governing formulation, while the finite temperature CADD method is force-based. (ii) The CLS and the finite temperature

[1]This is exactly what has been done for the finite temperature version of the BD method (Anciaux, Ramisetti, and Molinari, 2012), where the non-linear Cauchy-Born continuum model, which was originally presented in the static BD method, was exchanged for a linear elastic model in the finite temperature version.

CADD methods use a sharp interface between the scales. In contrast, the finite temperature BD method uses a handshake region. (iii) In the CLS and finite temperature CADD methods, a strong degree of compatibility is enforced in the coupling BCs of the scales. In terms of the continuum, this means that the interface nodes move in step with the interface atoms. In the finite temperature BD method, on the other hand, a weak degree of compatibility is used, whereby the BCs are only enforced in an average manner.

In the description of the method, special focus will be laid on the application to the finite temperature CADD method (Qu *et al.*, 2005; Shiari, Miller, and Curtin, 2005)[2]. The application to the two other methods follows the same principles, but the different key characteristics of the methods make a unified presentation difficult. Still, guidance for the application of the approach to the other methods will be given and their similarities and differences will be highlighted.

6.2. Methods

6.2.1. The continuum region in the CADD method

The spatial decomposition of a solid body into continuum and atomistic regions, V and Ω, which is used in the CADD method, is shown in Fig. 6.1a. In CADD, the regions are separated by a sharp interface (*i.e.*, there is no handshake region).

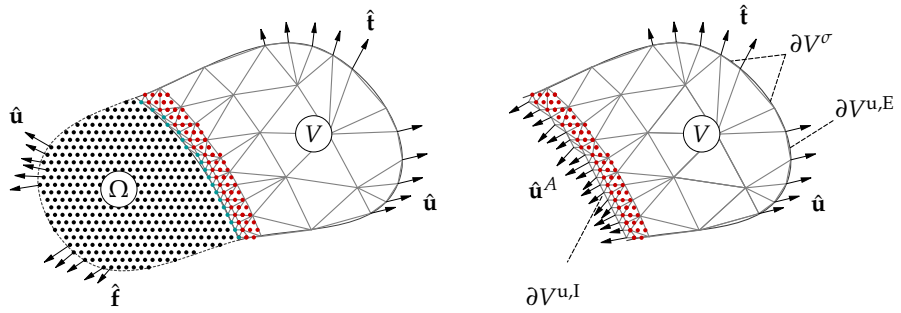

Fig. 6.1.: (a) The spatial decomposition used in the CADD method. The decomposition is the same for all other methods that do not use a handshake region, *e.g.*, the CLS method. (b) Continuum region. The continuum nodes on the internal (interface) boundaries $\partial V^{\mathrm{u,I}}$ are subject to displacement BCs using the atomic displacements $\mathbf{u}^{A}$. The continuum nodes on the external (non-interfacial) boundaries, $\partial V^{\mathrm{u,E}}$ and ∂V^{σ}, are subject to predefined displacements and tractions, respectively.

[2]In the following text, the finite temperature CADD method will simply be labeled as CADD.

The set closure $\overline{V}$ of the continuum region is the set union of the inner region and the boundary, *i.e.*, $\overline{V} = V \cup \partial V$ (see Fig. 6.1b). The boundary ∂V consists of non-intersecting displacement and traction boundaries, *i.e.*, $\partial V = \overline{\partial V^{\mathrm{u}}} \cup \overline{\partial V^{\sigma}}$, $\partial V^{\mathrm{u}} \cap \partial V^{\sigma} = \varnothing$, where $\varnothing$ is the empty set. Furthermore, it will be useful to distinguish between internal and external displacement boundaries $\partial V^{\mathrm{u}} = \partial V^{\mathrm{u,I}} \cup \partial V^{\mathrm{u,E}}$. Along the internal displacement boundaries $\partial V^{\mathrm{u,I}}$, the continuum region is coupled to the atomistic region. All other displacement boundaries are external.

CADD applies a strong compatibility coupling between the scales. The first characteristic of this coupling is that interface nodes, (*i.e.*, the nodes at the internal displacement boundaries $\partial V^{\mathrm{u,I}}$) move in step with the interface atoms. This is achieved through displacement BCs of the interface nodes using the atomic displacements $\hat{\mathbf{u}}^A$. This is the directional coupling from the atomistic region to the continuum. The coupling in the other direction (*i.e.*, from the continuum to the atomistic region) is solely achieved through the pad atom positions. The pad atoms strictly follow the deformation of the continuum, which is the second characteristic of the strong compatibility coupling.

Dynamic continuum model

In the continuum region, a dynamic or a quasi-static continuum model may be used. The standard approach, *i.e.*, the application of a dynamic continuum model, naturally ensures maximum compatibility between the scales and allows traveling waves to exist in the continuum. The strong form of the dynamic initial/boundary-value problem in the CADD method is

Find $u_i : \overline{V} \times [0, t^{\mathrm{e}}] \to \mathbb{R}$ such that

$$\rho \ddot{u}_i = \sigma_{ij,j} + \rho b_i \qquad \text{on } V \times]0, t^{\mathrm{e}}[\tag{6.1a}$$

$$u_i = \hat{u}_i^A \qquad \text{on } \partial V^{\mathrm{u,I}} \times]0, t^{\mathrm{e}}[\tag{6.1b}$$

$$u_i = \hat{u}_i \qquad \text{on } \partial V^{\mathrm{u,E}} \times]0, t^{\mathrm{e}}[\tag{6.1c}$$

$$\sigma_{ij} n_j = \hat{t}_i \qquad \text{on } \partial V^{\sigma} \times]0, t^{\mathrm{e}}[\tag{6.1d}$$

Initial conditions:

$$u_i(\mathbf{x}, 0) = u_i^0(\mathbf{x}) \quad \dot{u}_i(\mathbf{x}, 0) = \dot{u}_i^0(\mathbf{x}) \qquad \mathbf{x} \in V$$

where $[0, t^{\mathrm{e}}]$ is the time interval, $\hat{u}_i^A$ are the atomic displacements and $\hat{u}_i$ and $\hat{f}_i$ are prescribed functions along the boundary.

The problem is solved through temporal and spatial discretization with the given initial conditions. As discussed in Section 5.2.1, in the temporal discretization of the

continuum problem, the same time step is commonly used as in the atomistic model. The interface nodes are attached to the interface atoms at every time step, *i.e.*, $u_i = \hat{u}_i^A$.

As discussed above, studying large continuum regions may be problematic in a dynamic continuum model, as the external continuum BCs may take an exceedingly long time to advance to the atomistic region. And, related to this aspect, after a change in the BCs, the system may take long periods of time to reach a new state of equilibrium.

Quasi-static continuum model

Alternatively, a quasi-static continuum model may be used in which the continuum region is instantaneously brought into equilibrium at every discrete instant of continuum time. As long as the continuum dynamics are not of particular importance to the studied problem, the approach is attractive, as external continuum BCs immediately affect the atomistic region. And, related to this aspect, after a change occurs in the BCs, the instantaneous equilibrium in the continuum region allows the whole system to attain higher equilibration rates (*i.e.*, the targeted system's state of equilibrium is attained more rapidly). The strong form of the quasi-static initial/boundary-value problem is

Find $u_i : \overline{V} \times [0, t^{\mathrm{e}}] \to \mathbb{R}$ such that

$$0 = \sigma_{ij,j} + \rho b_i \qquad \text{on } V \times]0, t^{\mathrm{e}}[\tag{6.2a}$$

$$u_i = \frac{1}{\Delta t} \int_{t-\Delta t}^{t} \hat{u}_i^A \, d\tau \qquad \text{on } \partial V^{\mathrm{u,I}} \times]0, t^{\mathrm{e}}[\tag{6.2b}$$

$$u_i = \hat{u}_i \qquad \text{on } \partial V^{\mathrm{u,E}} \times]0, t^{\mathrm{e}}[\tag{6.2c}$$

$$\sigma_{ij} n_j = \hat{t}_i \qquad \text{on } \partial V^{\sigma} \times]0, t^{\mathrm{e}}[\tag{6.2d}$$

Initial conditions:

$$u_i(\mathbf{x}, 0) = u_i^0(\mathbf{x}) \qquad \mathbf{x} \in V$$

Like the dynamic problem, the quasi-static problem is solved through temporal and spatial discretization using the given initial conditions. The temporal discretization with time step Δt in the continuum is commonly, however, coarser than that which is used in the atomistic region. During a continuum time step, the displacements of the interface atoms are averaged, *i.e.*, $u_i = \frac{1}{\Delta t} \int_{t-\Delta t}^{t} \hat{u}_i^A \, d\tau$.

It will be shown in the example in Section 6.3.1 that the choice of the continuum time step Δt significantly affects the wave reflection behavior and is, therefore, critical to the accuracy of the model. It will also be shown that a quasi-static continuum generally increases unphysical wave reflection. Yet another critical point is that the quasi-static

approach naturally suppresses physical dynamics in the continuum (*e.g.*, there are no traveling waves in the continuum).

6.2.2. Hybrid continuum model

In order to combine the advantages of the dynamic and the quasi-static continuum model, while removing the drawbacks, the use of a hybrid (dynamic and quasi-static) continuum model is proposed. The approach is based on the superposition of a dynamic and a quasi-static subproblem (see Fig. 6.2) and, thus, limited to linear elastic continua. The strong form of the hybrid initial/boundary-value problem is[3]

Find $u_i^D, u_i^S : \overline{V} \times [0, t^e] \to \mathbb{R}$ such that

$$\rho \ddot{u}_i^D = \sigma_{ij,j}^D + \rho b_i^D \qquad 0 = \sigma_{ij,j}^S + \rho b_i^S \qquad \text{on } V \times]0, t^e[\tag{6.3a}$$

$$u_i^D = \hat{u}_i^A \qquad u_i^S = 0 \qquad \text{on } \partial V^{u,I} \times]0, t^e[\tag{6.3b}$$

$$u_i^D = 0 \qquad u_i^S = \hat{u}_i \qquad \text{on } \partial V^{u,E} \times]0, t^e[\tag{6.3c}$$

$$\sigma_{ij}^D n_j = 0 \qquad \sigma_{ij}^S n_j = \hat{t}_i \qquad \text{on } \partial V^{\sigma} \times]0, t^e[\tag{6.3d}$$

Initial conditions:

$$u_i^D(\mathbf{x}, 0) = u_i^0(\mathbf{x}) \qquad u_i^S(\mathbf{x}, 0) = 0 \qquad \mathbf{x} \in V$$

$$\dot{u}_i^D(\mathbf{x}, 0) = \dot{u}_i^0(\mathbf{x}) \qquad \mathbf{x} \in V$$

Both subproblems are solved through temporal and spatial discretization using the given initial conditions. As can be seen in Eqs. 6.3b, 6.3c and 6.3d, the BCs of the dynamic and quasi-static continuum models are complementary (see Fig. 6.2). The partitioning of the body force term in 6.3a into $\rho \mathbf{b}^D$ and $\rho \mathbf{b}^S$ requires some further discussion. Body forces, which are constant (*e.g.* due to gravity) or slowly varying over time, can be arbitrarily partitioned between the two subproblems. Due to the superposition principle the constant influence in time of such a load can either enter the dynamic or static equations. Body forces which are significantly varying over time (*e.g.* due to rapidly varying magnetic fields) should be fully assigned to the dynamic subproblem, due to its usually higher temporal resolution. This partitioning was however not further explored, as body forces are assumed to be negligible in all of the examples presented below.

The solution to the hybrid initial/boundary-value problem is found by the superposition of the dynamic and quasi-static partial solutions $u_i = u_i^D + u_i^S$ on $\overline{V} \times [0, t^e]$. The pad atom positions, which reveal the directional coupling from the continuum to

[3]The superscripts S and D are used to denote quantities in the quasi-static and dynamic subproblem, respectively.

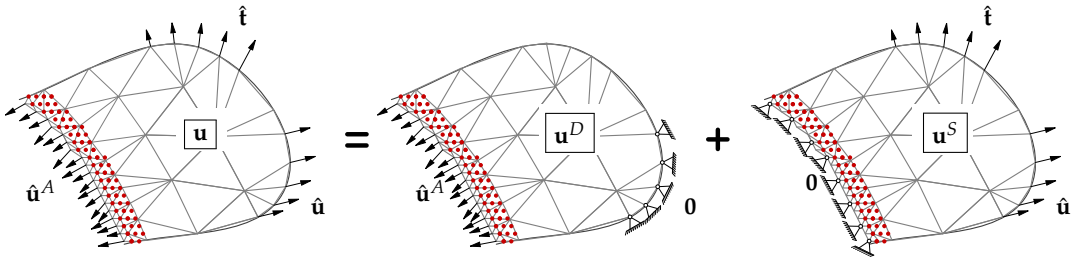

Fig. 6.2.: The two complementary subproblems used in the hybrid approach. The dynamic and the quasi-static subproblems yield $\mathbf{u}^D$ and $\mathbf{u}^S$, respectively.

the atomistic region, are updated using this superposed solution. The stresses in the hybrid model are also found by the superposition of the stresses in the dynamic and quasi-static subproblems, *i.e.*, $\sigma_{ij} = \sigma_{ij}^D + \sigma_{ij}^S$ on $\overline{V} \times [0, t^e]$.

Fig. 6.3 illustrates the interplay between the continuum and the atomistic region for the dynamic, quasi-static and hybrid continuum models, respectively.

As can be seen in Fig. 6.3c, the dynamic subproblem uses the atomistic time step $\Delta\tau$. In the quasi-static subproblem, a larger time step Δt is usually used for computational efficiency. It can also be seen that the two subproblems do not interact with each other and are thus independent. The dynamic subproblem solely interacts with the atomistic problem and vice versa (see Fig. 6.2). On the other hand, the quasi-static subproblem influences the atomistic problem but not vice versa. The quasi-static subproblem only depends on the prescribed external BCs (see Fig. 6.2). This also allows researchers to comfortably compute the solution of the quasi-static subproblem prior to running the actual simulation in a preprocessing step.

Although the hybrid continuum approach is readily applicable to other methods, the description and the equations presented were based on the CADD method. The different key characteristics of other methods may lead to different equations. The possible differences in the application to two other eligible methods, namely the CLS and the dynamic BD method, will now be described.

The CLS method and the CADD method share many common key characteristics. Just like CADD, CLS also does not use a handshake region and employs strong compatibility coupling between the scales. A major difference between the two methods is that CLS is an energy-based approach, while CADD is force-based. Although this causes a significant difference in how the atomistic regions are treated in the two methods, it has no impact on the continuum. Therefore, the current presentation of our approach can be applied without altering to the CLS method.

The key characteristics of the dynamic BD method, on the other hand, are diametrically

opposed to those of the dynamic CADD method. It is an energy-based method that uses a handshake region and employs weak compatibility coupling between the scales. The mixing of the continuum and atomistic models in the handshake region, which is part of the continuum domain V, affects the balance equations of linear momentum (Eqs. 6.1a, 6.2a and 6.3a). The weak compatibility coupling affects both the equations for the BCs along the internal displacement boundary (Eqs. 6.1b, 6.2b and 6.3b) and the balance of linear momentum (Eqs. 6.1a, 6.2a and 6.3a), the latter by applying additional forces on the nodes in the handshake region. The hybrid continuum approach is in principally applicable to the dynamic BD method. However, a detailed investigation of the application is not within the scope of this work and is left for future research.

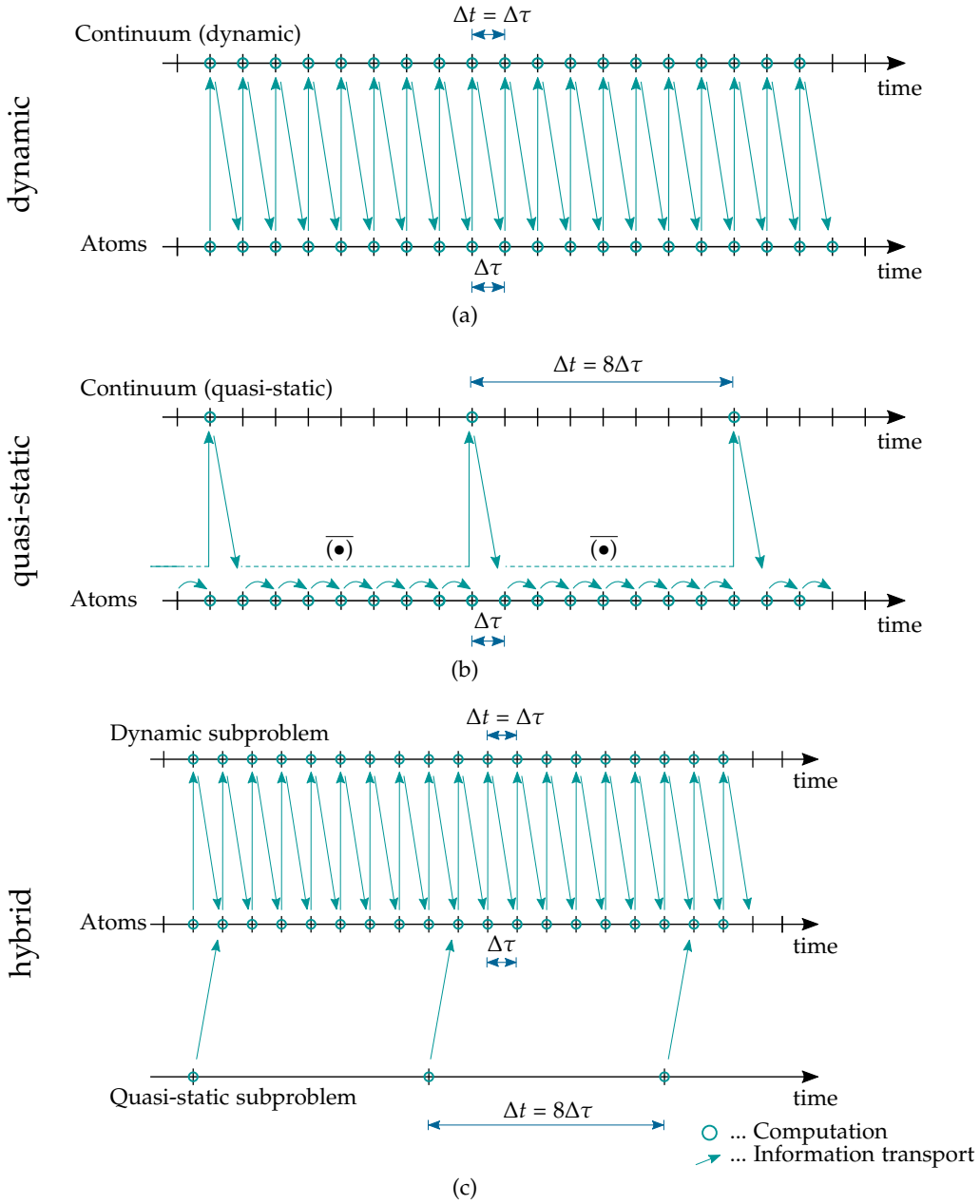

Fig. 6.3.: Interplay between the scales in the CADD method with (a) the dynamic continuum model, (b) the quasi-static continuum model and (c) the hybrid continuum model. The $\overline{(\bullet)}$ symbol represents the time average of the atomic quantities relevant to the continuum. In case of the CADD method, these quantities are the displacements of the interface atoms.

6.3. Numerical examples

In this section, three numerical examples will be presented. The purpose of the first two examples is to highlight the advantages and drawbacks of the dynamic and quasi-static continuum models and to compare the performance of the hybrid continuum model with both. The third example is a practical example, namely, a 2D tensile test, for which the dynamic and quasi-static models are expected to yield comparable results. It will be shown that the results of the hybrid continuum model agree very well.

Aluminium is the material of interest in all examples, and the EAM potential (see Section 2.2.4) as given by Zhou, Johnson, and Wadley (2004) is used as the interatomic potential. A cut-off radius of 6.404 Å is applied (see NIST, 2020).

The details of the discretization of the course scale and time integration of the equations of motion are identical to Section 5.3. As in Section 5.3, the anisotropic elastic constants and mass densities of the continuum as well as the equilibrium lattice spacings at the studied temperatures are found by separate MD simulations using the given interatomic potential.

6.3.1. (Quasi-)2D pulse reflection

In this example, the reflection of pulses at the interface will be studied for the dynamic, quasi-static and hybrid continuum models. The two-dimensional geometry used and the BCs of the system are shown in Fig. 6.4. Longitudinal pulses will be introduced, which travel in horizontal direction (*i.e.*, in the direction of the x-axis), from the atomistic region into the continuum. Therefore, essentially one-dimensional pulse propagation is studied using a 2D geometry (hence, the problem is quasi-2d).

The material studied is hexagonal aluminum with the c-axis aligned normal to the x, y-plane. Two different lattice orientations are used by aligning the x-axis with the $[11\bar{2}0]$- and $[\bar{1}100]$-directions, respectively, which corresponds to a 90° rotation (see Fig. 6.4).

For the given external continuum BCs in this example, the dynamic and the hybrid continuum models coincide. This is because there are no external traction BCs on the continuum, and the external displacement BCs dictate zero displacement, which leads to zero displacements in the quasi-static subproblem when combined. The solution only consists of the dynamic subsolution, which is equal to the solution of the dynamic continuum model.

The right end of the atomistic domain is used to introduce the longitudinal pulses in the horizontal direction. To this end, the motion of six layers of atoms on the far right-hand

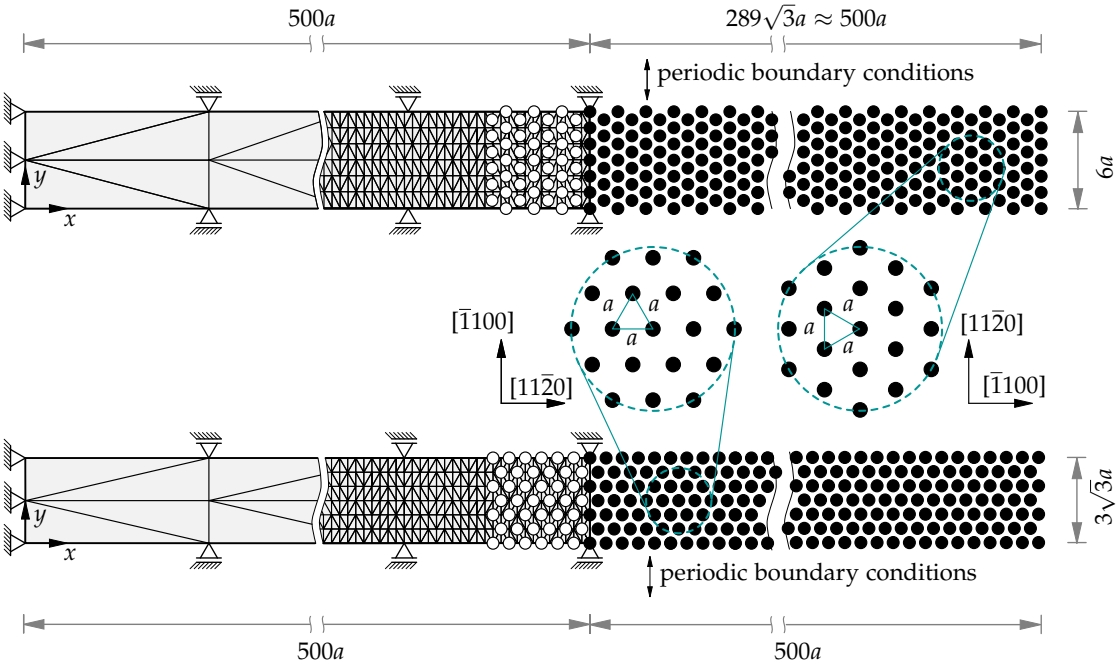

Fig. 6.4.: Geometry and BCs used in the quasi-2D pulse reflection example. a is the equilibrium lattice distance.

side is controlled. In principle, any type of pulse may be introduced; however, pulses of the form

$$\hat{u}(x,t) = -A\exp(-\alpha(kx-\omega t)^2)\cos(kx-\omega t) \tag{6.4}$$

are used, where $\hat{u}(x,t)$ is the horizontal displacement. A, k and ω are the amplitude, wave number and frequency of the pulse, respectively, and α is a parameter which controls the spatial extent of the pulse. This type of pulse provides a relatively sharp frequency spectrum with a small spatial extent (exemplary pulses are shown in Fig. 6.5). Moderate values for the amplitude of $A = 1/4a$ are used, where a is the equilibrium lattice spacing.

The pulses travel through the atomistic region until they reach the interface, where parts of the pulses are reflected. Ultimately, we are interested in the reflection coefficient R, which is the ratio of the reflected amplitude to the incoming amplitude A. To quantify the magnitude of the reflected amplitude, the horizontal atomic displacements after reflection is tracked. In the optimal case, the reflected amplitude is only a few percent of the incoming amplitude. This implies that it will be much smaller than the thermal fluctuations of the atoms at reasonable temperatures. To keep the reflected amplitude from getting lost in the thermal noise, the thermal fluctuations are kept at a minimum by studying the system at an initial temperature of 10^{-3} K. This limits the

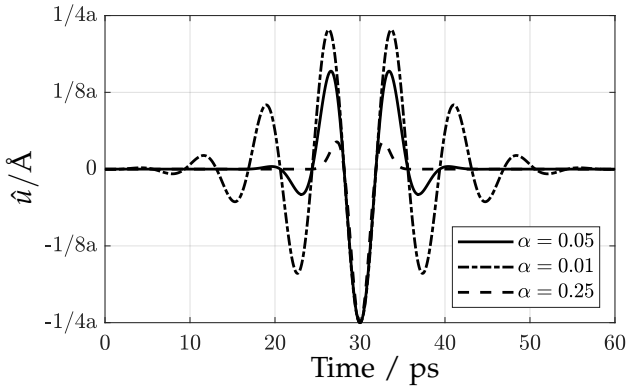

Fig. 6.5.: Exemplary pulses of frequency $\omega = 8.38 \times 10^{11}$ Hz and amplitude $A = 1/4a$ for different values of the parameter α. The pulses are shown as a function of time at a fixed position x. A value of $\alpha = 0.05$ (solid line) is used for all three pulses.

amount of error for the reflection coefficient caused by the thermal fluctuations to less than 0.5 percentage points. In addition, no thermostat is included in this example to solely compare the reflection caused by the different continuum models. The common approach applied in the CADD method is to use a Langevin thermostat in the near-interface atomistic region to control the temperature. However, in contrast to the following numerical examples, a thermostat is omitted here, as it was found that the Langevin thermostat itself is also a source of reflection.[4]

The simulations are carried out as follows: first, the system is equilibrated at 10^{-3} K for 20 ps (with an equilibrium lattice spacing of $a = 2.6485$ Å). After equilibration, three pulses of varying frequency are introduced and the reflection coefficient for the dynamic/hybrid and the quasi-static continuum models are evaluated. The pulses used have frequencies (and periods) of $\omega^1 = 2.51 \times 10^{12}$ Hz ($t^1 = 2500\Delta\tau$), $\omega^2 = 1.26 \times 10^{12}$ Hz ($t^2 = 5000\Delta\tau$) and $\omega^3 = 8.38 \times 10^{11}$ Hz ($t^3 = 7500\Delta\tau$). In the quasi-static continuum model, different values of the time step Δt (multiples of $\Delta\tau$) are used to show the influence on the reflection behavior. The results are shown in Fig. 6.6 and Fig. 6.7.

The dynamic continuum model yields lower amounts of wave reflection due to the consistent dynamical coupling, as expected. The hybrid continuum model, which here coincides with the dynamic continuum model, retains this low wave reflection behavior. The quasi-static continuum model generally leads to increased wave reflection, and its reflection behavior depends significantly on the continuum time step Δt. The optimal

[4]This is because of the random forces, which act on the thermostatted atoms in the Langevin thermostat. These forces slightly perturb the dynamics of the atoms, which leads to unphysical reflection.

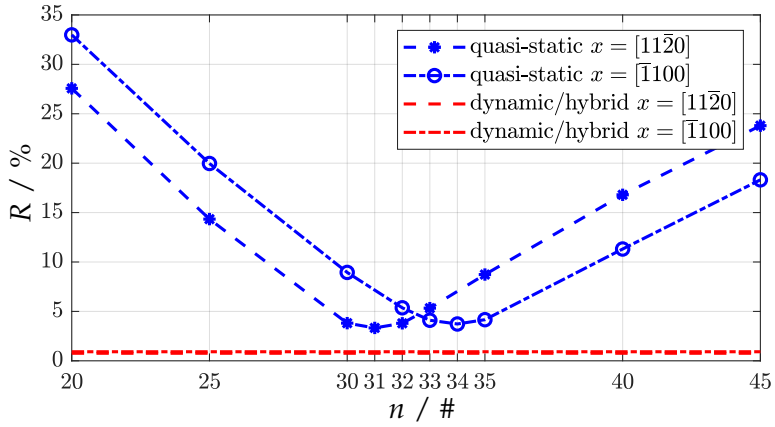

Fig. 6.6.: Average reflection coefficient R of the continuum models for the two lattice directions over the three studied pulses, with $\Delta t = n\Delta\tau$.

value of Δt in terms of wave reflection also clearly depends on the pulse direction in the lattice, *i.e.*, the wave vector. Deviations from the optimal Δt value result in higher wave reflection. This behavior can be explained as follows: as Δt increases, the continuum becomes stiffer and eventually, as $\Delta t \to \infty$, the continuum and thus the pad atoms are permanently locked in place. This is the limit of extreme stiffness, in which the continuum causes the atoms to experience a rigid wall BC. On the other hand, as Δt decreases, the continuum becomes softer. At the limit of extreme softness, $\Delta t \to 0$, the quasi-static continuum can be imagined as being dynamic with zero mass and thus zero inertia. These two extreme cases are illustrated for a simple, one-dimensional chain of atoms in Appendix A. The time step which resembles the real system lies somewhere in between these two extremes. In case of the x-axis being equal to the $[11\bar{2}0]$ or the $[\bar{1}100]$-direction, this time step is about $\Delta t = 31\Delta\tau$ or $\Delta t = 34\Delta\tau$, respectively.

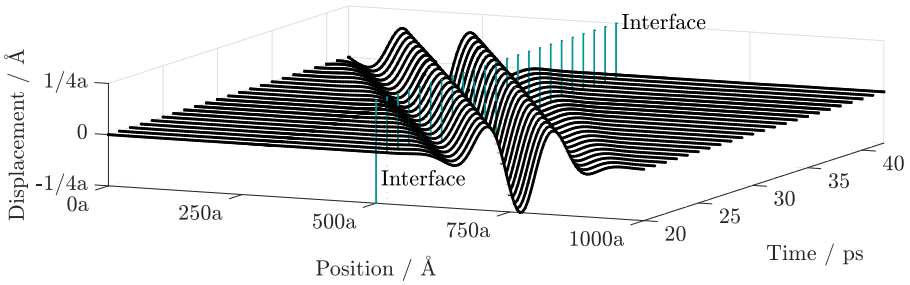

(a) dynamic/hybrid, $R = 0.60\%$

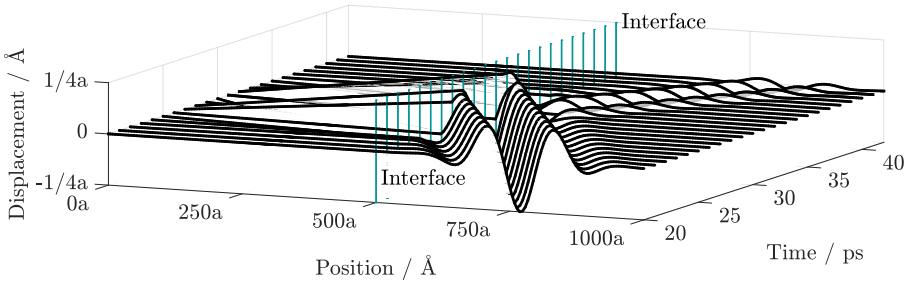

(b) quasi-static $\Delta t = 25\Delta\tau$, $R = 15.39\%$

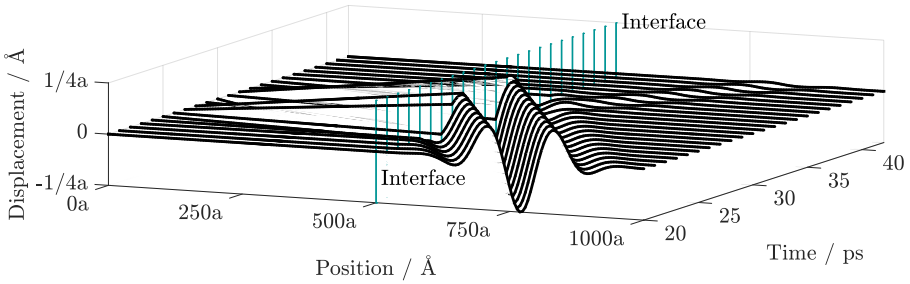

(c) quasi-static $\Delta t = 30\Delta\tau$, $R = 3.74\%$

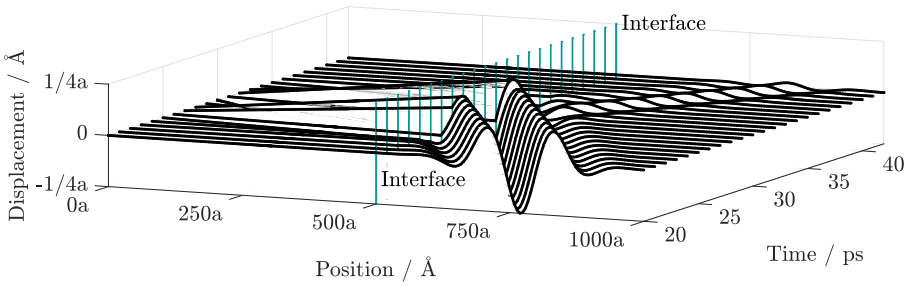

(d) quasi-static $\Delta t = 35\Delta\tau$, $R = 9.38\%$

Fig. 6.7.: Exemplary visualization of the propagation of pulse 2 ($\omega^2 = 1.26 \times 10^{12}$ Hz, $t^2 = 5000\Delta\tau$) for the x-axis coinciding with the $[11\bar{2}0]$-direction. For the dynamic/hybrid continuum model, the pulse propagates over the interface with minimal reflection. For the quasi-static continuum model, the reflection is higher and depends significantly on the continuum time step Δt.

6.3.2. Equilibration rate

When large continuum regions are to be treated in a dynamic continuum model, the time needed for a change in the external BCs to reach the atomistic region may become prohibitively long. This is because of the time limitations of molecular dynamics. If it is assumed that the simulation time for a practical system is limited to the range of nanoseconds, a continuum region in the size of micrometers can already be large enough to exceed the computational limitations. Also, related to this aspect, the system may take an exceedingly long time to reach a new equilibrium state, after the continuum BCs have changed. To avoid these issues, a quasi-static continuum model presents an attractive alternative, as long as the dynamics in the continuum region are not important. In the quasi-static continuum model, equilibrium in the continuum is enforced at each continuum time step. Therefore, the atoms immediately experience changes in the external continuum BCs, and new equilibrium states of the total system can be reached more rapidly.

The purpose of this example is to illustrate the difference among the equilibration rates for the dynamic, quasi-static and the hybrid continuum models. The same geometry and material as in the last example are used. In contrast, the right-hand end of the atomistic region is clamped by fixing the position of six layers of atoms, as shown in Fig. 6.8. As the orientation in the atomistic region is not important in this example, the x-axis is arbitrarily aligned with the $[11\bar{2}0]$-direction. Also, the system is now studied at a temperature of 100 K, with an equilibrium lattice spacing of $a = 2.6498$ Å. After equilibrating the system for 20 ps at 100 K, a compression of 1% ($10a$) is applied via displacement BCs on the left-hand edge of the continuum with three different strain rates $\dot{\varepsilon}^1 = 2.75 \times 10^8\,\mathrm{s}^{-1}$, $\dot{\varepsilon}^2 = 8.25 \times 10^8\,\mathrm{s}^{-1}$ and $\dot{\varepsilon}^3 = 2.475 \times 10^9\,\mathrm{s}^{-1}$.

In this example, a Langevin thermostat is applied in the atomistic region to the first two layers of atoms near the interface, to control the temperature. In addition to controlling the temperature, the Langevin thermostat also provides the system with dynamic stability at elevated temperatures due to its inherent damping abilities (Junge, Anciaux, and Molinari, 2015). Like this damping in the atomistic vicinity of the interface, it was also found that some, although smaller, amount of damping is needed in the continuum vicinity of the interface to ensure dynamic stability. To this end, a mass proportional damping is applied in the region of the pad atoms with a damping coefficient of $1/10$ of the chosen Langevin thermostat damping coefficient $\gamma = 2.5 \times 10^{13}\,\mathrm{s}^{-1}$. The continuum damping is applied in the dynamic continuum model and the dynamic subproblem of the hybrid continuum model.

The atoms in the compressed system will be distributed according to a linear displacement field. The deviation from the compressed equilibrium state in the atomistic region

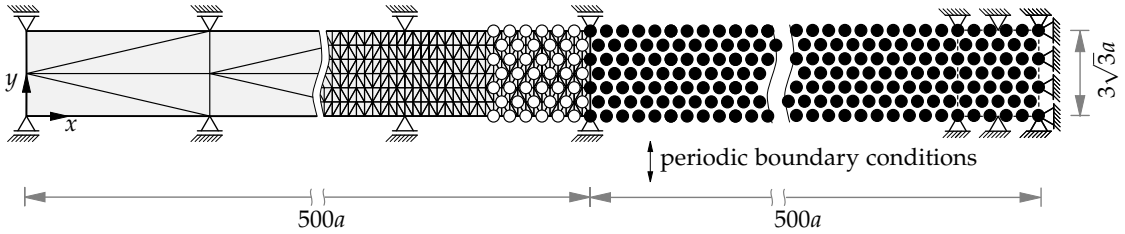

Fig. 6.8.: Geometry and BCs used in the equilibration rate example.

is quantified using the root-mean-square deviation (RMSD)

$$\text{RMSD} = \sqrt{\frac{\sum_{i=1}^{N} (u_i^A - \tilde{u}_i^A)^2}{N}} \tag{6.5}$$

of the horizontal atomic displacements $\mathbf{u}^A$ from the known linear target displacement field $\tilde{\mathbf{u}}^A$. Here, N is the total number of atoms in the atomistic region. Fig. 6.9 shows the RMSD over time for the three strain rates and the three continuum models. The strain rate $\dot{\varepsilon}_1$ is low enough, such that dynamic effects in the continuum are negligible. Thus, the dynamic and quasi-static continuum models show a similar decline in the RMSD (see also Fig. 6.10). The hybrid continuum model follows the same behavior. In the case of the two higher strain rates $\dot{\varepsilon}^2$ and $\dot{\varepsilon}^3$, dynamic effects are no longer negligible. The higher the strain rate, the longer it takes the system with the dynamic continuum model to reach an equilibrium state. The quasi-static and hybrid continuum models, on the other hand, reach equilibrium much faster (see also Fig. 6.11 and Fig. 6.12). In all scenarios, the quasi-static continuum model responds more quickly than the dynamic continuum model to the external change of the BCs, but continues to behave in a rather sluggish manner. The dynamic continuum model, on the other hand, affects the atomistic region abruptly, when the deformation reaches the interface. This is followed by a period of rather volatile behavior in the atomistic region. Depending on the strain rate, either one or the other manner may be favorable. The hybrid continuum model combines both qualities in terms of its performance in this problem setting.

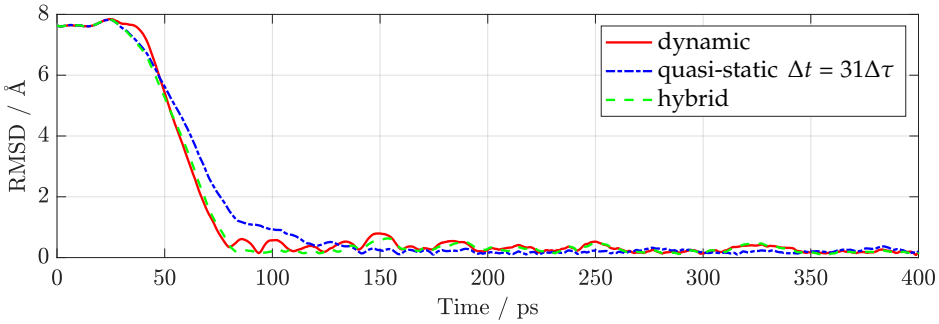

(a) $\dot{\varepsilon}^1 = 2.75 \times 10^8 \mathrm{s}^{-1}$

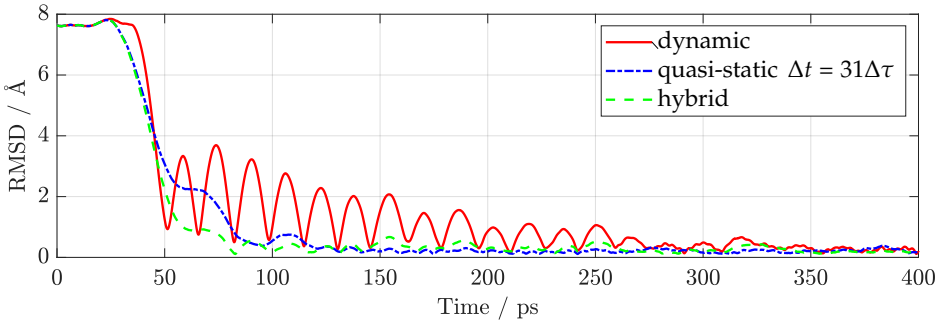

(b) $\dot{\varepsilon}^2 = 8.25 \times 10^8 \mathrm{s}^{-1}$

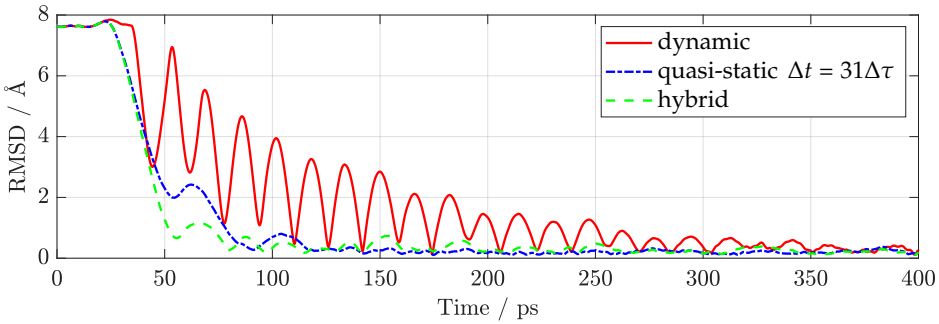

(c) $\dot{\varepsilon}^3 = 2.475 \times 10^9 \mathrm{s}^{-1}$

Fig. 6.9.: Root-mean-square deviation (RMSD) from the target displacement field over time for the different continuum models at different strain rates.

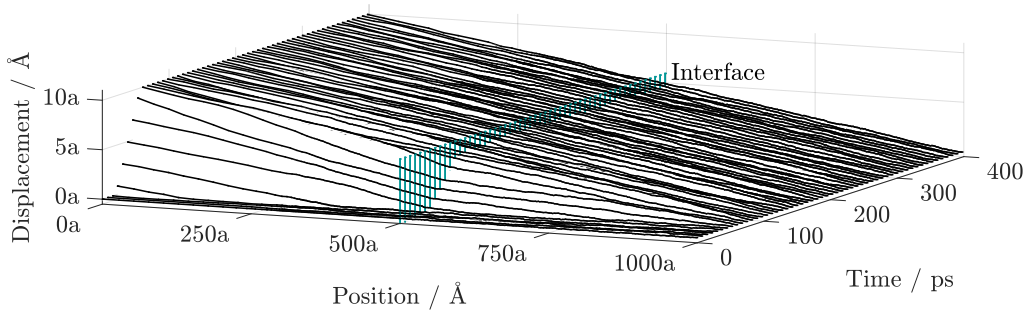

(a) dynamic

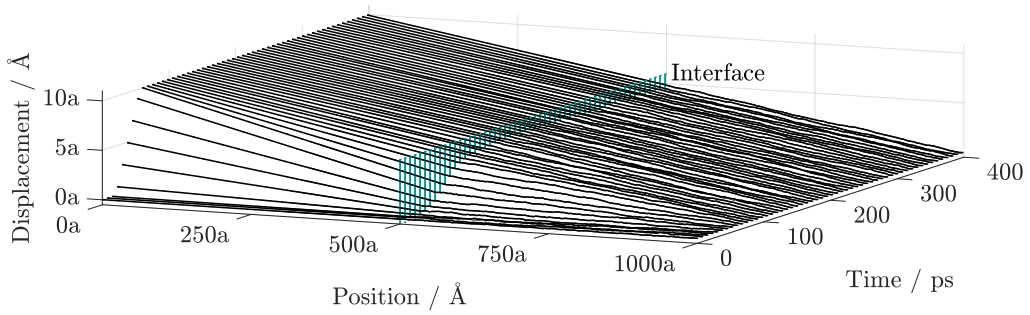

(b) quasi-static $\Delta t = 31\Delta\tau$

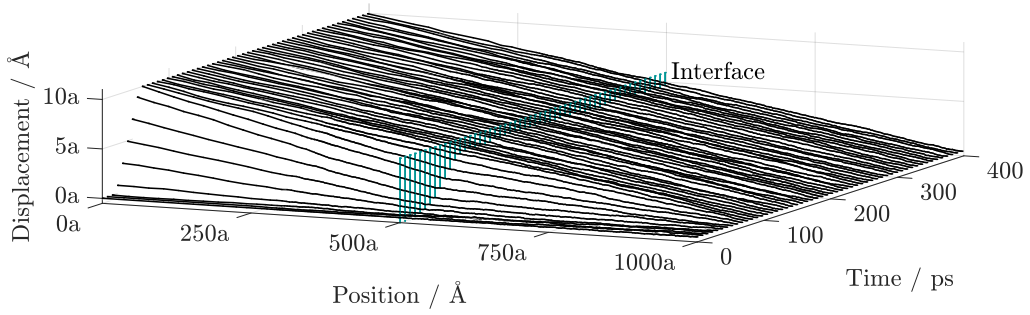

(c) hybrid

Fig. 6.10.: Exemplary comparison of the horizontal displacement over time for the dynamic (a), quasi-static (b) and hybrid (c) continuum models for $\dot{\varepsilon} = 2.75 \times 10^8\,\mathrm{s}^{-1}$.

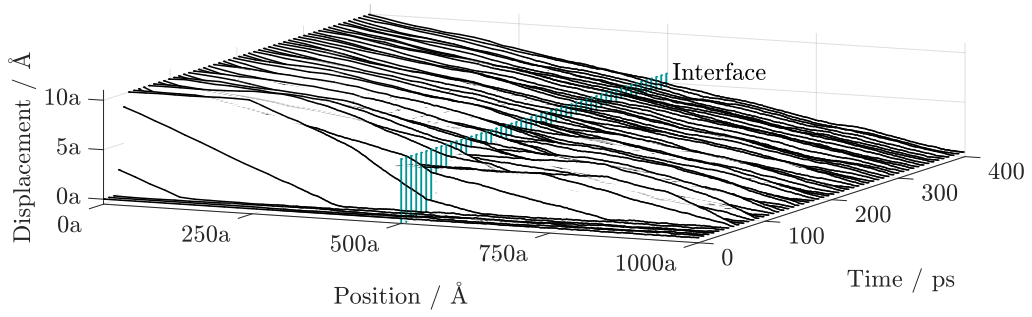

(a) dynamic

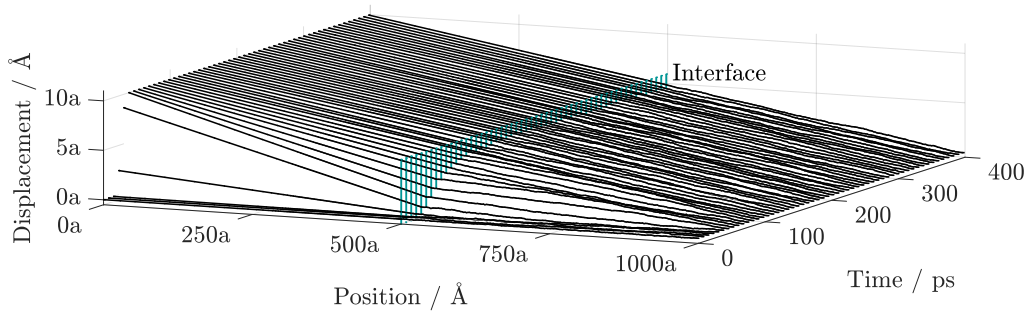

(b) quasi-static $\Delta t = 31\Delta\tau$

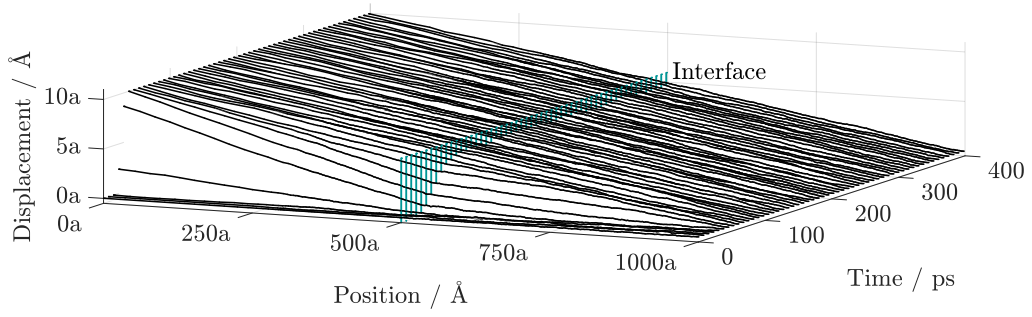

(c) hybrid

Fig. 6.11.: Exemplary comparison of the horizontal displacement over time for the dynamic (a), quasi-static (b) and hybrid (c) continuum models for $\dot{\varepsilon} = 8.25 \times 10^8\,\mathrm{s}^{-1}$.

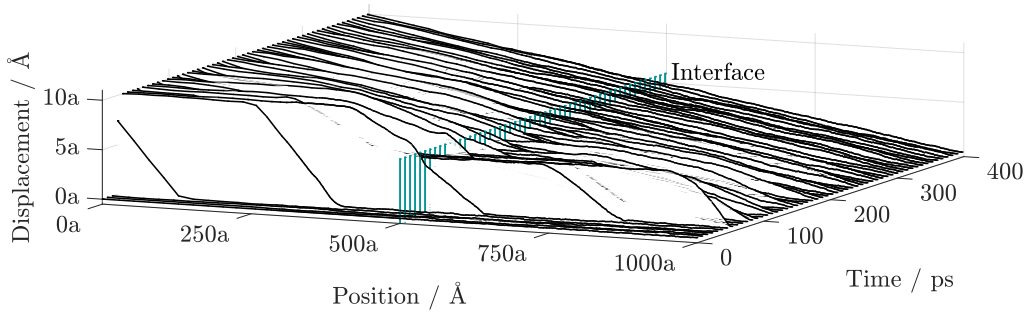

(a) dynamic

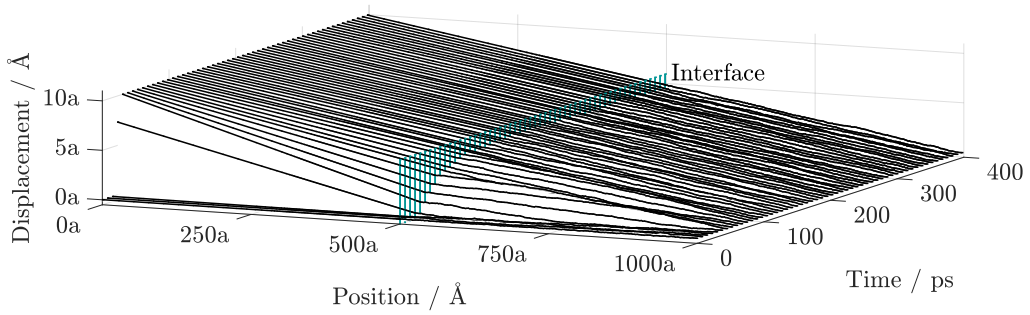

(b) quasi-static $\Delta t = 31\Delta\tau$

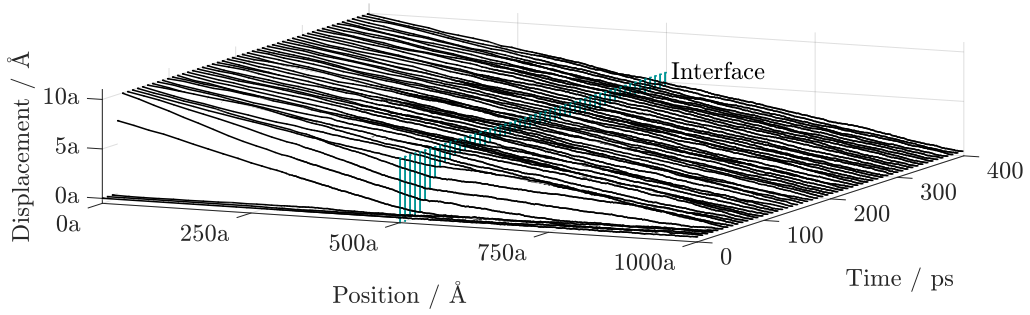

(c) hybrid

Fig. 6.12.: Exemplary comparison of the horizontal displacement over time for the dynamic (a), quasi-static (b) and hybrid (c) continuum models for $\dot{\varepsilon} = 2.475 \times 10^9\,\mathrm{s}^{-1}$.

6.3.3. Tensile tests of a 2D nanowire

Uniaxial tensile tests of a 2D nanowire are performed using the dynamic, quasi-static and hybrid continuum models. The tensile specimen is shown in Fig. 6.13. The same material is used as in the previous examples, and the x-axis is again aligned with the $[11\bar{2}0]$-direction of the material. The stress-strain curves of the material are studied at temperatures of 50 K, 150 K and 250 K, with equilibrium lattice spacings of $a = 2.6491$ Å, $a = 2.6507$ Å and $a = 2.6530$ Å, respectively. As in the last example, a Langevin thermostat is applied to the first two layers of atoms near the interface. Also, a damping in the pad atom region of the continuum is applied in the dynamic continuum model and the dynamic subproblem of the hybrid continuum model.

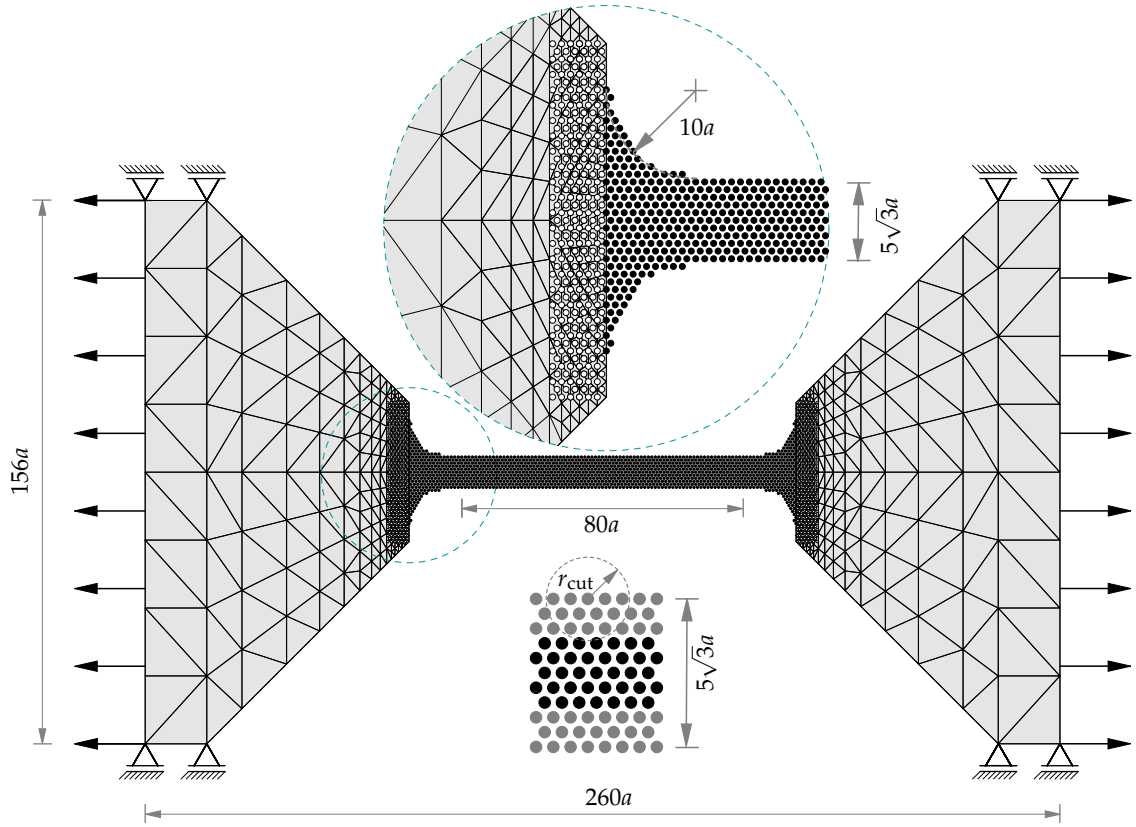

Fig. 6.13.: Geometry and BCs used in the uniaxial tensile test example.

The tensile tests are carried out as follows: first, the system is equilibrated for 40 ps. After equilibration, the uniaxial tensile loading is applied via displacement BCs along the outer edges of the continuum regions. A strain rate of $\dot{\varepsilon} = 2.75 \times 10^8\,\mathrm{s}^{-1}$ is used, which is comparable to rates cited in related work in the literature (Ju, Lin, and Lee,

2004; Xu and Chen, 2019). It was verified that the chosen strain rate is small enough, such that dynamic effects in the continuum are negligible (see Section 6.3.2). Thus, the dynamic and the quasi-static continuum model are expected to yield comparable results. As done in comparable works, all tests were performed $n = 10$ times, using different but equivalent initial configurations, to achieve reasonable statistical sampling. The different initial configurations are obtained by assigning different random initial velocities to the atoms.

During the tensile tests, the stress is measured in the middle part of the atomistic region with an initial length of $80a$ (see Fig. 6.13). As a stress measure, the virial stress given by (see, *e.g.*, Tadmor and Miller, 2011)

$$\sigma_{ij} = \frac{1}{\Omega^\sigma} \sum_{\alpha=1}^{N} \left(-m^\alpha (v_i^\alpha - \tilde{v}_i)(v_j^\alpha - \tilde{v}_j) + \frac{1}{2} \sum_{\beta \neq \alpha}^{N} (x_i^\beta - x_i^\alpha) f_j^{\alpha\beta} \right) \tag{6.6}$$

is used, where Ω^σ is the volume of the atomistic region of interest, α and β are atoms, i and j are spatial directions, N is the number of atoms in the volume, v_i^α is the i-th component of the velocity of atom α, $\tilde{v}_i$ is the i-th component of the average velocity, x_i^α is the i-th component of the position of atom α and $f_j^{\alpha\beta}$ is the j-th component of the force on atom α applied by atom β. As a two-dimensional geometry is used, the volume V is reduced to an area A. Hence, the computed stresses have the dimension of force per length. To minimize the influence of known surface effects of the virial stress (see, *e.g.*, Zimmerman *et al.*, 2004), the atoms in a distance of one cut-off radius $r^{\text{cut}} = 6.404\,\text{Å}$ from the surface are not included in the stress evaluation (see Fig. 6.13).

As a strain measure, the engineering strain $\varepsilon = \frac{\Delta L}{L_0}$ is used, where L_0 equals the initial length of the atomistic region after equilibration and ΔL is the change in length of the atomistic region. Hence, the resulting stress-strain curves shown in Fig. 6.14 are (true) stress - (engineering) strain curves.

The stress-strain curves are pictured in Fig. 6.14. The dynamic continuum, the quasi-static continuum and the hybrid continuum model show very similar results up until the highest observed stress value (point of fracture). As expected, the obtained curves are strongly dependent on temperature. While the slope of the curve changes marginally, the stresses and strains at fracture clearly decrease as the temperature increases.

Different initial configurations do not have much influence on the pre-fracture part of the stress-strain curve (up until the highest observed stress levels). However, they significantly affect the stress-strain curve after this point. By using different, yet equivalent, initial configurations, the trajectories of microstates of the system in the phase space that is accessible to the ensemble are followed, each of which displays slightly different fracture behavior. Depending on the initial configuration, the fracture may

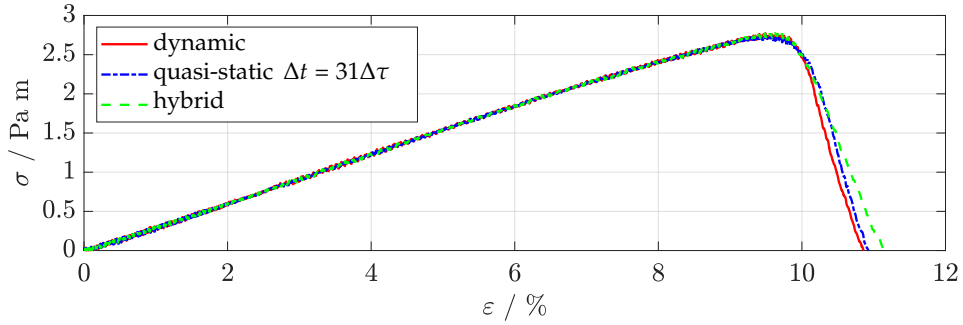

(a) $T = 50\,\mathrm{K}$

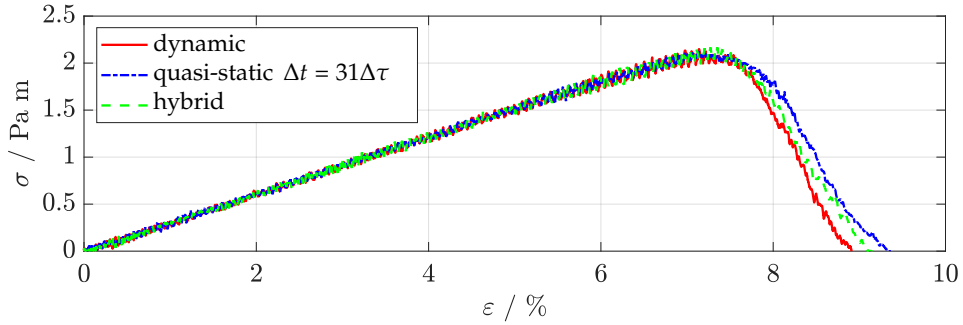

(b) $T = 150\,\mathrm{K}$

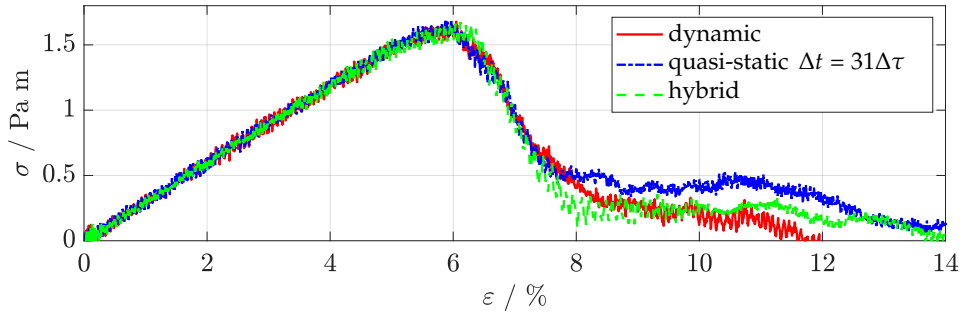

(c) $T = 250\,\mathrm{K}$

Fig. 6.14.: Stress-strain curves of the 2D aluminum nanowire at different temperatures for the dynamic, quasi-static and hybrid continuum model. The quantity σ gives the non-zero virial stress component in the uniaxial tensile test.

either occur rather in a localized and rapid manner, leading to a rapid drop in stress, or in a non-localized manner, with distributed plastic deformation and an associated slower stress decay rate. The correct statistical ensemble average can only be found

by averaging over $n \to \infty$ different initial configurations. For $n = 10$, the statistical averaging is not optimal, which explains the slight differences seen in the stress-strain curves in the three continuum models, but it is still reasonable. Overall, the results agree very well, and it is expected that the curves fully converge for $n \to \infty$.

7. Conclusion

This thesis presents an attempt towards the long term endeavor of taking atomistic-to-continuum multiscale methods beyond the purely academic realm to take the next big step of industrial adoption. One obstacle towards this goal is found in the large computational burden associated with these methods, hence approaches to increase the efficiency are needed in order to make these methods accessible to a wider range of users. The thesis is a collection of three such approaches, which promise substantial computational savings. All three approaches are general in the sense that they are readily applicable to a many atomistic-to-continuum multiscale models. The approaches have little limitations (see below), and thus are useful for studying a wide range of problems. Furthermore, the approaches can rather easily be implemented into existing codebases and have little computational overhead. A summary of the three approaches (presented in Chaps. 4 to 6) shall be given here.

In Chapter 4, similarities between the Newton-Raphson iteration scheme commonly used to solve the macroscopic equations in a hierarchical atomistic-to-continuum method and adaptive schemes from the field of stochastic approximation were revealed. Based on this finding, the application of standard averaging approaches from stochastic approximation to the hierarchical method was proposed in order to diminish the negative influence of noisy microscopic information on the computations of the macroscale. The noisy microscopic information results from an improper sampling of the microscale. This problem is commonly encountered in practical applications, where a sufficient sampling is often not feasible due to immense computational cost of the microscale computations.
It was shown in three numerical examples that the use of the two approaches "averaging of the iterates" and "averaging of the iterates and observations" leads to faster convergence of the solution fields, *i.e.*, the macroscopic displacement and stress distributions. The approach was also compared to a reference case, where only well-converged (noise-free) microscopic information was used. It was shown that in this case, the two approaches are able to achieve the same quality of results at a fraction of the computational cost.
As the application of these methods does not introduce any noteworthy additional computational burden (the displacement and stress fields of the most recent macroscopic iterations need to be stored), the consideration of these methods in hierarchical

atomistic-to-continuum models at finite temperature is highly advocated.

In Chapter 5, a method to couple the scales in concurrent atomistic-to-continuum models based on current demand by application to the finite temperature version of the CADD method was carefully described.
The focus was laid on the application of the presented algorithm to a version of the CADD method that uses a dynamic finite element formulation and couples the scales in every instant of fine-scale time. The application to a quasi-static continuum with less frequent coupling of the scales is readily possible, but has not been described in detail.
The presented algorithm is stable in the sense that false positives do not have a negative impact on the simulation. In the case of a false positive, the continuum solution fields in the model at hand are computed as inherent to the model, causing only unnecessary computational effort, but no further disadvantages.
The algorithmic detection of deformation was achieved by using a simple, yet effective, deformation measure as presented in Section 5.2.3. The application of more sophisticated deformation measures, *e.g.*, using invariants of the Green-Lagrange strain tensor as proposed by Tadmor, Ortiz, and Phillips (1996), is possible.
It was shown that the computational cost of the algorithm is low and a number of measures to minimize cost were presented. The low cost is convenient for those problems in which the continuum solution is always demanded over the course of the simulation. This is caused by ongoing deformation at the coupling interface or ongoing changes in the external (non-interfacial) boundary conditions of the continuum. In these cases, the application of the algorithm is redundant. However, due to the low cost of the algorithm, this additional effort is mostly negligible.
Due to the altered dynamics in the continuum, the application of the algorithm is limited to problems in which accurate continuum dynamics are not of significant importance. Caution must also be taken if the continuum region contains large, *e.g.*, micron-sized, finite elements. In this case, the cut-off frequency must be increased to allow for an adequate positioning of the band atoms as discussed above.

In Chapter 6, a hybrid continuum model for dynamic concurrent atomistic-to-continuum methods, was presented. The model represents an attractive alternative to the common approaches dynamic or quasi-static continuum models. The novel approach is based on the superposition of a dynamic and a quasi-static subproblem with complementary BCs.
The approach allows (i) the continuum to be rapidly brought to an equilibrium state, causing the external continuum BCs to immediately take effect on the atomistic region, thereby saving computational resources while (ii) still keeping the continuum dynamics active, thereby avoiding massive wave reflection along the scale interface.
The limitations of the model are as follows: as the superposition property is limited to linear systems, the hybrid continuum model is limited to linear elastic continua. As the external continuum BCs are applied in a quasi-static manner, it is also naturally

not suitable for problems which explicitly require the external continuum BCs to yield dynamic effects in the continuum.
As in Chapter 5, the focus was laid on the application of the approach to the dynamic CADD method. Nevertheless, it was argued that the approach can generally be applied to all dynamic concurrent atomistic-to-continuum methods as long as a linear elastic continuum is used and guidance regarding the application to two other methods was provided.
Three numerical examples were presented, the first two of which highlighted the advantages and drawbacks of the common approaches of dynamic and quasi-static continuum models. It was shown that a dynamic continuum model yields excellent wave reflection behavior but is unsuitable in large continuum regions and may lead to low equilibration rates. While being suitable for large continuum regions, the wave reflection behavior of the quasi-static continuum model is inferior, and improper choices of the continuum time step Δt can seriously and negatively affect the accuracy of the model. The optimal choice of Δt is non-trivial, as it seems to depend on the wave vector. It was shown that the hybrid continuum model is capable of combining the advantages of both methods. In the third example, a practical problem in which the dynamic and quasi-static continuum models are expected to yield comparable results was studied. It was found that the results of the hybrid continuum model agree very well with both.

It is to be hoped that the three presented approaches will find adoption by other researchers and practitioners or serve as a basis to motivate alternative techniques. What is still missing are more general benchmark studies which might help to single out the most effective candidates from the overwhelming and continuously growing list of available atomistic-to-continuum methods. Hopefully, these methods will then receive a wider adoption and combined efforts in their development process. An important step towards industrial adoption is the development of open-source, parallel computing software packages, similar to the those available for single-scale techniques. The presented approaches in this thesis may be part of such a software package.

Appendix

Appendix A.

1D atomic chain coupled to a quasi-static continuum

In the example in Section 6.3.1, it was shown that the choice of the coupling frequency Δt in the quasi-static continuum model is critical to the wave reflection behavior at the interface. Some optimal value of Δt in terms of wave reflection exists, and a deviation from this value in either direction causes increased reflection. This behavior was explained by referring to the two extreme cases of extreme stiffness ($\Delta t \to \infty$) and extreme softness ($\Delta t \to 0$). The purpose of this Appendix is to vividly illustrate both of these cases using a simple example. The one-dimensional chain of five atoms of mass m shown in Fig. A.1a is considered. To simplify the description, only nearest-neighbor interactions as well as small displacements of the atoms from their equilibrium positions are assumed. This leads to the spring-mass system shown in Fig. A.1b with four linear springs of spring constant k.

Fig. A.1.: (a) One dimensional chain of five atoms and (b) its approximation as a spring-mass system.

In the absence of external forces, the equations of motion (EOMs) for the system are

$$m\ddot{u}^{A,1} = -k(u^{A,1} - u^{A,2}) \tag{A.1}$$

$$m\ddot{u}^{A,2} = -k(u^{A,2} - u^{A,1}) - k(u^{A,2} - u^{A,3}) \tag{A.2}$$

$$m\ddot{u}^{A,3} = -k(u^{A,3} - u^{A,2}) - k(u^{A,3} - u^{A,4}) \tag{A.3}$$

$$m\ddot{u}^{A,4} = -k(u^{A,5} - u^{A,3}) - k(u^{A,4} - u^{A,5}) \tag{A.4}$$

$$m\ddot{u}^{A,5} = -k(u^{A,5} - u^{A,4}). \tag{A.5}$$

The displacements u of the atoms are denoted with a superscript "A". The displacements of the nodes introduced are soon written without superscript. The left half of the chain shall be modeled as a continuum, introducing a sharp interface at atom 3 (see Fig. A.2). It is assumed that the continuum node spacing is consistent with the atomic spacing. Note that there is now a pad atom attached to node 2 (illustrated as a hollow circle). In the simple case of nearest-neighbor interactions, only one pad atom is needed.

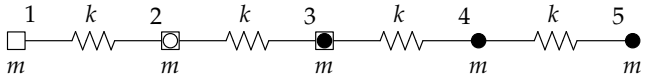

Fig. A.2.: Spatial decomposition of the atomic chain into a continuum region and an atomistic region. Nodes are visualized as squares, atoms as filled circles and pad atoms as hollow circles.

If a dynamic continuum (with lumped mass matrix) is used, the EOMs in Eq. A.1 to Eq. A.5 still hold. If a quasi-static continuum is used, the EOMs of the atoms (Eq. A.3 to Eq. A.5) are still valid; however, the equations in the continuum change. At every Δt time steps, the displacement of node 3 is found from a time average of the displacement of atom 3, *i.e.*,

$$u_3 = \frac{1}{\Delta t} \int_{t-\Delta t}^{t} u^{A,3} \, d\tau. \tag{A.6}$$

The "EOMs" of node 1 and 2 change to (notice the missing inertia term)

$$0 = -k(u^1 - u^2) \tag{A.7}$$

$$0 = -k(u^2 - u^1) - k(u^2 - u^3). \tag{A.8}$$

The two extreme cases, $\Delta t \to \infty$ and $\Delta t \to 0$ shall now be studied.

In the first case, $\Delta t \to \infty$, Eq. A.6 yields $u^3 = 0$. Eq. A.7 and Eq. A.8 yield $u^1 = u^2 = 0$, thus no displacement occurs across the continuum. This affects the atomistic region in the following way. The interface boundary condition (BC) of the atomistic region is given solely through the position of the pad atom, which is attached to node 2. The pad atom position becomes effective in the EOM of atom 3, which now reads as

$$m\ddot{u}^{A,3} = -k(u^{A,3} - \cancel{u^2}) - k(u^{A,3} - u^{A,4}). \tag{A.9}$$

The EOMs of the other atoms (Eq. A.4 and Eq. A.5) do not change. The EOMs of the atoms are thus tantamount to those in the system shown in Fig. A.3. Hence, the atoms feel a rigid wall.

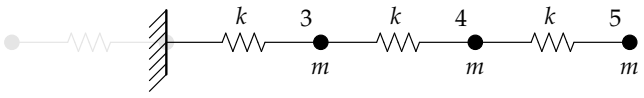

Fig. A.3.: Effective system modeled for $\Delta t \to \infty$.

In the second case, $\Delta t \to 0$, Eq. A.6 yields $u^3 = u^{A,3}$, Eq. A.7 and Eq. A.8 yield $u^1 = u^2 = u^3 = u^{A,3}$ and, thus, a rigid body motion in the continuum. Now, the EOM of atom 3, changes to

$$m\ddot{u}^{A,3} = \cancel{-k(u^{A,3} - u^2)} - k(u^{A,3} - u^{A,4}). \tag{A.10}$$

Again, the EOMs of the other atoms are unchanged. In this case, the atoms feel a free surface, and the EOMs in the atomistic region are tantamount to those of the system shown in Fig. A.4.

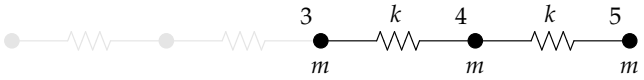

Fig. A.4.: Effective system modeled for $\Delta t \to 0$ (with no external continuum BC).

This free surface BC on the atoms results from the continuum permanently being in a state of zero stress. This is only the case if no external displacement BCs and no external tractions are present on the continuum. It will now be exemplarily shown that, *e.g.*, in the case of an external displacement BC, there is no longer a free surface, but instead a rigid wall with a reduced spring constant. This boundary is equivalently unphysical. To this end, the same system as before (Fig. A.2) is considered; however, it is clamped at the left-hand end at the continuum, *i.e.*, $u^1 = 0$ (see Fig. A.5).

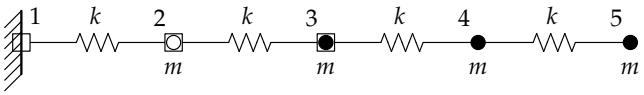

Fig. A.5.: Spatial decomposition of the atomic chain into a continuum region and an atomistic region. The left end of the system is clamped.

We are still concerned with the second case, *i.e.* $\Delta t \to 0$ and therefore $u^3 = u^{A,3}$. For the clamped boundary with $u^1 = 0$, Eq. A.8 still holds and now yields $u^2 = \frac{1}{2}u_3 = \frac{1}{2}u^{A,3}$. In this case, the EOM of atom 3, changes to

$$\begin{aligned} m\ddot{u}^{A,3} &= -k(u^{A,3} - \frac{1}{2}u^{A,3}) - k(u^{A,3} - u^{A,4}) \\ &= -\frac{k}{2}(u^{A,3}) - k(u^{A,3} - u^{A,4}). \end{aligned} \tag{A.11}$$

Again, the EOMs of the other atoms remain unchanged. In this case, the EOMs in the atomistic region are tantamount to those for the system shown in Fig. A.6.

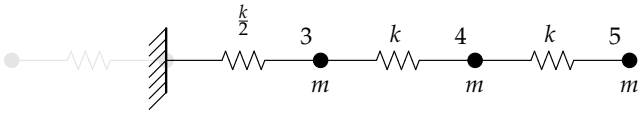

Fig. A.6.: Effective system modeled for $\Delta t \to 0$ (with clamped left boundary).

The system is similar to Fig. A.3, although the spring constant at the interface is now reduced by a factor of $1/2$, which is directly derived from the length of the continuum $l = 2a$, where a is the equilibrium spacing of the atoms. If there were 1000 elements of the same size across the continuum with the very left-hand node clamped, the spring stiffness would be reduced to $1/1000k$. Therefore, in the limit $l \to \infty$, the spring stiffness approaches zero, and the free surface BC (Fig. A.4) is recovered.

One can see that the first extreme case $\Delta t \to \infty$ leads to BCs for the atomistic region which are too stiff. On the other hand, the second case $\Delta t \to 0$ leads to BCs which are too soft. Both of these unphysical cases lead to increased amounts of wave reflection at the interface. Realistic BCs which minimize wave reflection are found in between these extreme values (see Section 6.3.1).

Bibliography

Abdulle, A., W. E, B. Engquist, and E. Vanden-Eijnden (2012). "The heterogeneous multiscale method". In: *Acta Numer.* 21, pp. 1–87. DOI: 10.1017/S0962492912000025 (cit. on p. 27).

Abraham, F., N. Bernstein, J. Broughton, and D. Hess (2000). "Dynamic fracture of silicon: Concurrent simulation of quantum electrons, classical atoms, and the continuum solid". In: *MRS Bull.* 25. DOI: 10.1557/mrs2000.70 (cit. on pp. 25, 82).

Abraham, F. F., J. Q. Broughton, N. Bernstein, and E. Kaxiras (1998). "Spanning the length scales in dynamic simulation". In: *J. Comput. Phys.* 12.6, pp. 538–546. DOI: 10.1063/1.168756 (cit. on pp. 25, 82).

Allen, M. P. and D. J. Tildesley (1989). *Computer Simulation of Liquids*. Oxford: Clarendon Press. ISBN: 9780198556459 (cit. on pp. 15, 20).

Aluko, O., S. Gowtham, and G. M. Odegard (2017). "Multiscale modeling and analysis of graphene nanoplatelet/carbon fiber/epoxy hybrid composite". In: *Compos. Part B-Eng.* 131, pp. 82–90. DOI: 10.1016/j.compositesb.2017.07.075 (cit. on p. 2).

Anciaux, G., T. Junge, M. Hodapp, J. Cho, J.-F. Molinari, and W. A. Curtin (2018). "The coupled atomistic/discrete-dislocation method in 3d part I: Concept and algorithms". In: *J. Mech. Phys. Solids* 118, pp. 152–171. DOI: 10.1016/j.jmps.2018.05.004 (cit. on p. 26).

Anciaux, G., S. B. Ramisetti, and J.-F. Molinari (2012). "A finite temperature bridging domain method for MD-FE coupling and application to a contact problem". In: *Comput. Meth. Appl. Mech. Eng.* 205-208, pp. 204–212. DOI: 10.1016/j.cma.2011.01.012 (cit. on pp. 25, 82).

Andersen, H. C. (1980). "Molecular dynamics simulations at constant pressure and/or temperature". In: *J. Chem. Phys.* 72, pp. 2384–2393. DOI: 10.1063/1.439486 (cit. on p. 31).

Anderson, P. M., J. P. Hirth, and J. Lothe (2017). *Theory of Dislocations*. 3rd ed. Cambridge: Cambridge University Press (cit. on pp. 60, 80).

Arndt, D., W. Bangerth, T. C. Clevenger, D. Davydov, M. Fehling, D. Garcia-Sanchez, G. Harper, T. Heister, L. Heltai, M. Kronbichler, R. M. Kynch, M. Maier, J.-P. Pelteret, B. Turcksin, and D. Wells (2019). "The deal.II library, version 9.1". In: *J. Numer. Math.* 27.4, pp. 203–213. DOI: 10.1515/jnma-2019-0064. URL: https://dealii.org/ (cit. on p. 3).

Badia, S., M. Parks, P. Bochev, M. Gunzburger, and R. Lehoucq (2008). "On atomistic-to-continuum coupling by blending". In: *Multiscale Model. Sim.* 7.1, pp. 381–406. DOI: 10.1137/07069969X (cit. on p. 25).

Barton, N., J. Bernier, R. Becker, A. Arsenlis, R. Cavallo, J. Marian, M. Rhee, H.-S. Park, B. Remington, and R. Olson (2011). "A multiscale strength model for extreme loading conditions". In: *J. Appl. Phys.* 109, p. 073501. DOI: 10.1063/1.3553718 (cit. on p. 28).

Bather, J. A. (1989). "Stochastic approximation: A generalization of the Robbins-Monro procedure". In: *Proceedings of the Fourth Prague Symposium on Asymptotic Statistics*. Ed. by P Mandl and M Hušková. Prague: Charles University, pp. 13–27 (cit. on p. 39).

Belytschko, T., W. K. Liu, and B. Moran (2000). *Nonlinear Finite Elements for Continua and Structures*. New York: Wiley. ISBN: 9780471987734 (cit. on pp. 7, 11, 13, 14).

Benaim, M. (1993). "The 'off line learning approximation' in continuous time neural networks: An adiabatic theorem". In: *Neural Netw.* 6, pp. 655–665. DOI: 10.1016/S0893-6080(05)80109-1 (cit. on p. 30).

Bonet, J. and R. D. Wood (1997). *Nonlinear Continuum Mechanics for Finite Element Analysis*. Cambridge: Cambridge University Press. ISBN: 9780521572729 (cit. on pp. 7, 9).

Broughton, J. Q., F. F. Abraham, N. Bernstein, and E. Kaxiras (1999). "Concurrent coupling of length scales: Methodology and application". In: *Phys. Rev. B* 60 (4), pp. 2391–2403. DOI: 10.1103/PhysRevB.60.2391 (cit. on pp. 25, 82).

Budarapu, P. R., X. Zhuang, T. Rabczuk, and S. P. A. Bordas (2019). "Chapter One - Multiscale modeling of material failure: Theory and computational methods". In: *Advances in Crystals and Elastic Metamaterials, Part 2*. Vol. 52, pp. 1–103. DOI: 10.1016/bs.aams.2019.04.002 (cit. on p. 28).

Cai, W., V. V. Bulatov, T. G. Pierce, M. Hiratani, M. Rhee, M. Bartelt, and M. Tang (2004). "Massively-parallel dislocation dynamics simulations". In: *IUTAM Symposium on Mesoscopic Dynamics of Fracture Process and Materials Strength*. Springer Netherlands, pp. 1–11. DOI: 10.1007/978-1-4020-2111-4_1. URL: http://paradis.stanford.edu/ (cit. on p. 3).

Çain, T. and B. M. Pettitt (1989). "Elastic constants of nickel: Variations with respect to temperature and pressure". In: *Phys. Rev. B* 39, pp. 12484–12491. DOI: 10.1103/physrevb.39.12484 (cit. on p. 34).

Chandler, D. and D. Wu (1987). *Introduction to Modern Statistical Mechanics*. Oxford: Oxford University Press. ISBN: 9780195042771 (cit. on p. 15).

Chen, L., P. Debenedetti, C. Gear, and I. Kevrekidis (2004). "From molecular dynamics to coarse self-similar solutions: A simple example using equation-free computation". In: *J. Non-Newton. Fluid* 120. DOI: 10.1016/j.jnnfm.2003.12.007 (cit. on p. 27).

Chen, W. and J. Fish (2006). "A generalized space–time mathematical homogenization theory for bridging atomistic and continuum scales". In: *Int. J. Numer. Meth. Eng.* 67.2, pp. 253–271. DOI: 10.1002/nme.1630 (cit. on p. 27).

Chen, Y., S. Shabanov, and D. McDowell (2019). "Concurrent atomistic continuum modeling of crystalline materials". In: *J. Appl. Phys.* 126, p. 101101. DOI: 10.1063/1.5099653 (cit. on p. 26).

Chen, Z., S. Jiang, Y. Gan, H. Liu, and T. D. Sewell (2014). "A particle-based multiscale simulation procedure within the material point method framework". In: *Comput. Part. Mech.* 1.2, pp. 147–158. DOI: 10.1007/s40571-014-0016-5 (cit. on p. 2).

Cheng, B. and D. M. Titterington (1994). "Neural networks: A review from a statistical perspective". In: *Stat. Sci.* 9, pp. 2–30. DOI: 10.1214/ss/1177010638 (cit. on p. 30).

Cho, J., J.-F. Molinari, W. A. Curtin, and G. Anciaux (2018). "The coupled atomistic/discrete-dislocation method in 3d part III: Dynamics of hybrid dislocations". In: *J. Mech. Phys. Solids* 118, pp. 1–14. DOI: 10.1016/j.jmps.2018.05.005 (cit. on p. 26).

Chockalingam, K. and L. C. Wellford (2011). "Multi-scale homogenization procedure for continuum–atomistic, thermo-mechanical problems". In: *Comput. Method. Appl. M.* 200.1, pp. 356–371. ISSN: 0045-7825. DOI: 10.1016/j.cma.2010.08.016 (cit. on p. 28).

Daw, M. S. and M. I. Baskes (1984). "Embedded-atom method: Derivation and application to impurities, surfaces, and other defects in metals". In: *Phys. Rev. B* 29 (12), pp. 6443–6453. DOI: 10.1103/PhysRevB.29.6443 (cit. on p. 19).

Dupuy, L. M., E. B. Tadmor, R. E. Miller, and R. Phillips (2005). "Finite-temperature quasicontinuum: Molecular dynamics without all the atoms". In: *Phys. Rev. Lett.* 95 (6), p. 060202. DOI: 10.1103/PhysRevLett.95.060202 (cit. on p. 24).

E, W. and B. Engquist (2003). "The heterogenous multiscale methods". In: *Commun. Math. Sci.* 1.1, pp. 87–132. DOI: 10.4310/CMS.2003.v1.n1.a8 (cit. on p. 27).

E, W., W. Ren, and E. Vanden-Eijnden (2009). "A general strategy for designing seamless multiscale methods". In: *J. Comput. Phys.* 228.15, pp. 5437–5453. DOI: 10.1016/j.jcp.2009.04.030 (cit. on p. 27).

El Alem, W., A. El Hami, and R. Ellaia (2011). "A new methodology for an optimal shape design". In: *Appl. Mech. Mater.* 61, pp. 43–54. DOI: 10.4028/www.scientific.net/AMM.61.43 (cit. on p. 30).

Engquist, B., X. Li, W. Ren, and E. Vanden-Eijnden (2007). "The heterogeneous multiscale methods: A review". In: *Commun. Comput. Phys.* 2, pp. 367–450 (cit. on p. 27).

Ericksen, J. L. (2008). "On the Cauchy-Born rule". In: *Math. Mech. Solids* 13, pp. 199–220. DOI: 10.1177/1081286507086898 (cit. on p. 35).

Fish, J., W. Chen, and R. Li (2007). "Generalized mathematical homogenization of atomistic media at finite temperatures in three dimensions". In: *Comput. Method. Appl. M.* 196.4, pp. 908–922. ISSN: 0045-7825. DOI: 10.1016/j.cma.2006.08.001 (cit. on p. 27).

Fish, J., M. A. Nuggehally, M. S. Shephard, C. R. Picu, S. Badia, M. L. Parks, and M. Gunzburger (2007). "Concurrent AtC coupling based on a blend of the continuum stress and the atomistic force". In: *Comput. Method. Appl. M.* 196.45, pp. 4548–4560. DOI: 10.1016/j.cma.2007.05.020 (cit. on p. 25).

Frenkel, D. and B. Smit (2001). *Understanding Molecular Simulation: From Algorithms to Applications*. Amsterdam: Elsevier. ISBN: 9780080519982 (cit. on p. 15).

Giannozzi, P., S. Baroni, N. Bonini, M. Calandra, R. Car, C. Cavazzoni, D. Ceresoli, G. L. Chiarotti, M. Cococcioni, I. Dabo, A. D. Corso, S. de Gironcoli, S. Fabris, G. Fratesi, R. Gebauer, W. Gerstmann, C. Gougoussis, A. Kokalj, M. Lazzerim, L. Martin-Samos, N. Marzari, F. Mauri, R. Mazzarello, S. Paolini, A. Pasquarello, L. Paulatto, C. Sbraccia, S. Scandolo, G. Sclauzero, A. P. Seitsonen, A. Smogunov, P. Umari, and R. M. Wentzcovitch (2009). "QUANTUM ESPRESSO: a modular and open-source software project for quantum simulations of materials". In: *J. Phys. Condens. Matter* 21.39, p. 395502. DOI: 10.1088/0953-8984/21/39/395502. URL: https://www.quantum-espresso.org/ (cit. on p. 3).

Gracie, R. and T. Belytschko (2009). "Concurrently coupled atomistic and XFEM models for dislocations and cracks". In: *Int. J. Numer. Meth. Eng.* 78.3, pp. 354–378. DOI: 10.1002/nme.2488 (cit. on p. 25).

Gracie, R. and T. Belytschko (2011). "An adaptive concurrent multiscale method for the dynamic simulation of dislocations". In: *Int. J. Numer. Meth. Eng.* 86.4-5, pp. 575–597. DOI: 10.1002/nme.3112 (cit. on p. 25).

Halicioğlu, T. and G. M. Pound (1975). "Calculation of potential energy parameters form crystalline state properties". In: *Phys. Status Solidi. A* 30.2, pp. 619–623. DOI: 10.1002/pssa.2210300223 (cit. on p. 70).

Hodapp, M., G. Anciaux, J.-F. Molinari, and W. A. Curtin (2018). "Coupled atomistic/discrete dislocation method in 3d part II: Validation of the method". In: *J. Mech. Phys. Solids* 119, pp. 1–19. DOI: 10.1016/j.jmps.2018.05.003 (cit. on p. 26).

Holian, B. L. and R. Ravelo (1995). "Fracture simulations using large-scale molecular dynamics". In: *Phys. Rev. B* 51, pp. 11275–11288. DOI: 10.1103/physrevb.51.11275 (cit. on pp. 21, 71).

Holzapfel, G. A. (2000). *Nonlinear Solid Mechanics: A Continuum Approach for Engineering*. New York: Wiley. ISBN: 9780471823193 (cit. on pp. 7, 9).

Hoover, W. G. (1985). "Canonical dynamics: Equilibrium phase-space distributions". In: *Phys. Rev. A* 31 (3), pp. 1695–1697. DOI: 10.1103/PhysRevA.31.1695 (cit. on pp. 21, 32).

Hünenberger, P. H. (2005). "Thermostat algorithms for molecular dynamics simulations". In: *Adv. Polym. Sci.* 173, pp. 105–149. DOI: 10.1007/b99427 (cit. on pp. 21, 32, 71).

Iacobellis, V. and K. Behdinan (2013). "Comparison of concurrent multiscale methods in the application of fracture in nickel". In: *J. Appl. Mech-T. ASME* 80, p. 051003. DOI: 10.1115/1.4023477 (cit. on p. 23).

Jahanshahi, M., H. Ahmadi, and A. R. Khoei (2020). "A hierarchical hyperelastic-based approach for multi-scale analysis of defective nano-materials". In: *Mech. Mater.* 140, p. 103206. ISSN: 0167-6636. DOI: 10.1016/j.mechmat.2019.103206 (cit. on p. 28).

Jones, J. E. and S. Chapman (1924). "On the determination of molecular fields. From the equation of state of a gas". In: *P. Roy. Soc. A-Math. Phy.* 106.738, pp. 463–477. DOI: 10.1098/rspa.1924.0082 (cit. on p. 19).

Ju, S.-P., J.-S. Lin, and W.-J. Lee (2004). "A molecular dynamics study of the tensile behaviour of ultrathin gold nanowires". In: *Nanotechnology* 15.9, pp. 1221–1225. DOI: 10.1088/0957-4484/15/9/019 (cit. on p. 101).

Junge, T., G. Anciaux, and J.-F. Molinari (2015). "Dynamic stability of displacement-based atomistic/continuum coupling methods". In: *J. Mech. Phys. Solids* 80, pp. 103–120. DOI: 10.1016/j.jmps.2015.04.004 (cit. on pp. 25, 95).

Kantorovich, L. (2008a). "Generalized Langevin equation for solids. I. Rigorous derivation and main properties". In: *Phys. Rev. B* 78, p. 094304. DOI: 10.1103/PhysRevB.78.094304 (cit. on pp. 21, 71).

Kantorovich, L. (2008b). "Generalized Langevin equation for solids. II. Stochastic boundary conditions for nonequilibrium molecular dynamics simulations". In: *Phys. Rev. B* 78, p. 094305. DOI: 10.1103/PhysRevB.78.094305 (cit. on pp. 21, 71).

Karakasidis, T. E. and C. A. Charitidis (2007). "Multiscale modeling in nanomaterials science". In: *Mater. Sci. Eng., C* 27.5, pp. 1082–1089. DOI: 10.1016/j.msec.2006.06.029 (cit. on p. 2).

Keralavarma, S., A. Bower, and W. Curtin (2014). "Quantum-to-continuum prediction of ductility loss in aluminium-magnesium alloys due to dynamic strain aging". In: *Nat. Commun.* 5, p. 4604. DOI: 10.1038/ncomms5604 (cit. on p. 28).

Kevrekidis, I., C. Gear, J. Hyman, P. Kevrekidid, O. Runborg, and C. Theodoropoulos (2003). "Equation-free, coarse-grained multiscale computation: Enabling microscopic simulators to perform system-level analysis". In: *Commun. Math. Sci.* 1. DOI: 10.4310/CMS.2003.v1.n4.a5 (cit. on p. 27).

Kevrekidis, I. G., C. W. Gear, and G. Hummer (2004). "Equation-free: The computer-aided analysis of complex multiscale systems". In: *AIChE J.* 50.7, pp. 1346–1355. DOI: 10.1002/aic.10106 (cit. on p. 27).

Kiefer, J. and J. Wolfowitz (1952). "Stochastic estimation of the maximum of a regression function". In: *Ann. Math. Statist.* 23, pp. 462–466. DOI: 10.1214/aoms/1177729392 (cit. on p. 38).

Kim, W. K., M. Luskin, D. Perez, A. F. Voter, and E. B. Tadmor (2014). "Hyper-QC: An accelerated finite-temperature quasicontinuum method using hyperdynamics". In: *J. Mech. Phys. Solids* 63, pp. 94–112. DOI: 10.1016/j.jmps.2013.10.001 (cit. on p. 24).

Kohlhoff, S., P. Gumbsch, and H. F. Fischmeister (1991). "Crack propagation in b.c.c. crystals studied with a combined finite-element and atomistic model". In: *Phil. Mag. A* 64.4, pp. 851–878. DOI: 10.1080/01418619108213953 (cit. on p. 25).

Kushner, H. J. and J. Yang (1993). "Stochastic approximation with averaging of the iterates: Optimal asymptotic rate of convergence for general processes". In: *SIAM J. Control Optim.* 31 (4), pp. 1045–1062. DOI: 10.1137/0331047 (cit. on p. 39).

Kushner, H. J. and G. G. Yin (2003). *Stochastic Approximation and Recursive Algorithms and Applications*. New York: Springer (cit. on pp. 29, 36, 37, 39).

Lazarus, D. (1949). "The Variation of the adiabatic elastic constants of KCl, NaCl, CuZn, Cu, and Al with pressure to 10,000 bars". In: *Phys. Rev.* 76.4, pp. 545–53. DOI: 10.1103/PhysRev.76.545 (cit. on pp. 50, 54).

Lekhnitskii, S. (1968). *Anisotropic Plates*. London: Gordon & Breach (cit. on pp. 50, 54).

Li, A., R. Li, and J. Fish (2008). "Generalized mathematical homogenization: From theory to practice". In: *Comput. Method. Appl. M.* 197, pp. 3225–3248. DOI: 10.1016/j.cma.2007.12.002 (cit. on p. 27).

Li, X. and W. E (2005). "Multiscale modeling of the dynamics of solids at finite temperature". In: *J. Mech. Phys. Solids* 53.7, pp. 1650–1685. ISSN: 0022-5096. DOI: 10.1016/j.jmps.2005.01.008 (cit. on p. 27).

Li, X., J. Z. Yang, and W. E (2010). "A multiscale coupling method for the modeling of dynamics of solids with application to brittle cracks". In: *J. Comput. Phys.* 229.10, pp. 3970–3987. ISSN: 0021-9991. DOI: 10.1016/j.jcp.2010.01.039 (cit. on p. 27).

López-Rubio, E. and R. M. Luque-Baena (2011). "Stochastic approximation for background modelling". In: *Comput. Vis. Image Underst.* 115, pp. 735–749. DOI: 10.1016/j.cviu.2011.01.007 (cit. on p. 30).

Lu, G., E. B. Tadmor, and E. Kaxiras (2006). "From electrons to finite elements: A concurrent multiscale approach for metals". In: *Phys. Rev. B* 73 (2), p. 024108. DOI: 10.1103/PhysRevB.73.024108 (cit. on p. 24).

Malvern, L. E. (1969). *Introduction to the Mechanics of a Continuous Medium*. Prentice-Hall series in engineering of the physical sciences. New Jersey: Prentice-Hall (cit. on p. 7).

Marsden, J. E. and T. J. R. Hughes (1994). *Mathematical Foundations of Elasticity*. Dover Civil and Mechanical Engineering Series. Mineola: Dover. ISBN: 9780486678658 (cit. on p. 7).

Mathew, N., R. C. Picu, and M. Bloomfield (2011). "Concurrent coupling of atomistic and continuum models at finite temperature". In: *Comput. Meth. Appl. Mech. Eng.* 200.5, pp. 765–773. DOI: 10.1016/j.cma.2010.09.018 (cit. on p. 58).

Miller, R. E. and E. B. Tadmor (2009). "A unified framework and performance benchmark of fourteen multiscale atomistic/continuum coupling methods". In: *Model. Simulat. Mater. Sci. Eng.* 17, 053001. DOI: 10.1088/0965-0393/17/5/053001 (cit. on pp. 23, 82).

NIST (2020). *National Institute of Standards and Technology: Interatomic Potentials Repository*. DOI: 10.18434/m37. URL: https://www.ctcms.nist.gov/potentials/Download/2004--Zhou-X-W-Johnson-R-A-Wadley-H-N-G--Al/4/Al_Zhou04.eam.alloy (visited on 11/01/2020) (cit. on p. 90).

Nosé, S. (1984). "A unified formulation of the constant temperature molecular dynamics methods". In: *J. Chem. Phys.* 81.1, pp. 511–519. DOI: 10.1063/1.447334 (cit. on pp. 21, 32).

Park, H., E. Karpov, and W. Liu (2004). "A temperature equation for coupled atomistic/continuum simulations". In: *Comput. Method. Appl. M.* 193, p. 1713. DOI: 10.1016/j.cma.2003.12.023 (cit. on p. 25).

Parks, M., P. Bochev, and R. Lehoucq (2008). "Connecting atomistic-to-continuum coupling and domain decomposition". In: *Multiscale Model. Sim.* 7, pp. 362–380. DOI: 10.1137/070682848 (cit. on p. 25).

Parrinello, M. and A. Rahman (1981). "Polymorphic transitions in single crystals: A new molecular dynamics method". In: *J. Appl. Phys.* 52, pp. 7182–7190. DOI: 10.1063/1.328693 (cit. on p. 31).

Plimpton, S. (1995). "Fast parallel algorithms for short-range molecular dynamics". In: *J. Comput. Phys.* 117.1, pp. 1–19. ISSN: 0021-9991. DOI: 10.1006/jcph.1995.1039. URL: https://lammps.sandia.gov/ (cit. on p. 3).

Podio-Guidugli, P. (2010). "On (Andersen-)Parrinello-Rahman molecular dynamics, the related metadynamics, and the use of the Cauchy-Born Rule". In: *J. Elasticity* 100, pp. 145–153. DOI: 10.1007/s10659-010-9250-0 (cit. on p. 31).

Polyak, B. T. and A. B. Juditsky (1992). "Acceleration of stochastic approximation by averaging". In: *SIAM J. Control Optim.*, pp. 838–855. DOI: 10.1137/0330046 (cit. on p. 39).

Qian, D., G. J. Wagner, and W. K. Liu (2004). "A multiscale projection method for the analysis of carbon nanotubes". In: *Comput. Method. Appl. M.* 193.17, pp. 1603–1632. DOI: 10.1016/j.cma.2003.12.016 (cit. on p. 25).

Qu, S., V. Shastry, W. A. Curtin, and R. E. Miller (2005). "A finite-temperature dynamic coupled atomistic/discrete dislocation method". In: *Model. Simulat. Mater. Sci. Eng.* 13, p. 1101. DOI: 10.1088/0965-0393/13/7/007 (cit. on pp. 21, 26, 61, 68, 71, 74, 81–83).

Ramisetti, S. B., G. Anciaux, and J.-F. Molinari (2013). "Spatial filters for bridging molecular dynamics with finite elements at finite temperatures". In: *Comput. Meth. Appl. Mech. Eng.* 253, pp. 28–38. DOI: 10.1016/j.cma.2012.09.008 (cit. on p. 58).

Ramisetti, S. B., G. Anciaux, and J.-F. Molinari (2014). "A concurrent atomistic and continuum coupling method with applications to thermo-mechanical problems". In: *Int. J. Numer. Meth. Eng.* 97.10, pp. 707–738. DOI: 10.1002/nme.4606 (cit. on p. 58).

Ray, J. R. and A. Rahman (1985). "Statistical ensembles and molecular dynamics studies of anisotropic solids. II". In: *J. Chem. Phys.* 82, pp. 4243–4247. DOI: 10.1063/1.448813 (cit. on p. 31).

Reid, A.C.E., R. Lua, E. García, V. R. Coffman, and S. Langer (2009). "Modelling microstructures with OOF2". In: *Int. J. Mater. Prod. Tec.* 35, pp. 361–373. DOI: 10.1504/IJMPT.2009.025687. URL: https://www.ctcms.nist.gov/oof/oof2/ (cit. on p. 3).

Robbins, H. and S. Monro (1951). "A stochastic approximation method". In: *Ann. Math. Statist.* 22, pp. 400–407. DOI: 10.1214/aoms/1177729586 (cit. on p. 37).

Rudd, R. E. (2001). "The atomic limit of finite element modeling in MEMS: Coupling of length scales". In: *Analog. Integr. Circ. S.* 29.1-2, pp. 17–26. DOI: 10.1023/A:1011217927309 (cit. on p. 2).

Schwabe, R. (1994). "On Bather's stochastic approximation algorithm". In: *Kybernetika* 30.3, pp. 301–306 (cit. on p. 39).

Seyedpoor, S. M., J. Salajegheh, E. Salajegheh, and S. Gholizadeh (2011). "Optimal design of arch dams subjected to earthquake loading by a combination of simultaneous perturbation stochastic approximation and particle swarm algorithms". In: *Appl. Soft. Comput.* 11, pp. 39–48. DOI: 10.1016/j.asoc.2009.10.014 (cit. on p. 30).

Shenoy, V. B., R. Miller, E. B. Tadmor, R. Phillips, and M. Ortiz (1998). "Quasicontinuum models of interfacial structure and deformation". In: *Phys. Rev. Lett.* 80 (4), pp. 742–745. DOI: 10.1103/PhysRevLett.80.742 (cit. on p. 24).

Shenoy, V. B., R. Miller, E. B. Tadmor, D. Rodney, R. Phillips, and M. Ortiz (1999). "An adaptive finite element approach to atomic-scale mechanics—the quasicontinuum method". In: *J. Mech. Phys. Solids* 47.3, pp. 611–642. DOI: 10.1016/S0022-5096(98)00051-9 (cit. on p. 24).

Shiari, B., R. E. Miller, and W. A. Curtin (2005). "Coupled atomistic/discrete dislocation simulations of nanoindentation at finite temperature". In: *J. Eng. Mater. Tech.* 127, pp. 358–368. DOI: 10.1115/1.1924561 (cit. on pp. 26, 61, 68, 82, 83).

Shilkrot, L. E., R. E. Miller, and W. A. Curtin (2002). "Coupled atomistic and discrete dislocation plasticity". In: *Phys. Rev. Lett.* 89.2, p. 025501. DOI: 10.1103/PhysRevLett.89.025501 (cit. on p. 25).

Shilkrot, L. E., R. E. Miller, and W. A. Curtin (2004). "Multiscale plasticity modeling: coupled atomistics and discrete dislocation mechanics". In: *J. Mech. Phys. Solids* 52.4, pp. 755–787. DOI: 10.1016/j.jmps.2003.09.023 (cit. on p. 25).

Smith, S. W. (2002). *Digital Signal Processing - A Practical Guide for Engineers and Scientists*. Amsterdam: Elsevier (cit. on pp. 62, 63).

Spall, J. C. (1992). "Multivariate stochastic approximation using a simultaneous perturbation gradient approximation". In: *IEEE Trans. Autom. Control* 37.3, pp. 332–341. DOI: 10.1109/9.119632 (cit. on p. 38).

Spall, J. C. (2000). "Adaptive stochastic approximation by the simultaneous perturbation method". In: *IEEE Trans. Autom. Control* 45.10, pp. 1839–1853. DOI: 10.1109/CDC.1998.761833 (cit. on p. 38).

Spall, J. C. (2003). *Introduction to Stochastic Search and Optimization: Estimation, Simulation, and Control*. New Jersey: Wiley (cit. on pp. 29, 37–39, 42).

Stukowski, A. (2014). "A triangulation-based method to identify dislocations in atomistic models". In: *J. Mech. Phys. Solids* 70, pp. 314–319. DOI: 10.1016/j.jmps.2014.06.009 (cit. on p. 78).

Sultan, C. (2010). "Proportional damping approximation using the energy gain and simultaneous perturbation stochastic approximation". In: *Mech. Syst. Signal Proc.* 24, pp. 2210–2224. DOI: 10.1016/j.ymssp.2010.02.013 (cit. on p. 30).

Swope, W. C., H. C. Andersen, P. H. Berens, and K. R. Wilson (1982). "A computer simulation method for the calculation of equilibrium constants for the formation of physical clusters of molecules: Application to small water clusters". In: *J. Chem. Phys.* 76.1, pp. 637–649. DOI: 10.1063/1.442716 (cit. on p. 20).

Tadmor, E. B., F. Legoll, W. K. Kim, L. M. Dupuy, and R. E. Miller (2013). "Finite-Temperature Quasi-Continuum". In: *Appl. Mech. Rev.* 65.1, p. 010803. DOI: 10.1115/1.4023013 (cit. on p. 24).

Tadmor, E. B. and R. E. Miller (2011). *Modeling Materials: Continuum, Atomistic and Multiscale Techniques*. Cambridge: Cambridge University Press. ISBN: 9781139500654 (cit. on pp. 2, 15, 23, 25, 33, 102).

Tadmor, E. B., R. E. Miller, and R. S. Elliott (2011). *Continuum Mechanics and Thermodynamics: From Fundamental Concepts to Governing Equations*. Cambridge: Cambridge University Press. ISBN: 9781139504829 (cit. on pp. 7, 13).

Tadmor, E. B., M. Ortiz, and R. Phillips (1996). "Quasicontinuum analysis of defects in solids". In: *Phil. Mag. A* 73, pp. 1529–1563. DOI: 10.1080/01418619608243000 (cit. on pp. 24, 106).

Templeton, J., R. Jones, and G. Wagner (2010). "Application of a field-based method to spatially varying thermal transport problems in molecular dynamics". In: *Model. Simul. in Mater. Sci.* 18, p. 085007. DOI: 10.1088/0965-0393/18/8/085007 (cit. on p. 25).

Truesdell, C. and W. Noll (1992). *The Non-linear Field Theories of Mechanics*. The non-linear field theories of mechanics Bd. 2. Berlin: Springer. ISBN: 9783540550983 (cit. on p. 7).

Tuckerman, M. (2010). *Statistical Mechanics: Theory and Molecular Simulation*. Oxford: Oxford University Press. ISBN: 9780191523465 (cit. on pp. 15–17, 19–21).

Ulz, M. H. (2013). "Comments on a continuum-related Parrinello-Rahman molecular dynamics formulation". In: *J. Elasticity* 113, pp. 93–112. DOI: 10.1007/s10659-012-9412-3 (cit. on p. 31).

Ulz, M. H. (2015a). "A multiscale molecular dynamics method for isothermal dynamic problems using the seamless heterogeneous multiscale method". In: *Comput. Method. Appl. M.* 295. DOI: 10.1016/j.cma.2015.07.019 (cit. on p. 28).

Ulz, M. H. (2015b). "Coupling the finite element method and molecular dynamics in the framework of the heterogeneous multiscale method for quasi-static isothermal problems". In: *J. Mech. Phys. Solids* 74, pp. 1–18. ISSN: 0022-5096. DOI: 10.1016/j.jmps.2014.10.002 (cit. on pp. 28, 31–33, 36).

Ulz, M. H. (2019). "A continuum-on-atomistic framework with bi-stable elements for the computation of minimum free energy paths". In: *Mech. Solids* 54, pp. 975–994. DOI: 10.3103/S0025654419060128 (cit. on p. 28).

Van der Giessen, E. and A. Needleman (1995). "Discrete dislocation plasticity: a simple planar model". In: *Model. Simulat. Mater. Sci. Eng.* 3.5, pp. 689–735. DOI: 10.1088/0965-0393/3/5/008 (cit. on pp. 26, 59).

Van der Giessen, E., P. A. Schultz, N. Bertin, V. V. Bulatov, W. Cai, G. Csányi, S. M. Foiles, M. G. D. Geers, C. González, M. Hütter, W. K. Kim, D. M. Kochmann, J. LLorca, A. E. Mattsson, J. Rottler, A. Shluger, R. B. Sills, I. Steinbach, A. Strachan, and E. B. Tadmor (2020). "Roadmap on multiscale materials modeling". In: *Model. Simul. Mater. Sc.* 28.4, p. 043001. DOI: 10.1088/1361-651x/ab7150. URL: https://doi.org/10.1088%2F1361-651x%2Fab7150 (cit. on p. 3).

Wagner, G., R. Jones, J. Templeton, and M. Parks (2008). "An atomistic-to-continuum coupling method for heat transfer in solids". In: *Comput. Method. Appl. M.* 197, pp. 3351–3365. DOI: 10.1016/j.cma.2008.02.004 (cit. on p. 25).

Wagner, G. J. and W. K. Liu (2003). "Coupling of atomistic and continuum simulations using a bridging scale decomposition". In: *J. Comput. Phys.* 190.1, pp. 249–274. DOI: 10.1016/S0021-9991(03)00273-0 (cit. on pp. 25, 74).

Weiner, J. H. (2002). *Statistical Mechanics of Elasticity*. New York: Wiley. ISBN: 9780486422602 (cit. on p. 15).

Wen-Long, C., H. Yong-Hua, L. Na, and M. Ran (2012). "Estimation of geological formation thermal conductivity by using stochastic approximation method based on well-log temperature data". In: *Energy* 38, pp. 21–30. DOI: 10.1016/j.energy.2011.12.047 (cit. on p. 30).

Wurm, P. and M. H. Ulz (2016). "A stochastic approximation approach to improve the convergence behavior of hierarchical atomistic-to-continuum multiscale models". In: *J. Mech. Phys. Solids* 95, pp. 480–500. ISSN: 0022-5096. DOI: 10.1016/j.jmps.2016.05.024 (cit. on p. 29).

Wurm, P. and M. H. Ulz (2020). "Demand-based coupling of the scales in concurrent atomistic-to-continuum models at finite temperature". In: *J. Mech. Phys. Solids* 137, p. 103849. ISSN: 0022-5096. DOI: 10.1016/j.jmps.2019.103849 (cit. on p. 57).

Xiang, M., J. Cui, B. Li, and X. Tian (2012). "Atom-continuum coupled model for thermo-mechanical behavior of materials in micro-nano scales". In: *Sci. China Phys. Mech.* 55. DOI: 10.1007/s11433-012-4765-y (cit. on p. 28).

Xiao, S. P. and T. Belytschko (2004). "A bridging domain method for coupling continua with molecular dynamics". In: *Comput. Meth. Appl. Mech. Eng.* 193.17–20, pp. 1645–1669. DOI: 10.1016/j.cma.2003.12.053 (cit. on p. 25).

Xiong, L., Q. Deng, G. Tucker, D. McDowell, and Y. Chen (2012). "A concurrent scheme for passing dislocations from atomistic to continuum domains". In: *Acta Mater.* 60. DOI: 10.1016/j.actamat.2011.11.002 (cit. on p. 26).

Xiong, L., G. Tucker, D. McDowell, and Y. Chen (2011). "Coarse-grained atomistic simulation of dislocations". In: *J. Mech. Phys. Solids* 59, pp. 160–177. DOI: 10.1016/j.jmps.2010.11.005 (cit. on p. 26).

Xu, S. and X. Chen (2019). "Modeling dislocations and heat conduction in crystalline materials: atomistic/continuum coupling approaches". In: *Int. Mater. Rev.* 64.7, pp. 407–438. DOI: 10.1080/09506608.2018.1486358 (cit. on pp. 23, 25, 102).

Zhou, X. W., R. A. Johnson, and H. N. G. Wadley (2004). "Misfit-energy-increasing dislocations in vapor-deposited CoFe/NiFe multilayers". In: *Phys. Rev. B* 69, p. 144113. DOI: 10.1103/PhysRevB.69.144113 (cit. on p. 90).

Zhou, X. W., H. N. G. Wadley, R. A. Johnson, D. J. Larson, N. Tabat, A. Cerezo, A. K. Petford-Long, G. D. W. Smith, P. H. Clifton, R. L. Martens, and T. F. Kelly (2001). "Atomic scale structure of sputtered metal multilayers". In: *Acta Mater.* 49.19, pp. 4005–4015. DOI: 10.1016/S1359-6454(01)00287-7 (cit. on p. 44).

Zienkiewicz, O. C. and R. L. Taylor (2000). *The Finite Element Method*. Oxford: Butterworth Heinemann (cit. on pp. 7, 12, 14, 70).

Zimmerman, J. A., E. B. Webb III, J. J. Hoyt, R. E. Jones, P. A. Klein, and D. J. Bammann (2004). "Calculation of stress in atomistic simulation". In: *Model. Simul. Mater. Sci.* 12.4, S319–S332. DOI: 10.1088/0965-0393/12/4/s03 (cit. on p. 102).